Optical Switch on a Chip: The Talbot Effect, Lüneburg Lenses & Metamaterials

Hamdam Nikkhah

Thesis submitted to the Faculty of Graduate and Postdoctoral Studies in partial fulfillment of the requirements for the degree of

Master of Science

Systems Science Program
School of Electrical Engineering and Computer Science
University of Ottawa
Ottawa, Canada

Abstract

The goal of the research reported in this thesis is to establish the feasibility of a novel optical architecture for an optical route & select circuit switch suitable for implementation as a photonic integrated circuit. The proposed architecture combines Optical Phased Array (OPA) switch elements implemented as multimode interference coupler based Generalised Mach-Zehnder Interferometers (GMZI) with a planar Lüneburg lens-based optical transpose interconnection network implemented using graded metamaterial waveguide slabs. The proposed switch is transparent to signal format and, in principle, can have zero excess insertion loss and scale to large port counts. These switches will enable the low-energy consumption high capacity communications network infrastructure needed to provide environmentally-friendly broadband access to all.

The thesis first explains the importance of switch structures in optical communications networks and the difficulties of scaling to a large number of switch ports. The thesis then introduces the Talbot effect, i.e. the self-imaging of periodic field distributions in free space. It elaborates on a new approach to finding the phase relations between pairs of Talbot image planes at carefully selected positions. The free space Talbot effect is mapped to the waveguide Talbot effect which is fundamental to the operation of multimode interference couplers (MMI). Knowledge of the phase relation between the MMI ports is necessary to achieve correct operation of the GMZI OPA switch elements. An outline of the design procedures is given that can be applied to optimise the performance of MMI couplers and, as a consequence, the GMZI OPA switch elements. The Lüneburg Optical Transpose Interconnection System (LOTIS) is introduced as a potential solution to the problem of excessive insertion loss and cross-talk caused by the large number of crossovers in a switch fabric. Finally, the thesis explains how a Lüneburg lens may be implemented in a graded 'metamaterial', i.e. a composite material consisting of 'atoms' arranged on a regular lattice suspended in a host by nano-structuring of silicon waveguide slabs using a single etch-step. Furthermore, the propagation of light in graded almost-periodic structures is discussed. Detailed consideration is given to the calibration of the local homogenised effective index; in terms of the local parameters of the metamaterial microstructure in the plane and the corrections necessary to accommodate slab waveguide confinement in the normal to the plane. The concept and designs were verified by FDTD simulation. A 4 × 4 LOTIS structure showed correct routing of light with a low insertion loss of -0.25 dB and crosstalk of -24.12 dB. An -0.45 dB excess loss for 2D analysis and an -0.83 dB insertion excess loss for 3D analysis of two side by side metamaterial Lüneburg lenses with diameter of 15 μm was measured, which suggests that the metamaterial implementation produces minimal additional impairments to the switch.

Acknowledgments

I would like to express the deepest appreciation to my supervisor, Dr. Trevor Hall, for his continuous support and guidance; without which this thesis would not have been possible. His encouragement and enthusiasm have been a great motivation to continue this interesting work. Thanks are also due to Dr. Sawsan Abdul-Majid and Dr. Ramon Maldonado-Basilio, Photonic Technology Laboratory (PTLab) University of Ottawa, for their kind assistance with simulation and experimental facilities in the PTlab over the past two years. I also would like to express my gratitude to Dr. Winnie Ye at Carleton University and Dr. Jessica Zhang at CMC Microsystems for sharing their experience of silicon photonics design during the project. I would like to thank my friends and colleagues in PTLab for their contribution to a friendly working environment. Finally I give a special thank you to my family that provided the greatest and warmest encouragement to me throughout my life to pursuing my goals. I am indebted to them for their continuous support, closely or remotely, during my study.

Table of Contents

List of Tables

List of Figures

List of Abbreviations

AWGR	Arrayed Waveguide Grating Router
CGH	Computer Generated Hologram
CMOS	Complementary Metal-Oxide Semiconductor
CW	Continuous Wave
FDTD	Finite Difference Time Domain
E/O	Electrical to Optical Conversion
FDM	Finite Difference Mode
FELC	Ferroelectric Liquid Crystal
FOTIS	Fourier Optical Transpose Interconnection System
GHG	Green House Gas emissions
GMZI	Generalised Mach-Zehnder Interferometer
ICT	Information and Communications Technology
LOTIS	Lüneburg Optical Transpose Interconnection System
MEMS	Micro-Electro-Mechanical System
MMI	Multi-Mode Interference Coupler
MZI	Mach Zehnder Interferometer
NEMS	Nano-Electro-Mechanical System
OPA	Optical Phased Array
OPD	Optical Path- Length Difference
OTIS	Optical Transpose Interconnection System
O/E	Optical to Electrical Conversion

PIC	Planar Integrated Circuit
PLC	Planar Light Circuit
ROADM	Reconfigurable Optical Add Drop Module
SLM	Spatial Light Modulator
SOI	Silicon On Insulator
SWG	Sub-Wavelength Gratings
TDM	Time Division Multiplexed
TE	Transverse Electric
TM	Transverse Magnetic
UV	Ultra Violet
WDM	Wavelength Division Multiplexed
WSS	Wavelength Selective Switch
2D	2 Dimensional
3D	3 Dimensional

Chapter 1. Introduction

In science and engineering research one encounters phenomena, theories and techniques that inspire through their intrinsic beauty, elegance or ingenuity, yet have practical application. This thesis concerns one example: a silicon photonics integrated circuit concept that harnesses the beauty of the Talbot effect, the elegance of Lüneburg lenses, and the ingenuity of metamaterial design towards the practical goal of transparent optical switching. This will enable the low-energy consumption high capacity communications network infrastructure needed to provide environmentally-friendly broadband access to all. This chapter provides the motivation and background necessary to set the research in context, outlines the problem to be addressed and explains how the thesis has been structured to meet its objectives.

1.1 Background & Motivation

1.1.1 Optical Switch Networks

The sight of pedestrians in public places consulting small hand-held wireless devices that display moving images transmitted over the communications network infrastructure, something that was science fiction a couple of decades ago, is now accepted as commonplace. The first and last segments of a path through a network are often via wireless links but the intermediate links are universally wired by optical fibre. Yet today, the nodes of the network, where signals must be switched between different links, are largely electronic. At every switching node, optical signals must be converted to electronic signals (O/E conversion), switched and buffered electronically, and then converted from an electronic signal back to an optical signal (E/O conversion) before traversing the next segment. As a consequence, the switching process becomes dependent on the modulation format, the data protocol, and the bit-rate. Any upgrade to the network thereby requires upgrades to the O/E & E/O interfaces. An upgrade of the node electronics as a whole may be necessary to accommodate changes in protocol or improvements in capacity, such as provided by advanced coherent optical modulation formats that can boost channel capacities to 100 Gbit/s.

Yet, most of the traffic entering a node is bypass traffic destined to other nodes and has no need of O/E conversion. This observation has led to the introduction of reconfigurable optical add drop modules (ROADMs) and the wavelength selective switches (WSSs) from which they may be constructed. ROADM & WSS technology enables wavelength channels to be selected from an incoming wavelength division multiplex (WDM) to 'drop' incoming traffic, destined locally to the node, and to 'add' a wavelength channel onto the outgoing wavelength division multiplex; while the bulk of the traffic bypasses the node via the 'express channel'.

ROADM & WSS technology reduce the number of O/E – E/O conversions significantly but they operate at a bandwidth granularity of a wavelength channel, which today can be 100 Gbit/s. The reconfiguration speed is typically a few milliseconds to enable < 50 ms protection and restoration switching. Hence, if a component time division multiplexed (TDM) channel should be dropped locally; the whole wavelength must be dropped from the wavelength multiplex, the desired TDM channel extracted, and the remainder with additions reassembled and re-inserted into the wavelength multiplex. An optical switch that can change its state in a time interval small compared to the duration of a TDM time-slot can accomplish the same task with less complication.

Information & Communication Technology (ICT) energy consumption growth is out of control as capacity demands due to increased numbers of users with evermore bandwidth hungry applications outstrip improvements in energy efficiency. While this energy consumption cannot be met by renewable sources of energy, the associated greenhouse gas emissions (GHG) are raising faster than any other industry sector [1]. Optical circuit switching can help contain this growth. Data transfer over fibre is more energy efficient compared to over copper [2]; and circuit switching is more energy efficient compared to internet protocol (IP) routing [3]. The current wavelength-routed networks set up quasi-permanent circuits and consequently require optical switches capable of reconfiguring only on millisecond timescales. To emulate the bandwidth sharing provided by IP, the network requires virtual circuits with very fine bandwidth granularity which demands switching that is fast compared to the duration of the switchable entity.

To overcome the aforementioned technological and economic barriers to continued expansion of network capacity, optical switches are needed, therefore, that feature high-speed ($\sim < 1$ μs) reconfiguration with minimal energy consumption. To meet connectivity requirements, it must be possible to construct switch fabrics, i.e. switches with large port counts ($\sim > 64 \times 64$) composed of many small arrays of switch elements. The key is to use components that are suitable for integration with small footprints; thereby offering the economics of volume production. A variety of material integration platforms may be used to implement switch fabrics, such as indium phosphide (InP), silica on silicon (SiO_2-Si), silicon on insulator (SOI), and silicon (Si). The potential of tight light confinement resulting in extremely small device footprints and the compatibility with CMOS processing offering low-cost manufacturing has made Si a preferred choice for Photonic Integrated Circuits (PICs).

1.1.2 Broadcast & Select and Route & Select Switches

There are two fundamental switch element architectures: 'broadcast & select' and 'route & select'. In the broadcast & select architecture, the optical signal is sent to every possible destination via gates (shutters) that block the unwanted paths. This causes an unavoidable $1/N$ fan-out loss, where N is the port dimension. As a consequence of reciprocity, there is also an unavoidable $1/N$ fan-in loss if the input ports and output ports support a single transverse mode. Hence, there is an insertion loss of $1/N^2$ that limits the scaling of port dimension. The scaling limitation cannot be overcome by the use of optical amplifiers to provide gain that compensates for the loss, because the insertion loss reduces the signal-to-noise ratio by the same factor [4]. In the route & select architecture there is no fan-out or fan-in loss because the beam from an input port is steered to the desired output port; consequently the route & select architecture can scale to larger port dimension. For this reason, only route & select switch architectures will be considered further in this thesis.

Large route and select switch fabrics up to 1100×1100 have been demonstrated [5] using micro-electro-mechanical system (MEMS) switch elements which operate on slow (~ 1 ms) timescales in free-space architectures which are difficult to assemble and align and hence they are expensive to package. At the other end of the scale, low dimension ($\sim 2 \times 2$) Mach-Zehnder Interferometer (MZI) switch elements are capable of sub-nanosecond reconfiguration.

The basis of a MZI is a pair of waveguides arms, with an optical path-length difference (OPD) between them that are excited by a 3 dB coupler at the input and recombined by a 3 dB coupler at the output. Depending upon the OPD, the light that exits the two arms may interfere constructively or destructively, thus modulating the output power. $LiNBO_3$ based MZI modulators are commercially available and allow the OPD to be varied using the intrinsic electro-optic effect of this material [6]. Rapid progress is being made also with Si-based MZI modulators [7-16]. The OPD is then varied either thermo-optically using a heating element over one waveguide arm or electro-optically by the injection or depletion of charge carriers in the arms (the plasma dispersion effect).

The two arms limit a MZI to 2×2 dimension switch elements. However a large switch fabric may be built in principle using multiple stages of small switch elements, but suffer from rapid accumulation of insertion loss and crosstalk [17]. The large number of switch elements also leads to a modest energy requirement for a single switch element escalating to a total switch energy requirement beyond practical drive levels. As a consequence, there is a general trend for the reconfiguration times of the switch fabric to lengthen with increasing port count.

1.1.3 Optical Phased Arrays

In general route & select switches without moving parts operate according to the principles of phased array beam-forming [18]. The incoming light is distributed across an array of phase shift elements which adjust the distribution of optical path length and hence the spatial distribution of the phase. The light that exits the individual phase-shift elements is then superimposed by some coherent means (e.g. diffraction) resulting in an interference pattern. The structure of the interference pattern is determined by the state of the phase-shift elements. Effectively, light from an input port may be formed into a beam that may be steered between the output ports.

There are many embodiments of phased array beam-forming in optics most of which have other names for historical reasons. For example, Computer Generated Holograms (CGHs), are an instance of an OPA in two dimensions (2D) – each pixel of the hologram acts as an antenna element, the phase of which is determined by the optical path length difference induced by the pixel either through the refractive index distribution or the surface relief of the hologram. A CGH design algorithm is therefore an example of an optical beam-forming procedure. A beam steering switch using a ferroelectric liquid crystal (FELC) on silicon VLSI spatial light modulator (SLM) as a programmable hologram has been demonstrated

[19]. FELC SLMs are capable of <10 μs reconfiguration and the architecture may be feasibly scaled to 64×64 ports. However, the free-space architecture does bring daunting assembly and packaging issues.

The relative phase induced by a particular optical path difference is linearly proportional to the frequency (equivalently vacuum wavelength) of the light. This enables the vacuum wavelength to be used as the OPA control variable, for example, by combining an Arrayed Waveguide Grating Router (AWGR) with fast tuneable wavelength conversion technology [20]. The output port of the AWGR, from which light from a particular input port emerges, is determined by the wavelength. Contemporary data modulation formats employ phase and amplitude modulation with coherent detection [21]. As a consequence, the switch is not truly 'transparent' if the wavelength convertors destroy phase information. Wavelength conversion preserving phase information is possible using parametric methods (e.g. nonlinear optical four-wave mixing) but conversion efficiencies are poor [22].

2D OPAs with 4×4 and 16×16 elements that emit light out of the plane of a silicon PIC were reported in [23] for optical wireless applications and subsequently, have been demonstrated with up to 4096 elements [24]. Beam steering may be achieved only by wavelength tuning or thermo-optic phase tuning [25]. Rapid addressing of very large number of elements remains a challenge and, in the context of a switch, the free-space architecture brings assembly and packaging issues (c.f. the ROSES FELC-SLM beam steering switch [19]. Reference [26] describes how these problems might be ameliorated by adaptive beam-forming).

1.1.4 Generalised Mach-Zehnder Interferometers

A multimode interference coupler (MMI) may be substituted as an alternative to a 'free-space' region. An MMI is a passive planar waveguide component that directs an equal fraction of the power entering each port to each of its output ports with relative phase differences that are intrinsic to the MMI and very well controlled. The Talbot effect, the self-imaging of periodic fields first discovered in free-space [27], is fundamental to its operation. The Generalised Mach-Zehnder Interferometer (GMZI) structure is a compact sandwich of a $1 \times M$ MMI coupler, an array of M electro-optic-phase shift elements, and a $M \times N$ MMI coupler ($M \geq N$). A first MMI splits the optical input equally between several independent waveguide electro-optical phase shift elements which are controlled by voltage or current. The optical beams are recombined by a second MMI coupler at the output. The electro-optic phase shift element controls the interference at each output port, directing the input light to the desired output. Although, this structure has been introduced here as a variant of an OPA, it is normally described as a generalisation of a MZI ($M = N = 2$). There have been a number of reports of the $1 \times N$ MZI switch structure implemented in various integration platforms [28-31].

1.1.5 Optical Interconnection Networks

Whatever the implementation technology, all switch elements will have a practical limitation to their port dimensions. In particular, the basic unit element of an OPA is a $1 \times N$ route or (by reciprocity) a $N \times 1$ select switch (c.f. the GMZI switch element described in Section 1.1.4). There is therefore a universal requirement for an optical interconnection network that can combine switch elements into a switch fabric with larger port dimension. For example, a $N \times N$ route & select transparent optical switch may be constructed using a two stage switch fabric; the first stage containing N route switch elements of dimension $1 \times N$ and the second stage containing N select switch elements of dimension $N \times 1$ interconnected by a $N \times N$ to $N \times N$ transpose interconnect.

The $N \times M$ to $M \times N$ transpose interconnection is fundamental to any multistage interconnection network and there have been numerous demonstrations of its implementation as a three-dimensional (3D) free-space optical system employing bulk optical components. An optical system using Fourier transform lenses to implement a transpose interconnection is described in [32] and various architectures for optical crossbar switches that exploit this system are described in [33]. However, 3D free-space optical systems are bulky and unstable due to the stringent alignment tolerances that must be met.

Alignment and stability issues can be largely overcome through the lithographic precision offered by planar light circuits. The restriction on scaling consequent upon the loss of one dimension, can be somewhat compensated by the nano-scale component footprints attainable in a silicon photonics integration platform. However, whereas in free-space, cross-over interconnection offers intrinsically no insertion loss and no cross-talk, it is a challenge to contain within reasonable bounds the accumulative insertion loss and cross-talk of the very large number of waveguide crossover interconnections inherent to a planar implementation.

Crossovers of photonics wires on silicon on insulator (SOI) have been reported with insertion loss of between -0.4 dB and -0.1 dB per crossing [34, 35] and cross-talk below -40 dB [36] which is achieved by expanding the mode using elliptical tapers and a lower index contrast in the cross-over region which requires a two-depth etch step that complicates the fabrication process.

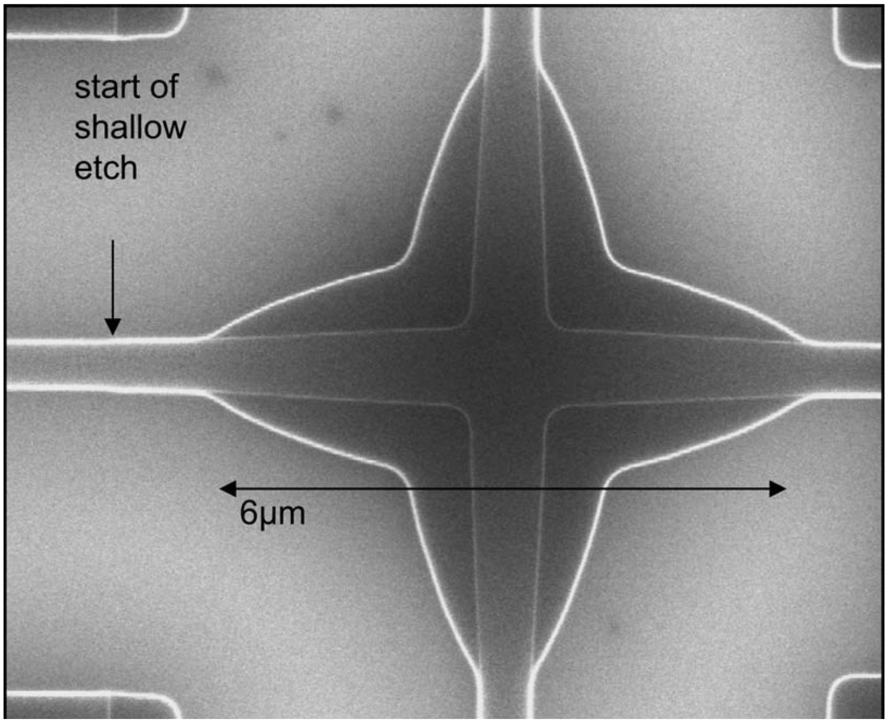

Fig. 1.1. A micrograph showing the structure of a waveguide crossover with elliptical tapers with reduced index contrast fabricated in SOI for operation at a wavelength of 1.55 μm. (Copyright Optical Society of America 2013, reproduced with permission from reference [36]).

Advances in lithography have enabled the fabrication of nanostructures with sub-wavelength feature sizes and separations. The effective refractive index seen by the mean optical field propagating in such structures is determined by the variation in local density of the sub-wavelength structures. In essence, one can fabricate thin film composite materials with engineered optical properties. Popularly known as metamaterials and known in the past as artificial dielectrics, these materials may also be viewed as photonic crystals operating in the long wavelength regime in the special case that the microstructure is periodic.

Bock et al [37] report the design, simulation, and experimental demonstration of a novel waveguide crossing based on sub-wavelength gratings (SWG) in silicon waveguides. The structure is shown in Figure 1.2. A transition region is used to match the incoming mode from the solid waveguides and the fundamental Bloch mode of the longitudinally periodic sub-wavelength grating waveguides that consist of small cubes of silicon separated by air gaps. The widths of the cubes are tapered down towards the crossover region expanding the modes locally in the crossover region. Fabrication requires only a single etch step. Fabricated devices offered insertion loss as low as -0.023 dB/crossing, polarisation dependent loss of < 0.02 dB and crosstalk of <-40 dB.

An alternative approach that avoids waveguide crossovers is to use planar lenses embedded in slab waveguides to implement ‘free-space optics on-a-chip’. This thesis explores the potential of a metamaterial implementation of the on-chip planar lenses required.

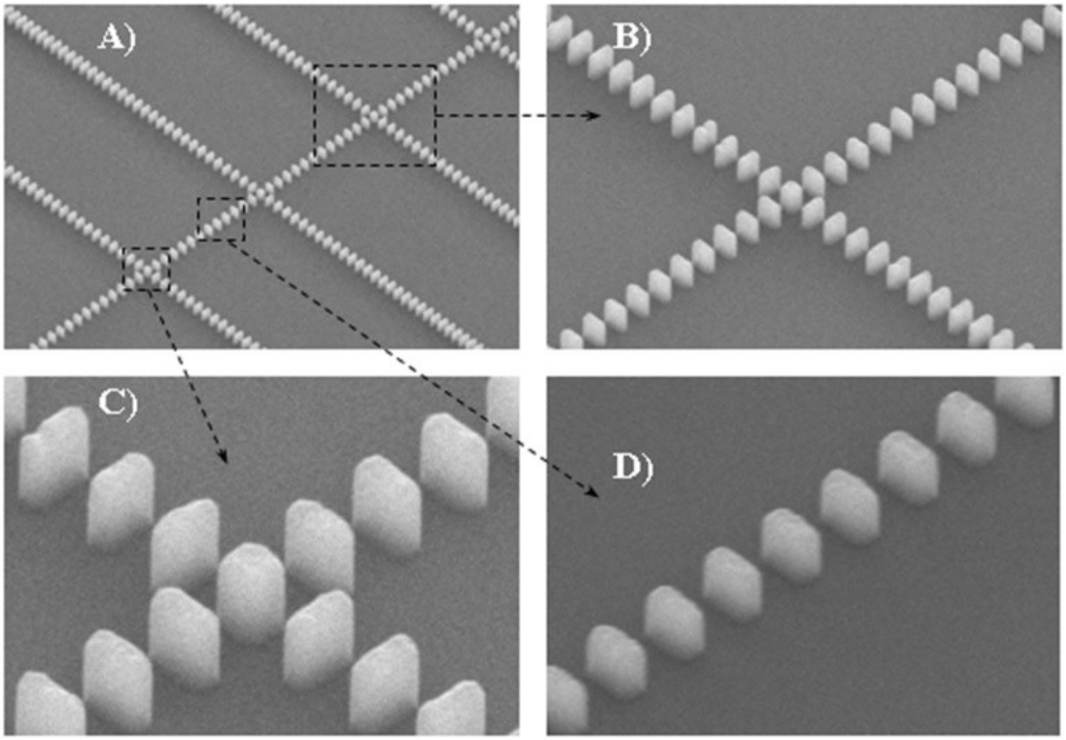

Fig. 1.2. Scanning electron microscope images of SWG crossings: *a*) multiple SWG crossings, *b*) one SWG crossing, *c*) detail of the crossing region with square center segment (220 nm × 220 nm) and *d*) SWG straight waveguide (Copyright Dr. P. J. Bock, 2013, reproduced with permission from reference [38]).

1.2 Aim & Objectives

The overall aim of this thesis is to establish the feasibility of a novel optical architecture for an optical route & select circuit switch suitable for implementation as a photonic integrated circuit. The proposed architecture combines optical phased array switch elements implemented as multimode interference coupler based generalised Mach-Zhender interferometers with a planar Lüneburg lens-based optical transpose interconnection system implemented using graded metamaterial waveguide slabs. The proposed switch is transparent to signal format and, in principle, can have zero excess insertion loss and scale to large port counts. The switch architecture may be implemented using a variety of material integration platforms, such as indium phosphide (InP), silica on silicon (SiO_2-Si), and silicon (Si) on insulator (SOI), but the focus of this work is SOI because its tight light-confinement offers the potential for extremely small device footprints and its compatibility with CMOS processing offers potential for low cost manufacture. The active phase shift elements required by the OPA may be implemented as electro-optic modulators which can operate at high speed (<100 ps) even in silicon. However, the design of the active phase shift elements falls outside the scope of this thesis.

The specific objectives are:

1) to clarify, generally, self-imaging in multimode interference couplers (MMI) in terms of its relation to the Talbot effect in free-space and, specifically, to determine the intrinsic phase relationships between the ports of a MMI;
2) to elucidate beam steering by an optical phased array implemented as generalised Mach-Zehnder interferometers with consideration of MMI design principles and port phase relations;
3) to formulate the design of a planar Lüneburg lens-based optical transpose interconnection system (OTIS);
4) to verify correct operation and to make a preliminary assessment of the performance of OTIS designs up to dimension $(4 \times 4) \times (4 \times 4)$ by full-wave simulation;

5) to formulate design procedures for graded metamaterial Lüneburg lenses valid in the near sub-wavelength region that account for photonic band structure and waveguide confinement effects; and,
6) to verify correct operation and to make a preliminary assessment of the performance of a Lüneburg lens implemented as a graded metamaterial compared to an ideal Lüneburg lens.

1.3 Structure of the Thesis

To achieve these objectives the thesis has been structured into five chapters:

Chapter 1 describes the motivation and the background of the research. It addresses the importance of switch structures in optical communications networks, the difficulties of scaling to a large number of switch ports and introduces the most relevant solutions offered in the literature today.

Chapter 2 introduces the Talbot effect, i.e. the self-imaging of periodic field distributions in free space. It elaborates a new approach to finding the phase relations between pairs of Talbot image planes at carefully selected positions. The free space Talbot effect is mapped to the waveguide Talbot effect which is fundamental to the operation of multimode interference couplers (MMI). The phase relation between the ports of an MMI coupler with a different number of ports is elaborated. Knowledge of the phase relation between the MMI ports is necessary to achieve correct operation of the GMZI OPA switch elements described in Chapter 3.

In Chapter 3, the results of Chapter 2 are used to explain the behaviour and characteristics of MMI couplers and their role in the GMZI OPA switch elements. The chapter also outlines the design procedures that can be applied to optimise the performance of MMI couplers and, as a consequence, the GMZI OPA switch elements. The chapter then introduces the optical transpose interconnection system (OTIS) using three stages of thin lenses as a potential solution to the problem of excessive insertion loss and cross-talk caused by the large number of crossovers in a switch fabric. The Lüneburg lens, a gradient index lens capable of perfect imaging, is then introduced and ray transformation properties are explained as an optical analogue of motion in a central potential. Exploiting these properties, the thin lenses are replaced by Lüneburg lenses and the OTIS structure is adapted in accordance.

In Chapter 4 it is explained how a Lüneburg lens may be implemented in a graded 'metamaterial', i.e. a composite material consisting of 'atoms' arranged on a regular lattice suspended in a host by nano-structuring of silicon waveguide slabs using a single etch-step. Furthermore, the propagation of light in graded almost-periodic structures is discussed. Detailed consideration is given to the calibration of the local macroscopic effective index; in terms of the local parameters of the metamaterial microstructure in the plane and the corrections necessary to accommodate slab waveguide confinement in the normal to the plane.

Chapter 5 summarises the most important points arising in the thesis, draws some conclusions and makes recommendations for further work.

The considerations are illustrated throughout the thesis by incorporating the results of simulations, which together demonstrate the practical potential of the overall switch fabric concept.

The Photon Design suite provided the principal tools that were used, including:

1. FimmWave & FimmProp (Eigenmode Expansion Method [39]) , for the simulation of planar waveguide elements;
2. OmniSim (Finite Difference Time Domain [40]) for the simulation of the Lüneburg lens based OTIS; and,
3. CrystalWave (Photonic Band Structure Solver extension of OmniSim) for the simulation of the metamaterial structures.

These tools were supplemented by custom MatLab scripts. A Python script was written to automate the quantisation of continuous refractive index profiles to metamaterial atom size. A listing is provided in Appendix V

1.4 Original Contributions and Achievements

The thesis contributes to the advancement of the field of photonic integrated circuits through both original contributions and the critical analysis of current knowledge. The contributions of the author include:

1. A critical analysis of knowledge drawn together from formally disparate subjects including: optical switching; phased arrays & beam-forming; the Talbot effect; planar waveguides; multimode interference couplers; generalised Mach-Zehnder interferometers; free-space optical transpose interconnection systems; the classical optics of Lüneburg lenses; photonic crystals, homogenisation & metamaterials.
2. A unique innovative switch architecture for an optical route & select circuit switch suitable for implementation as a photonic integrated circuit. The architecture combines optical phased array switch elements implemented as multimode interference coupler based generalised Mach-Zehnder interferometers with a planar Lüneburg lens-based optical transpose interconnection network implemented using graded metamaterial waveguide slabs. The proposed switch is transparent to signal format and, in principle, can have zero excess insertion loss and scale to large port counts.
3. The clarification of the theory of the Talbot effect in the context of both free-space and waveguide geometries introducing a new approach to determine the phase relations between the ports of MMI couplers. The introduction of the new concept of Talbot transfer matrices and the derivation of their relation to MMI transfer matrices.
4. The introduction of an original optical transpose interconnection system (OTIS) architecture using Lüneburg lenses with associated design procedures and verification by Finite Difference Time Domain (FDTD) simulation.
5. The introduction of an original quantisation procedure for graded metamaterial design based upon calibration using photonic band structure data.

The results presented in this thesis were obtained during a period of study at the University of Ottawa for a M.Sc. degree from Fall 2011 to Summer 2013 under the supervision of Dr. Trevor Hall. This work is to the best knowledge of the author original. The following publications related to this thesis research were published during this period.

1. **H. Nikkhah**, A. Benhsaien, R. Maldonado-Basilio, S. Abdul-Majid, T. J. Hall*,‘ Metamaterial Lüneburg waveguide lenses for switch fabric on-a-chip applications’*, Photonics North, Ottawa, June 2013. Proc. of SPIE (*to appear*).

2. **H. Nikkhah**, T. J. Hall, '*A transpose optical interconnect utilising metamaterial Lüneburg waveguide lenses for switch fabric on-a-chip applications*', SPIE Photonics West, San Francisco, United States, 2-7 February 2013, Proc. of SPIE **8627** , 86270V-1.
3. R. Maldonado-Basilio, R. Li, S. Abdul-Majid, **H. Nikkhah**, K. W. Leong, T. J. Hall, *'Effect of the degree of phase-correlation of laser sources on the transmission and optical coherent detection in radio-over-fibre systems'*, SPIE Photonics West, San Francisco, United States, 2-7 February 2013, Proc. of SPIE **8645**, 86450E.
4. **H. Nikkhah**, K. Van Acoleyen, R. Baets, '*Beam steering for wireless optical links based on an optical phased array in silicon*', Annals of Telecommunications, Springer, **68**(1-2) , February 2013, pp 57-62, (online since June 2012).
5. T. Hall, R. Maldonado-Basilio, S. Abdul-Majid, J. Seregelyi, R. Li, I. Antolín Pérez, **H. Nikkhah**, F. Lucarz, J. L. de Bougrenet de La Tocnaye, B. Fracasso, P. Pajusco, C. Kärnfelt, D. Bourreau, M. Ney, R. Guemri, Y. Josse, H. Liu, '*Radio-over-Fibre Access for Sustainable Digital Cities*', Annals of Telecommunications, Springer, 2013, **68**(1-2), pp. 3-21.
6. **H. Nikkhah**, Q. Zheng, I. Hassan, S. Abdul-Majid, T. J. Hall, '*The Free Space and Waveguide Talbot Effect: Phase Relations and Planar Light Circuit Applications*', Photonics North 2012, Montreal, Canada, June 2012, Proc. SPIE **8412**, 2012, art. 841217.
7. **H. Nikkhah**, R. Baets, K. Van Acoleyen: '*Optical Phased Arrays in Silicon on Insulator for Optical Wireless Systems*', Green Radio over Fibre and all-optical Wireless Technologies for Wireless Access Networks (GROWAN 2011), Brest, France, 15-17 June 2011.

Chapter 2. The Free-Space & Waveguide Talbot Effect

2.1 Introduction

In this chapter, it is explained how optical fields that are periodic in the transverse plane self-image periodically as they propagate along the optical axis: a phenomenon known as the Talbot effect. A transfer matrix is defined that relates the amplitude and phase of point sources placed on a particular grid at the input to their respective multiple images at a fractional Talbot effect image plane. The free-space Talbot effect may be mapped to the waveguide Talbot effect. Applying this mapping to the transfer matrix enables the prediction of the phase and amplitude relations between the ports of a Multimode Interference (MMI) coupler; a planar waveguide device. The transfer matrix approach has not previously been applied to the free-space case and its mapping to the waveguide case provides greater clarity and physical insight into the phase relationships than previous treatments.

In Section 2.2, the underlying physics of the Talbot effect in free space is first introduced with emphasis on the positions along the optical axis at which images occur; their multiplicity; and their relative phase relations determined by the Gauss Quadratic Sum of number theory. An original Talbot transfer matrix formulism is introduced in Section 2.3 to predict the phase relationships between carefully selected points on transverse planes separated by a fractional Talbot image distances within the Talbot carpet. In Section 2.4 the physics of self-imaging in multimode waveguides is explained and the Talbot transfer matrices are mapped into the corresponding waveguide Talbot transfer matrices. These matrices predict the port phase relations intrinsic to an MMI. These phase relationships are critical to coherent optical Planar Light Circuit (PLC) applications such as 90° optical hybrids for coherent optical receiver front-ends, external optical I-Q modulators for coherent optical transmitters; and optical phased array switches. The chapter closes with a summary in Section 2.5 of the most significant results. The formulism developed in this chapter is applied in the Chapter 3 to analyse the operation of generalised Mach-Zehnder interferometer switch elements.

2.2 The Talbot Effect in Free Space

Periodicity and coherency are two properties that regularly feature in problems in optical science and engineering. Their consequences for applications in switching, interconnections in planar optics and phase tuning are profound. Wave fields that are periodic in a transverse plane induce periodicity in the longitudinal direction manifested by self-images of the initial field [41]. This phenomenon is known as the Talbot effect in recognition of William Henry Fox Talbot (1800-1877) who first observed the effect in 1836 [27]. Talbot was a British mathematician and early pioneer of photography. His achievements include co-invention of the polarising microscope utilized in mineralogy; and, as a mathematician, proving several theorems regarding elliptic integrals [42]. While he was examining diffraction gratings under white light illumination with a magnifying lens, he found that the image of the grating was repeated even when he moved the lens out of focus [27]. Talbot demonstrated the results of his experiment at a meeting of the British Association in Bristol:

> *"It was very curious to observe that though the grating was greatly out of the focus of the lens ... the appearance of the bands was perfectly distinct and well defined. The experiments are communicated in the hope that they may prove interesting to the cultivators of optical science."* [42]

The principle of the Talbot effect rests upon diffraction which is defined as a deviation of light from a straight path that is the consequence of the wave nature of light. When a structure that is periodic in the transverse plane (x-coordinate) is illuminated by a coherent light field with a wavelength far smaller than the period it causes the reproduction of the structure in a sequence of images in transverse planes located at specific positions along the optical axis (z-coordinate) [44]. This effect is a natural consequence of the diffraction of light in the near-field (Fresnel diffraction) and was explained theoretically by John William Strutt, 3rd Baron Rayleigh (1842-1919); 50 years after the effect was discovered by Talbot, Lord Rayleigh calculated the Talbot distance and published his results in 1881 in a paper entitled: "*On copying diffraction-gratings, and on some phenomena connected therewith.*" [45]

Figure 2.1 illustrates the diffraction of light normally incident on a structure consisting of parallel regularly spaced slits. Each slit diffracts the incident light causing it to spread similar to a cylindrical wave at sufficient distances from the slit. The diffracted light from each slit ultimately overlap and interfere with each other.

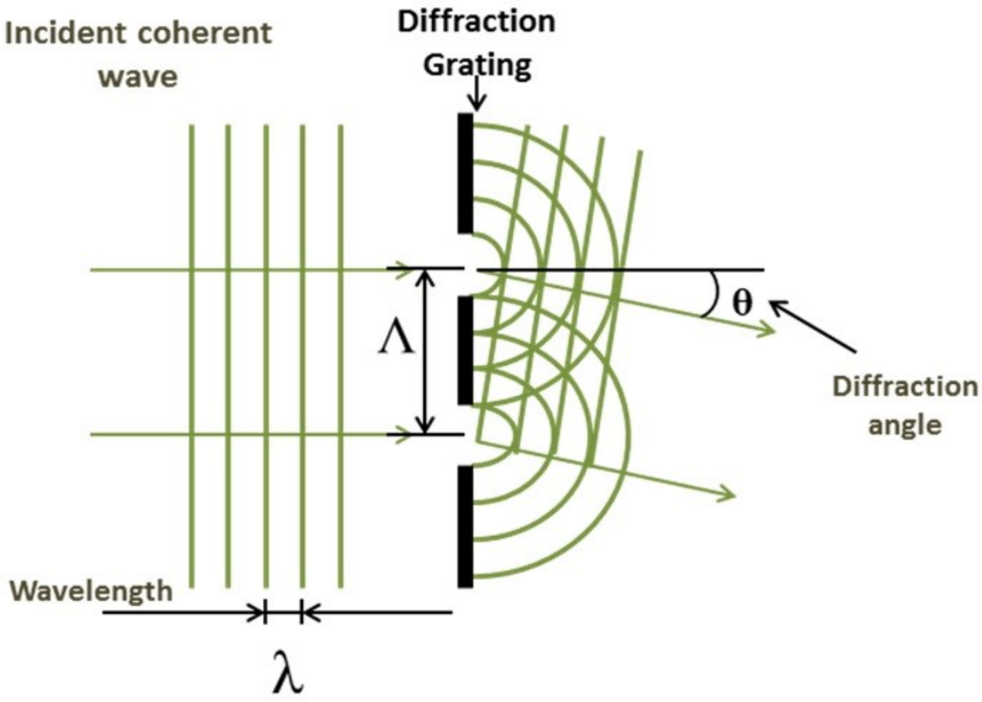

Fig. 2.1. The diffraction of a coherent wave by a diffraction grating.

Referring to Figure 2.1, it can be seen that when:

$$\Lambda sin\theta = n\lambda$$

Equation 2.1

where Λ is the period of the grating; λ is the vacuum wavelength; and n is an integer; constructive interference takes place on planes with a normal inclined by an angle θ to the optical axis. Equation 2.1 is Bragg's equation which provides a condition for the diffracted cylindrical waves to constructively interfere to form a diffracted plane wave. These plane waves are index by their integer order n.

The diffracted light therefore consists of plane wave components propagating at an angle θ_n with respect to the optical axis (see Figure 2.2). This angle depends on the wavelength of the light source, the spacing of the slits, and the diffraction order, as shown in Figure 2.3. The width of the slits affects the amplitude of the components via an overall envelope function. The diffracted plane wave components interfere constructively or destructively depending on their relative phases on propagation away from the structure.

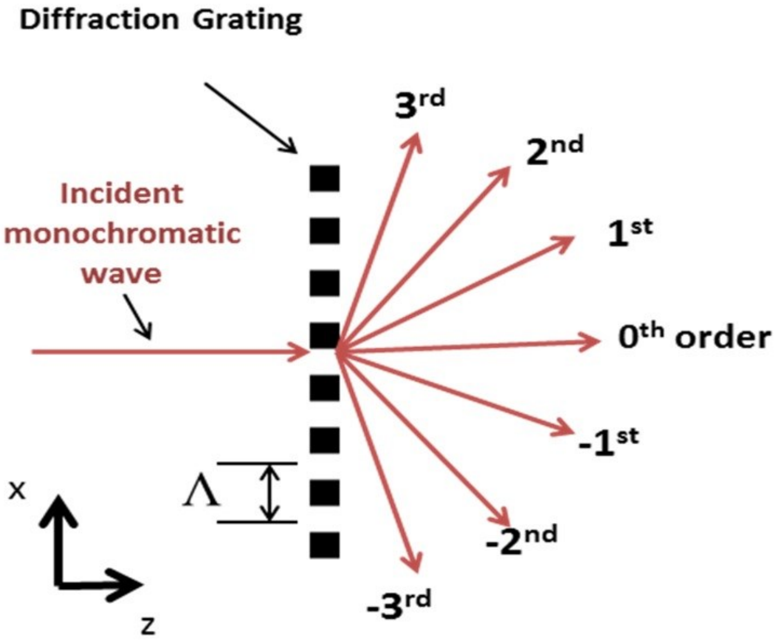

Fig. 2.2. A normally incident plane wave passing through a structure that is periodic in the transverse plane (*x*-axis), is diffracted into several plane-wave orders with different propagation angles to the optical axis (*z*-axis) that are defined by the Bragg equation (see Figure 2.3)

The wave-vector diagram, shown in Figure 2.3, more clearly illustrates the relation between the angles of propagation θ_n of the incident and diffracted beams.

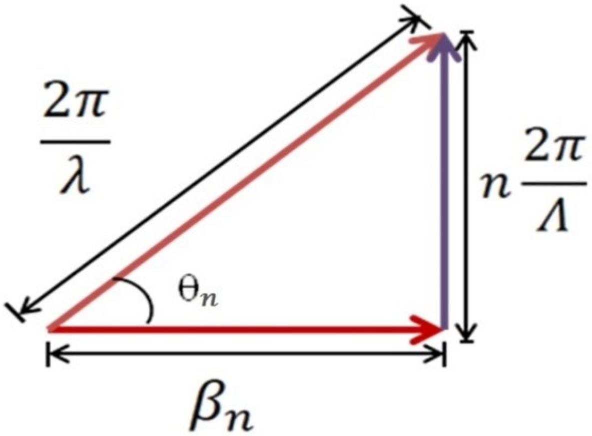

Fig. 2.3. the wave-vector diagram shows the geometrical relation between the diffracted beam with a diffraction angle of θ_n relative to the incident wave-vector, longitudinal component of propagation constant β_n and the transverse grating wave-vector $(2\pi/\Lambda)$

By reference to Figure 2.3 and with the application of Pythagoras's theorem, the phase matching condition is found:

$$\beta_n^2 + (n\kappa)^2 = k^2$$

Equation 2.2

where β_n is the longitudinal component of the propagation constant of the n^{th} order plane wave component; $n = \cdots - 2, -1, 0, 1, 2$ ... is an integer specifying the order of the beam; $\kappa = 2\pi/\Lambda$ is the spatial frequency of the grating (Λ is the transverse period or 'pitch' of the grating structure); and $k = 2\pi/\lambda$ is the wave-number of the incident beam (λ is the wavelength).

Note:

$$\begin{aligned} \beta_n &= \pm\sqrt{k^2 - (n\kappa)^2} \quad && (n\kappa)^2 \le k^2 \\ \beta_n &= \pm i\sqrt{(n\kappa)^2 - k^2} \quad && (n\kappa)^2 > k^2 \end{aligned}$$

Equation 2.3

The choice of sign depends on the choice of phase factor to represent forward and backward propagating plane waves.

The diffraction angles θ_n can be obtained from the Bragg equation (Equation 2.1) which follows from the application of elementary trigonometry to the wave-vector diagram:

$$\begin{gathered} k cos(\theta_n) = \beta_n \\ k sin(\theta_n) = n\kappa \\ \Longrightarrow \\ sin(\theta_n) = \frac{n\lambda}{\Lambda} \end{gathered}$$

Equation 2.4

Figure 2.4 shows the general form of the Talbot effect. A periodic structure located at $z = 0$ is reconstructed at intervals of $2z_T$. These reconstructions are called self-images or primary Talbot images. Mid-way between these primary Talbot images, there are self-images which are shifted by half a grating period in the transverse plane relative to the primary Talbot images. These are known as secondary Talbot images. In other words, a Talbot image occurs at integer multiples of the Talbot distance z_T . For even integer multiples, the result is a primary image and, for odd integer multiples, the result is a secondary Talbot image.

Lord Rayleigh calculated the Talbot distance [45] as:

$$z_T = \frac{\Lambda^2}{\lambda}$$

Equation 2.5

The Talbot distance is proportional to the square of the grating period and inversely proportional to the wavelength of the light. For example, for a yellow light source with a wavelength of 585 nm illuminating a grating structure with a period of 400 µm, the Talbot distance is 273.5 mm; which increases to 340.4 mm for a blue light source with a wavelength of 470 nm. For a grating with a period of 100 µm, the Talbot distances reduce to 17.1 mm and 21.3 mm for the yellow light and blue light sources respectively.

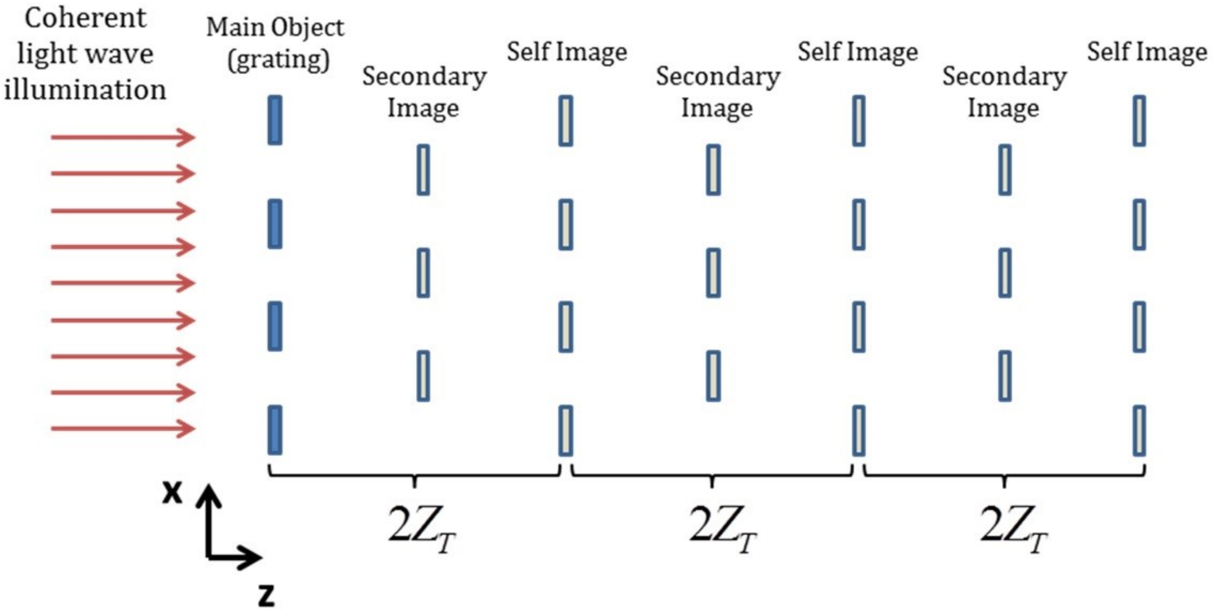

Fig. 2.4. The Talbot effect with primary and secondary Talbot self-images. The self-images are repeated at intervals of $2z_T$

The intensity of the field may be plotted over both transverse (x) and longitudinal (z) co-ordinates. Since the field is periodic in both co-ordinates, it is sufficient to plot one period in each direction only (i.e. the plot is over an elementary unit cell). The result is called a Talbot carpet because of its resemblance to a Persian carpet [46] (see Figure 2.5).

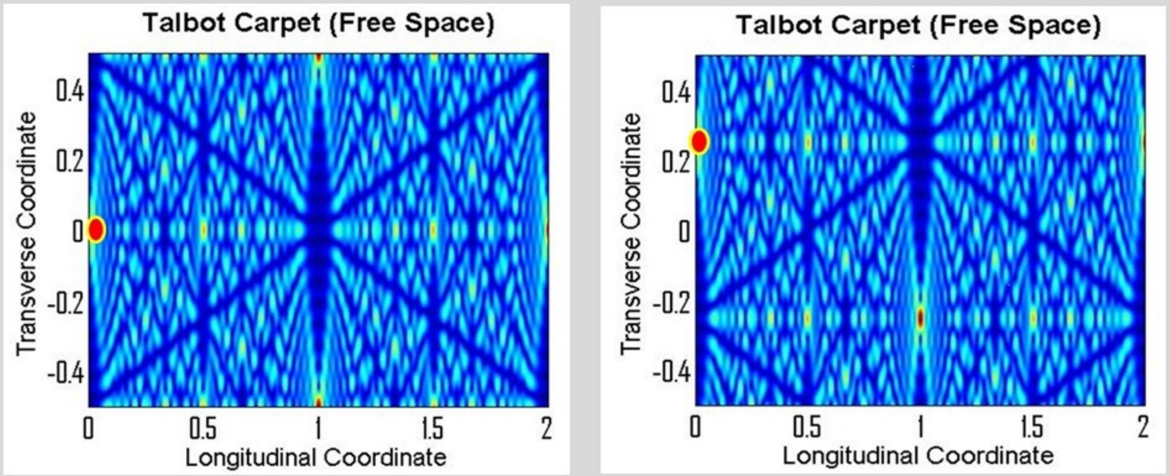

(a) The field excited by a point source at the input $z = 0$ *on the central axis* $x = 0$. *Note the primary image at* $z = 2$ *and the secondary image at* $z = 1$. *The secondary self-image of the source at unit Talbot distance is divided between the two boundaries because of the periodicity.*

(b) *The field excited by a point source at the input* $z = 0$ *at an offset from the central axis of* $x = 0.25$. *Comparison of (a) & (b) demonstrates the (circular) transverse translation invariance.*

Fig. 2.5. The free-space Talbot carpet. The images show one elementary unit cell. The boundaries of the cell should be identified as a consequence of periodicity. The transverse co-ordinate is in units of the period Λ and the longitudinal co-ordinate is in units of the Talbot distance $z_T = \Lambda^2/\lambda_0$ where λ_0 is the vacuum wavelength. Red indicates high intensity and dark blue low intensity. Self-images occur at integer multiples of the Talbot distance. A primary self-image of the source appears at twice the Talbot distance. Intricate multiple overlapping (interfering) images appear at rational fractional multiples of the Talbot distance.

The remainder of this section follows Berry's formulation of the Talbot effect [47].

Consider the initial field $\tilde{f}$ immediately after transmission through the grating structure. Since it is periodic in the x-coordinate with period Λ, it may be written as:

$$\tilde{f}(x) = \sum_{n=-\infty}^{\infty} f(x - n\Lambda)$$

Equation 2.6

where f is the field over a single lateral period $[-\Lambda/2\,,\ \Lambda/2\,]$ outside of which the field is zero.

This expression may be written as a convolution:

$$\tilde{f} = h \otimes f$$

Equation 2.7

that is:

$$\tilde{f}(x) = \int_{-\infty}^{\infty} h(x-y) f(y)\, dy$$

Equation 2.8

where:

$$h(x) = \sum_{n=-\infty}^{\infty} \delta(x - n\Lambda)$$

Equation 2.9

Since h is periodic with period Λ , it admits a Fourier series representation:

$$h(x) = \sum_{n=-\infty}^{\infty} c_n exp(in\kappa x)$$

$$\kappa = \frac{2\pi}{\Lambda}$$

Equation 2.10

The coefficients are found from:

$$c_n = \frac{1}{\Lambda} \int_{-\Lambda/2}^{\Lambda/2} h(x) exp(-in\kappa x)\, dx$$

Equation 2.11

On substituting Equation 2.9 into Equation 2.11, only the Dirac distribution at the origin contributes and hence $c_n = 1/\Lambda$ and consequently h may be represented by the Poisson sum:

$$h(x) = \frac{1}{\Lambda} \sum_{n=-\infty}^{\infty} exp(in\kappa x)$$

Equation 2.12

The convolution kernel h may be extended as a solution to the Helmholtz equation by augmenting each term with a factor that describes its phase evolution with propagation along the z-axis:

$$h(x,z) = \frac{1}{\Lambda} \sum_{n=-\infty}^{\infty} exp(in\kappa x) exp(i\beta_n z)$$

Equation 2.13

Equation 2.13 is a sum of plane waves that reduces to Equation 2.12 when $z = 0$. Each plane wave component is a solution of the Helmholtz equation provided:

$$\beta_n^2 + (n\kappa\ )^2 = k^2$$

Equation 2.14

This is identical to Equation 2.2 and hence Equation 2.3 provides expressions for β_n up to a choice of sign. Limiting consideration to forward propagating waves with an implicit $exp(-i\omega t)$ time dependence; the appropriate choice is:

$$\begin{aligned} \beta_n &= \sqrt{k^2 - (n\kappa)^2} \quad (n\kappa)^2 \leq k^2 \\ \beta_n &= i\sqrt{(n\kappa)^2 - k^2} \quad (n\kappa)^2 > k^2 \end{aligned}$$

Equation 2.15

To summarise, the problem has been cast as a linear system which generates the output $\tilde{f}$ at any distance by convolving a single period of the input f by a system impulse response h. By construction, h satisfies the Helmholtz equation and hence by linearity so does $\tilde{f}$. Moreover, h reduces to a comb function replicating f at $z = 0$ to model the transverse periodicity of the initial field.

Now, consider the system response in the paraxial approximation. This corresponds to fields that have plane wave components propagating at angles θ to the optical axis sufficiently small that $sin(\theta) \approx \theta$. Equivalently, $(n\kappa)^2 \ll k^2$ and hence

$$\beta_n = \sqrt{k^2 - (nK)^2} = k\left[1 - \left(\frac{n\kappa}{k}\right)^2\right]^{\frac{1}{2}} \approx k\left[1 - \frac{1}{2}\left(\frac{n\kappa}{k}\right)^2\right] = k - \frac{1}{2}n^2\frac{\kappa^2}{k}$$

Equation 2.16

or

$$\begin{aligned} \beta_n z &\approx kz - 2\pi n^2 \frac{z}{2z_T} \\ z_T &= \frac{\Lambda^2}{\lambda} \end{aligned}$$

Equation 2.17

By substitution of Equation 2.17 in Equation 2.13, $h(x,z)$ may be re-written:

$$h(x,z) = e^{ikz}\frac{1}{\Lambda}\sum_{n=-\infty}^{\infty} e^{i2\pi n\frac{x}{\Lambda}} e^{-i\pi n^2\frac{z}{z_T}}$$

Equation 2.18

For a primary image to form, the phase factors associated to each of the components in the summation of Equation 2.18 must agree with their initial value. This is exactly the case at transverse planes intersecting the axis at even integer multiples of the Talbot distance:

$$\frac{z}{z_T} = 2m \qquad\qquad m \in \mathbb{Z}$$

$$\Rightarrow$$

$$e^{-i\pi n^2\frac{z}{z_T}} = e^{-i2\pi m n^2} = 1 \quad \forall n \in \mathbb{Z}$$

$$\Rightarrow$$

$$h = e^{ikz}\sum_{n=-\infty}^{\infty} \delta(x - n\Lambda)$$

Equation 2.19

A closer analysis elaborated in Appendix I reveals multiple imaging occurs at rational fractional multiples of the Talbot distance:

$$z = \frac{p}{q} z_T \quad p, q \in \mathbb{Z}$$

Equation 2.20

The underlying mathematical reason this occurs is consequent on the serendipitous accident that:

$$(-1)^{l^2} = (-1)^l \quad l \in \mathbb{Z}$$

Equation 2.21

which can be applied under certain circumstances to replace a quadratic dependence by a linear dependence on an index in the exponent of exponential terms deriving from Equation 2.18.

Application is made also of the fact that it is always possible to rearrange the elements of a sequence into a set of sub-sequences, each of length, q, and then find the sum of the sequence by summing the subsequence sums:

$$\sum_{n=-\infty}^{\infty} a_n = \sum_{s=0}^{q-1}\sum_{l=-\infty}^{\infty} a_{lq+s}$$

Equation 2.22

The result found in Appendix I is:

$$h(x,z) = e^{ikz} \sum_{m=-\infty}^{\infty} \frac{1}{q^{1/2}} g(2m)\delta\left(x - (2m)\frac{\Lambda}{2q}\right) \qquad even\, p\; or\; q$$

$$h(x,z) = e^{ikz} \sum_{m=-\infty}^{\infty} \frac{1}{q^{1/2}} g(2m+1)\delta\left(x - (2m+1)\frac{\Lambda}{2q}\right) \qquad odd\, p\; \&\; q$$

Equation 2.22

where the Talbot phase factor:

$$g(n; p, q) = g(0; p, q) exp[i\theta(n; p, q)]$$

Equation 2.23

is periodic in n with integer period $2q$ reflecting the transverse period Λ of the field. It is also periodic in p with integer period $2q$ reflecting the longitudinal period $2z_T$ of the field.

The common phase factor $g(0; p, q)$ is unimodular and given by the Gauss quadratic sum [48]:

$$g(0; p, q) = \frac{1}{q^{1/2}} \sum_{s=0}^{q-1} e^{-i\frac{\pi p}{q}s^2}$$

Equation 2.24

In Appendix I, it is shown that, for relatively prime p and q (i.e. p and q are integers with no non-trivial integer common factor), the Talbot phase may be evaluated using:

$$\theta(n; p, q) = p(p \setminus q)^2 \left(\frac{n}{2}\right)^2 \frac{\pi}{q} \qquad even\, n$$

$$\theta(n; p, q) = 4p(4p \setminus q)^2 n^2 \frac{\pi}{q} \qquad odd\, n$$

Equation 2.25

where $(p\backslash q)$ means the inverse of p modulo q:

$$(p\backslash q)p = 1\, mod\, q$$

Equation 2.26

and only exists if p & q are relatively prime.

For the purposes of this thesis it is the relative phase factor $exp[i\theta(n; p, q)]$ that is important and is evaluated in Table 2.1 for $p = 1$ and $q = 2, 3 \ldots, 8$.

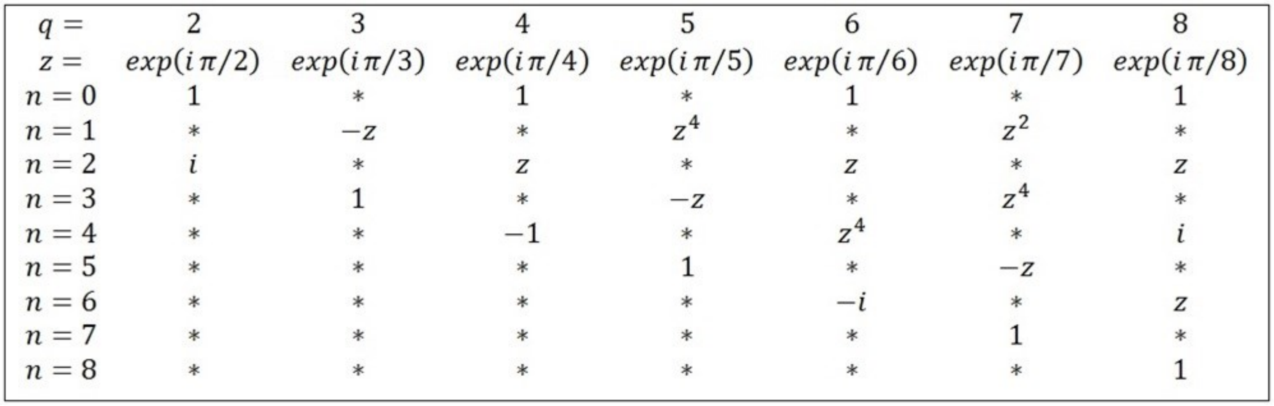

$q =$	2	3	4	5	6	7	8
$z =$	$exp(i\pi/2)$	$exp(i\pi/3)$	$exp(i\pi/4)$	$exp(i\pi/5)$	$exp(i\pi/6)$	$exp(i\pi/7)$	$exp(i\pi/8)$
$n = 0$	1	$*$	1	$*$	1	$*$	1
$n = 1$	$*$	$-z$	$*$	z^4	$*$	z^2	$*$
$n = 2$	i	$*$	z	$*$	z	$*$	z
$n = 3$	$*$	1	$*$	$-z$	$*$	z^4	$*$
$n = 4$	$*$	$*$	-1	$*$	z^4	$*$	i
$n = 5$	$*$	$*$	$*$	1	$*$	$-z$	$*$
$n = 6$	$*$	$*$	$*$	$*$	$-i$	$*$	z
$n = 7$	$*$	$*$	$*$	$*$	$*$	1	$*$
$n = 8$	$*$	$*$	$*$	$*$	$*$	$*$	1

Table 1. The Talbot phase factors for $p = 1$ and $q = 2, 3 \ldots, 8$

2.3 The Free-space Talbot Transfer Matrix

This section introduces an original concept: the free-space Talbot transfer matrix. This matrix provides a mapping between a set of point sources on a carefully chosen lattice in one transverse plane to their images on the same lattice in another transverse plane separated from the first by a rational fractional multiple of the Talbot distance. These matrices capture the self-imaging properties of the fractional Talbot effect.

As a consequence of its periodicity, the impulse response on a transverse plane located at $z = (p/q)z_T$, may be mapped as a distribution on a unit circle that is divided into a set of $2q$ regularly spaced points indexed by $n \in \mathbb{Z}_{2\mathrm{q}}$. The analysis in Appendix I shows the singular support of the Dirac distributions of the impulse response are located at the points with odd index when p and q are odd and even index when p or q is even. This is illustrated schematically in Fig 2.6.

Consider a periodic field of period Λ at the input plane. Suppose one period of the input consists of $2q$ regularly spaced point sources (Figure 2.7) modelled as Dirac distributions of weight a_n , $n \in \mathbb{Z}_{2\mathrm{q}}$, located on a regular lattice of pitch $\Lambda/2q$. The field at the input Talbot plane then admits the same representation as a set of distributions on a unit circle (Figure 2.8). By ensuring the pitch of the input and impulse response Dirac distributions are the same, the convolution of the input by the impulse response results in a multiple image of point sources (Figure 2.7) which may be modelled as Dirac distributions of amplitude weight b_n , $n \in \mathbb{Z}_{2\mathrm{q}}$ located on a regular lattice with the same pitch $\Lambda/2q$. Hence, the field at the output Talbot plane of interest admits the same representation as a set of distributions on a unit circle (Figure 2.8)

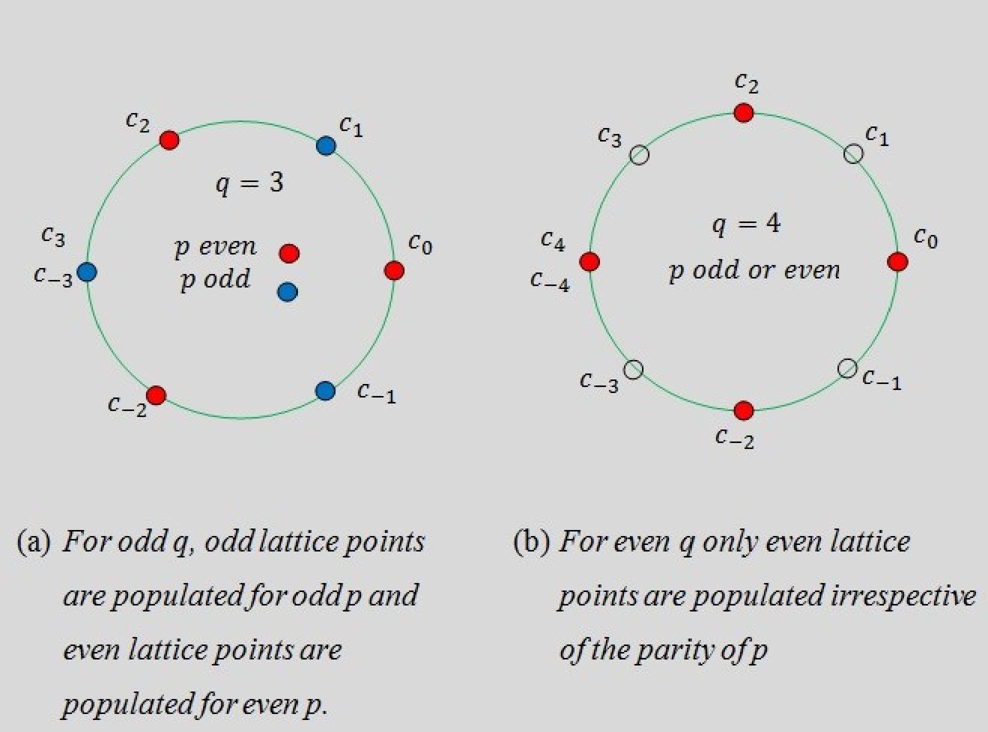

(a) *For odd q, odd lattice points are populated for odd p and even lattice points are populated for even p.*

(b) *For even q only even lattice points are populated irrespective of the parity of p*

Fig. 2.6. The impulse response evaluated in the fractional Talbot plane $z = (p/q)z_T$ represented as a distribution on a unit circle divided by a set of $2q$ regularly spaced points.

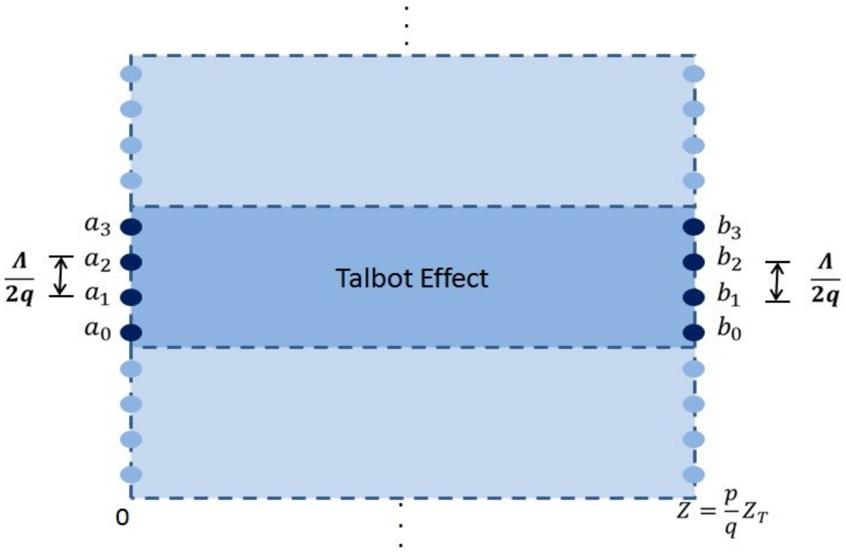

Fig.2.7. The fractional Talbot effect with point sources on a lattice of pitch $\Lambda/2q$ .The amplitude weights of the Delta distributions at lattice site n at the input and output are described by a_n, b_n respectively.

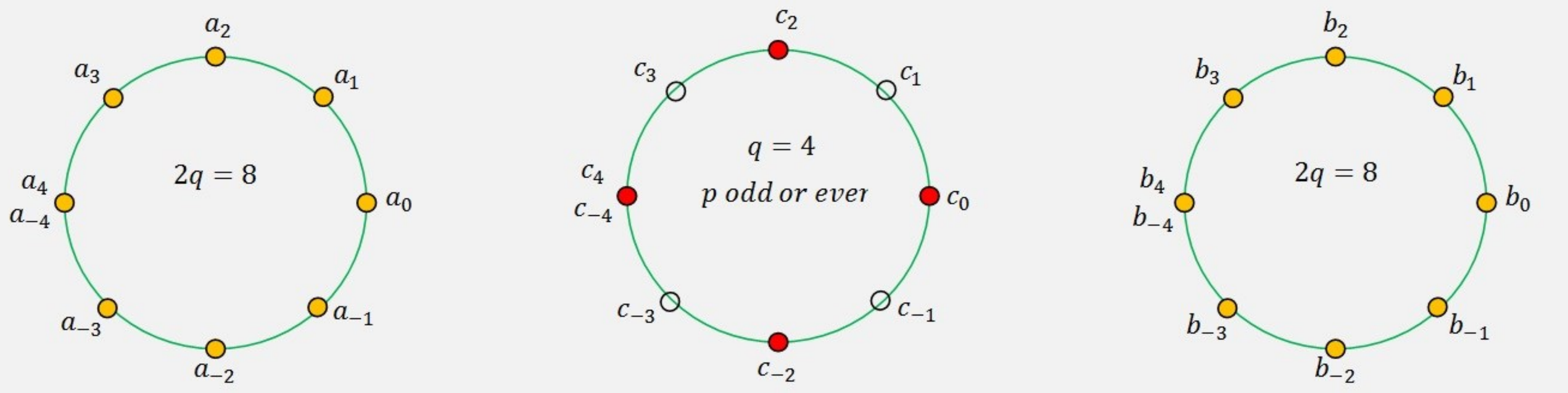

(a) Input lattice (q=4) populated by Dirac distributions of weight a_j

(b) Convolution kernel lattice (q=4) with even sites only populated by the Talbot impulse response Dirac distributions of weight c_{i-j}.

(c) Output lattice (q=4) for populated by Dirac distributions of weight b_i

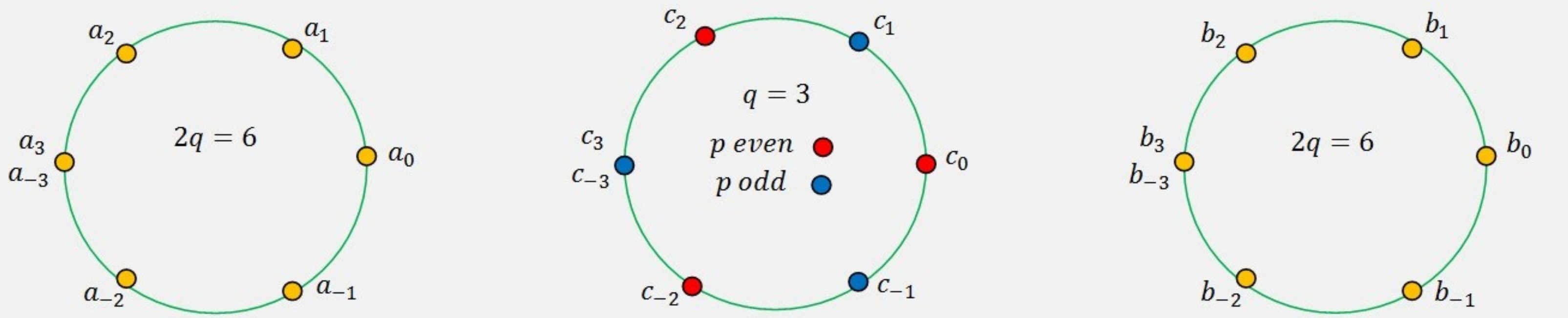

(d) Input lattice (q=3) populated by Dirac distributions of weight a_j

(e) Convolution kernel lattice (q=3) with even (even p) or odd (odd p) populated by the Talbot impulse response Dirac distributions of weight c_{i-j}

(f) Output lattice (q=3) for populated by Dirac distributions of weight b_j

Fig. 2.8. A depiction of the Fractional Talbot Effect as circular convolution. The input, Talbot impulse response & output distributions are all periodic with the same period. This may be visualised by wrapping a single period around a circle. Convolution is thereby transformed to circular convolution. The discrete supports of the distributions map the circular convolution into a matrix multiplication by a circulant matrix.

The convolution of two periodic functions results in a periodic function of the same period. In the case where the functions involved are distributions on a lattice, the amplitude weights compose as a discrete circular convolution.

$$\boldsymbol{b} = \boldsymbol{Ta}$$

Equation 2.27

where $\boldsymbol{a}$ and $\boldsymbol{b}$ are inputs and output vectors, respectively, representing the amplitude weights of the distributions and **T** is a circulant matrix with the Talbot phase factors as its entries:

$$T_{ij} = c_{i-j} = \frac{1}{\sqrt{q}} g(i-j;p,q)$$

Equation 2.28

For instance for $q = 3$, Equation 2.27 may be written:

$$\begin{bmatrix} b_{-3} \\ b_{-2} \\ b_{-1} \\ b_0 \\ b_1 \\ b_2 \end{bmatrix} = \begin{bmatrix} c_0 & c_{-1} & c_{-2} & c_{-3} & c_2 & c_1 \\ c_1 & c_0 & c_{-1} & c_{-2} & c_{-3} & c_2 \\ c_2 & c_1 & c_0 & c_{-1} & c_{-2} & c_{-3} \\ c_3 & c_2 & c_1 & c_0 & c_{-1} & c_{-2} \\ c_{-2} & c_3 & c_2 & c_1 & c_0 & c_{-1} \\ c_{-1} & c_{-2} & c_3 & c_2 & c_1 & c_0 \end{bmatrix} \begin{bmatrix} a_{-3} \\ a_{-2} \\ a_{-1} \\ a_0 \\ a_1 \\ a_2 \end{bmatrix}$$

Equation 2.29

where the red entries correspond to p or q even and the blue entries correspond to p and q odd.

Since $g(-n;p,q) = g(n;p,q)$ and consequently $c_{-n} = c_n$, Equation 2.29 can be simplified to a symmetric circulant matrix:

$$\begin{bmatrix} b_{-3} \\ b_{-2} \\ b_{-1} \\ b_0 \\ b_1 \\ b_2 \end{bmatrix} = \begin{bmatrix} c_0 & c_1 & c_2 & c_3 & c_2 & c_1 \\ c_1 & c_0 & c_1 & c_2 & c_3 & c_2 \\ c_2 & c_1 & c_0 & c_1 & c_2 & c_3 \\ c_3 & c_2 & c_1 & c_0 & c_1 & c_2 \\ c_2 & c_3 & c_2 & c_1 & c_0 & c_1 \\ c_1 & c_2 & c_3 & c_2 & c_1 & c_0 \end{bmatrix} \begin{bmatrix} a_{-3} \\ a_{-2} \\ a_{-1} \\ a_0 \\ a_1 \\ a_2 \end{bmatrix}$$

Equation 2.30

2.4 The Talbot Effect in a Multimode Waveguide

2.4.1 Self-imaging in Multimode Waveguides

The free-space Talbot effect may be mapped to a description of the self-imaging properties of planar multimode waveguides. The multiple imaging property of multimode waveguides was first demonstrated by Ulrich and Ankele in planar glass waveguides [49], [50]. They used a ray tracing formalism to explain the formation of multiple images at a specific distance. This was a starting point for the development of Multimode Interference couplers (MMI) [51]. An $N \times M$ MMI consists of a multimode waveguide section of carefully chosen length with one or more, usually monomode, waveguides placed at each end that form N input and M output ports of the MMI. [52], [53].

Figure 2.9 illustrates the transverse form of the field amplitude of the first few lowest order eigenmodes with mode index ν propagating along the z-axis of a multimode waveguide section.

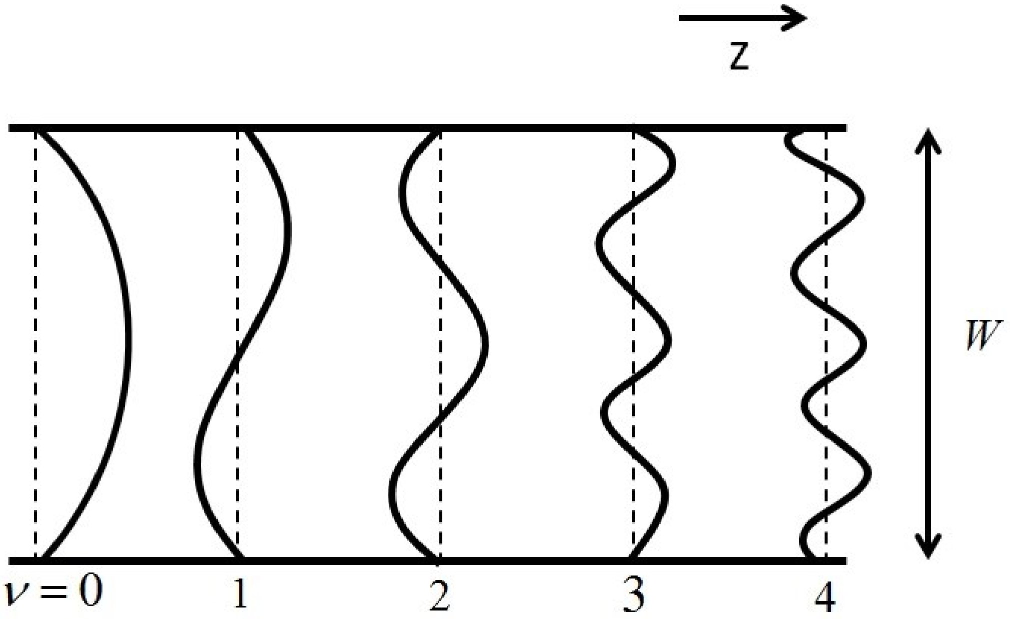

Fig. 2.9. The form of the field amplitude of the first few lowest order transverse modes indexed by ν which propagate along the z-axis of a multimode waveguide with width W.

At each transverse plane along the axis, the field consists of a superposition of the eigenmodes. Each of these eigenmodes propagates independently, acquiring a phase delay that depends upon their associated propagation constant (eigenvalue). At certain positions along the axis, the phases of the modes can take on particular relative values that create a field consisting of the superposition of one or more images of the input field. In general, the component images are translated in the transverse plane differently and possess different overall complex amplitudes [51-53].

In the case where there is a high refractive index contrast between the material interior and exterior to the waveguide sidewalls, the evanescent fields rapidly decay away from the sidewalls on the scale of a wavelength. The field amplitude is then close to zero at the sidewalls which behave essentially as mirrors. The multimode waveguide thereby has a structure analogous to a kaleidoscope which provides a heuristic explanation of the multiple self-imaging phenomena observed.

In this tight confinement limit, the field amplitude of the modes ψ_ν in the interior of the waveguide is given by:

$$\psi_\nu(x,z) = \begin{cases} cos(\eta\kappa x)exp\left(i\beta_\eta z\right) & \eta = \nu + 1 = 2m \\ sin(\eta\kappa x)exp\left(i\beta_\eta z\right) & \eta = \nu + 1 = 2m + 1 \end{cases} \qquad -\frac{W}{2} \leq x < \frac{W}{2} \quad \kappa = \frac{2\pi}{2W}$$

Equation 2.31

where the origin of the transverse co-ordinate has been taken as the mid-point between the waveguide sidewalls. These modes may therefore be expressed using a plane wave basis:

$$\left.\begin{aligned} \varphi_n(x,z) &= exp(in\kappa x)exp(i\beta_n z) \\ \beta_n &= \sqrt{k^2 - n^2\kappa^2} \\ k &= \frac{2\pi}{\lambda} \\ \kappa &= \frac{2\pi}{\Lambda} \end{aligned}\right\} \quad \begin{gathered} n = 0, \pm 1, \pm 2 \ldots \\ \lambda = \frac{\lambda_0}{n_{core}} \\ \Lambda = 2\mathrm{W} \end{gathered}$$

Equation 2.32

where n_{core} is the refractive index of the waveguide core (not to be confused with n which is used as an integer index in this chapter).

Any function represented using this basis within the region $x \in \left[-\frac{1}{2}W, \frac{1}{2}W\right]$ extends naturally outside this region as a periodic function of period $\Lambda = 2\mathrm{W}$.

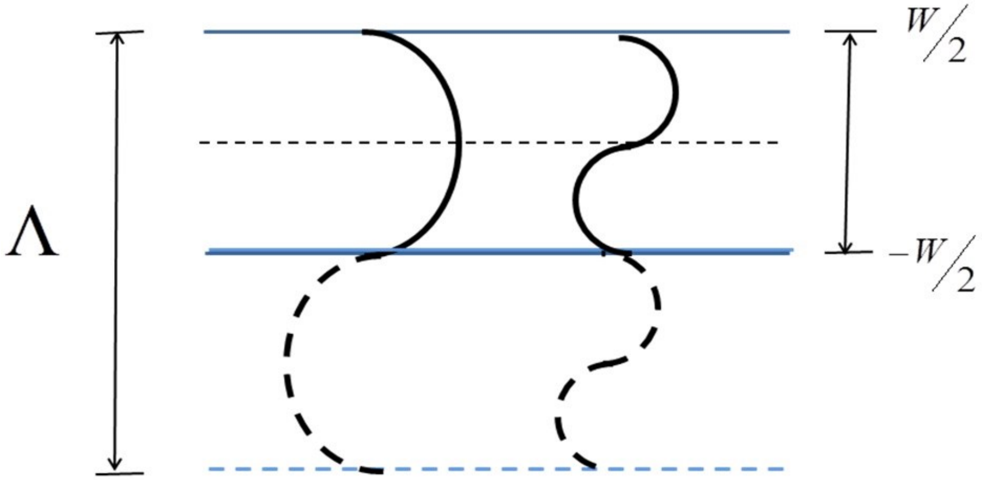

Fig. 2.10. A unit cell of width $\Lambda = 2\mathrm{W}$ consisting of a real waveguide of width W (solid lines) alongside a virtual anti-symmetric partner waveguide (long dashes). The lower sidewall of the real waveguide acts as a mirror which enforces an anti-symmetric field in the unit cell about the lower waveguide sidewall. It can be seen that the upper sidewall also enforces an anti-symmetric field in the unit cell when the lower (virtual) and upper (real) boundaries of the unit cell are identified. This is equivalent to an infinitely extended homogenous medium with 2W periodic fields anti-symmetric about the axes defined by the replication of the sidewall locations.

In the context of modelling a strongly confining multimode waveguide section, the waveguide field extends periodically as an anti-symmetric function about the real sidewalls and their periodic replications. The unit cell is therefore of width $\Lambda = 2\mathrm{W}$ and is anti-symmetric about an axis coinciding with a sidewall. It is therefore convenient to define a new co-ordinate system with the sidewall located at $x = 0$.

With reference to Figure 2.10, a unit cell can be constructed by placing the real waveguide alongside a virtual partner waveguide with anti-symmetric excitation about a sidewall. The periodic replication of this structure (Figure 2.11) yields a *homogenous* medium with a periodic initial field. The propagation of this initial field is then formally identical to the problem of propagating the periodic initial field in the Talbot effect. The anti-symmetry of the initial field of the unit cell takes care of the boundary condition at the sidewalls of the real waveguide and the setting of the 'free-space' wavelength λ equal to the reduced vacuum wavelength λ_0/n_{core} and the transverse period Λ to twice the waveguide width $2W$ takes care of the waveguide dimensions and material.

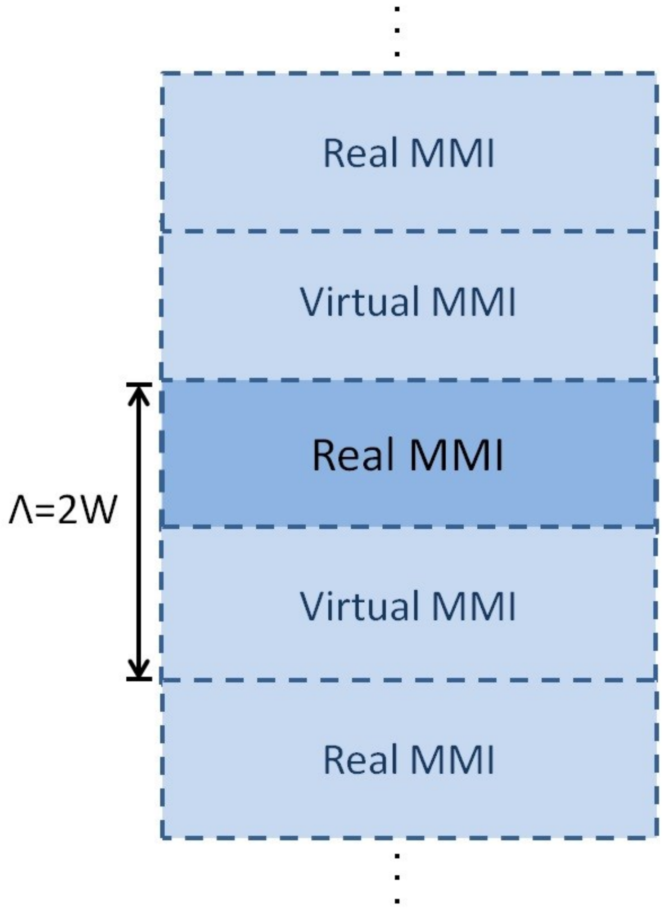

Fig. 2.11. A periodic structure unit cell of width 2W consisting of the multimode waveguide section of the real MMI (dark blue) alongside an anti-symmetric partner virtual multimode waveguide section (adjacent pale blue rectangle). The infinitely replicated unit cell corresponds to a homogeneous material excited by an initial field of period 2W that is anti-symmetric about any axis corresponding to the image of a sidewall (horizontal dashed lines) under the replication

Figure 2.12 shows the free-space Talbot carpet for a point source with an anti-symmetric partner point source located at the input at the mid-points of the upper and lower halves of the unit cell. The carpet can be observed to have zero lines on the axis and the upper or lower boundaries of the unit cell (which are equivalent). The zero fields at the sidewalls of the multimode section of a real MMI are therefore correctly modelled by taking either the upper or lower half of the unit cell to correspond to the real MMI with the corresponding initial field.

Self-images of the initial field can be observed at regular intervals along the z-axis. The particular position where the point sources are placed suppresses the excitation of all the odd order modes of the modelled real multimode waveguide section. The excited modes therefore correspond to plane waves with transverse wave numbers equal to $2n\kappa$. The Talbot distance is thereby equivalently reduced by fourfold compared to the case for general excitation. This accounts for the eight self-imaging planes seen in Fig. 2.12 (b) compared to the two seen in Figure 2.12 (a). Figure 2.12 also demonstrates that the transverse translation invariance of the free-space Talbot effect is broken in the waveguide Talbot effect by the sidewall mirrors. Both figures were generated to the same scales by the same Matlab script.

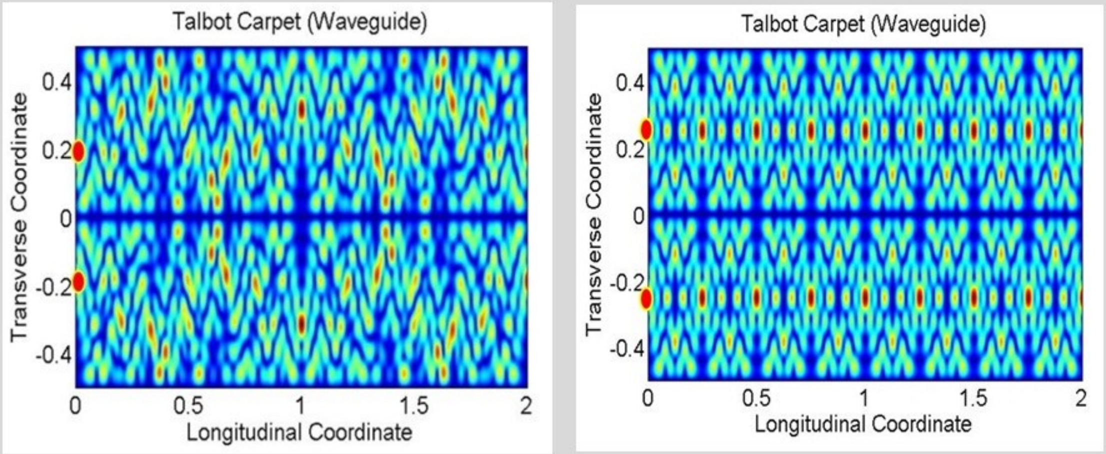

(c) The multimode field excited by a point source at the input $z = 0$ *at an offset from the central axis of* $x = 0.1875$. *Note the primary image at* $z = 2$ *and the secondary image at* $z = 1$

(d) *The multimode field excited by a point source at the input* $z = 0$ *at an offset from the central axis of* $x = 0.25$. *Selective excitation results in an apparent fourfold reduction of the Talbot distance.*

Fig. 2. 12. The Talbot carpet for a multimode slab waveguide. The images show one elementary unit cell formed from a real multimode waveguide of width W alongside its virtual anti-symmetric partner. The zero-field on the axis and at the two boundaries enforced by the mirror symmetry can be observed. The boundaries should be identified as a consequence of periodicity. Comparison of the two images illustrates that the (circular) translation symmetry has been broken by the mirror symmetry. The transverse co-ordinate is in units of the period $\Lambda = 2\mathrm{W}$ and the longitudinal co-ordinate is in units of the Talbot distance $\mathrm{z_T} = \Lambda^2/\lambda$ where $\lambda = \lambda_0/\mathrm{n_{eff}}$, λ_0 is the vacuum wavelength and $\mathrm{n_{eff}}$ is the effective index of the fundamental mode of the slab waveguide.

In the literature [54], self-imaging distances are expressed in terms of the beat length L_π between the two lowest order modes. Now, from Equation 2.32:

$$\begin{gathered}\beta_n - \beta_m \approx (m^2 - n^2)\pi\frac{\lambda}{\Lambda^2}\\ \Longrightarrow\\ L_\pi = \frac{\pi}{\beta_1 - \beta_2} = \frac{1}{3}\frac{\Lambda^2}{\lambda} = \frac{1}{3}z_T\end{gathered}$$

Equation 2.33

The Talbot distance is therefore three times the beat length:

$$z_T = 3L_\pi$$

Equation 2.34

The position of the multiple self-imaging planes predicted in this work is therefore in full agreement with the literature on multiple self-imaging in MMI couplers [51-53].

2.4.2 MMI Transfer Matrices

Transfer matrices for MMIs were first introduced by Heaton [53]. The Talbot matrices introduced in this thesis are their equivalent in the context of the free-space Talbot effect. It has been established that the self-imaging in multimode waveguides may be modelled as a special case of the Talbot effect in free-space. It follows that the MMI transfer matrices may be related to the Talbot matrices.

Recall that the Talbot matrices $\boldsymbol{T}$ of dimension $2q \times 2q$ relate a vector $\boldsymbol{a}$ of dimension $2q$ that represents a set of point sources located at the points of a lattice with a pitch $(\Lambda/2q)$ that generate the field to a vector $\boldsymbol{\mathscr{b}}$ that represents the multiple images of these point sources after propagation of a distance $z = (p/q)z_T$. Since the Talbot matrix is symmetric and persymmetric, (symmetric about the trailing diagonal), it commutes with the exchange matrix $\boldsymbol{J}$ (a matrix involution with unit entries in the trailing diagonal and zero entries elsewhere). Hence:

$$\begin{gathered}\boldsymbol{\mathscr{b}} = \boldsymbol{T}\boldsymbol{a}\\ \Longrightarrow\\ \boldsymbol{J}\boldsymbol{\mathscr{b}} = \boldsymbol{T}\boldsymbol{J}\boldsymbol{a}\\ \frac{1}{2}(\boldsymbol{I} \pm \boldsymbol{J})\boldsymbol{\mathscr{b}} = \frac{1}{2}\boldsymbol{T}(\boldsymbol{I} \pm \boldsymbol{J})\boldsymbol{a}\end{gathered}$$

Equation 2.35

That is the symmetric $(+)$ and anti-symmetric (-) parts of the field distributions are separately solutions.

The exchange operator $\boldsymbol{J}$ is a $2q \times 2q$ matrix that admits the decomposition:

$$\boldsymbol{J} = \begin{bmatrix} \mathbf{0} & \boldsymbol{J} \\ \boldsymbol{J} & \mathbf{0} \end{bmatrix}$$

Equation 2.36

where the entries in the matrix on the right hand side are $q \times q$ matrices[1].

In the case of an MMI the fields are anti-symmetric about the sidewall between the real and virtual regions of the unit cell hence using Equation 2.35 the field vectors may be represented by:

$$\boldsymbol{\mathscr{a}} = \begin{bmatrix} -\boldsymbol{J}\boldsymbol{a} \\ \boldsymbol{a} \end{bmatrix}$$
$$\boldsymbol{\mathscr{b}} = \begin{bmatrix} -\boldsymbol{J}\boldsymbol{b} \\ \boldsymbol{b} \end{bmatrix}$$

Equation 2.37

As a consequence of the transverse translation invariance of the free-space problem the mirror plane can pass through the transverse lattice anywhere; between lattice points or even through a lattice point. In this thesis it has been chosen to pass midway between lattice points. As a consequence the MMIs modeled may have single mode access waveguide ports centred on the q lattice points that fall within the real waveguide region and there are no unusable half-ports. The formulism does encompass the most common multiport structures. However, MMIs with a port centred on the input face such as a 1×2 symmetric coupler are excluded from the formulism and must be treated separately.

The Talbot transfer matrix is also partition in a way consistent with Equation 2.37

$$\boldsymbol{T} = \begin{bmatrix} \boldsymbol{V} & \boldsymbol{W} \\ \boldsymbol{W} & \boldsymbol{V} \end{bmatrix}$$

Equation 2.38

where $\mathbf{V}$ and $\mathbf{W}$ are $q \times q$ symmetric Toeplitz matrices that inherit the property of commutating with the exchange operator:

$$\boldsymbol{V}\boldsymbol{J} = \boldsymbol{J}\boldsymbol{V}$$

$$\boldsymbol{W}\boldsymbol{J} = \boldsymbol{J}\boldsymbol{W}$$

Equation 2.39

As an example, consider the case $q = 3$ for which the Talbot transfer matrix takes the form:

---

[1] For ease of notation, matrix objects of similar function but different dimension may have the same symbol as the dimension is clear from the context.

$$\boldsymbol{T} = \begin{bmatrix} c_0 & c_1 & c_2 & c_3 & c_2 & c_1 \\ c_1 & c_0 & c_1 & c_2 & c_3 & c_2 \\ c_2 & c_1 & c_0 & c_1 & c_2 & c_3 \\ c_3 & c_2 & c_1 & c_0 & c_1 & c_2 \\ c_2 & c_3 & c_2 & c_1 & c_0 & c_1 \\ c_1 & c_2 & c_3 & c_2 & c_1 & c_0 \end{bmatrix}$$

Equation 2.40

where the red entries are non-zero for p or q even and the blue entries are non-zero for p and q odd. Hence:

$$\boldsymbol{V} = \begin{bmatrix} c_0 & c_1 & c_2 \\ c_1 & c_0 & c_1 \\ c_2 & c_1 & c_0 \end{bmatrix}$$

$$\boldsymbol{W} = \begin{bmatrix} c_3 & c_2 & c_1 \\ c_2 & c_3 & c_2 \\ c_1 & c_2 & c_3 \end{bmatrix}$$

Equation 2.41

therefore, Equation 2.35 may be written:

$$\begin{bmatrix} -\boldsymbol{Jb} \\ \boldsymbol{b} \end{bmatrix} = \begin{bmatrix} \boldsymbol{V} & \boldsymbol{W} \\ \boldsymbol{W} & \boldsymbol{V} \end{bmatrix} \begin{bmatrix} -\boldsymbol{Ja} \\ \boldsymbol{a} \end{bmatrix}$$

Equation 2.42

as a consequence, it separates into the two equations:

$$\begin{gathered} -\boldsymbol{Jb} = -\boldsymbol{VJa} + \boldsymbol{Wa} \\ \Rightarrow \\ \boldsymbol{b} = [\boldsymbol{JVJ} - \boldsymbol{JW}]\boldsymbol{a} \end{gathered}$$

Equation 2.43

and

$$\begin{gathered} \boldsymbol{b} = -\boldsymbol{WJa} + \boldsymbol{Va} \\ \Rightarrow \\ \boldsymbol{b} = [\boldsymbol{V} - \boldsymbol{WJ}]\boldsymbol{a} \end{gathered}$$

Equation 2.44

which agree by virtue that $\mathbf{V},\ \mathbf{W}$ commute with $\mathbf{J}$ and $\mathbf{J}$ is an involution.

The MMI transfer matrix may therefore be represented as:

$$\boldsymbol{T}_{\boldsymbol{MMI}} = \boldsymbol{V} - \boldsymbol{WJ}$$

Equation 2.45

where $\boldsymbol{V}$, $\boldsymbol{W}$ are the projections of the Talbot matrix $\boldsymbol{T}$ given by the partition defined by Equation 2.38.

Returning to the example:

$$\boldsymbol{T}_{\boldsymbol{MMI}} = \begin{bmatrix} c_0 & c_1 & c_2 \\ c_1 & c_0 & c_1 \\ c_2 & c_1 & c_0 \end{bmatrix} - \begin{bmatrix} c_3 & c_2 & c_1 \\ c_2 & c_3 & c_2 \\ c_1 & c_2 & c_3 \end{bmatrix} \begin{bmatrix} 0 & 0 & 1 \\ 0 & 1 & 0 \\ 1 & 0 & 0 \end{bmatrix}$$

$$\Rightarrow$$

$$\boldsymbol{T}_{\boldsymbol{MMI}} = \begin{bmatrix} c_0 & c_1 & c_2 \\ c_1 & c_0 & c_1 \\ c_2 & c_1 & c_0 \end{bmatrix} - \begin{bmatrix} c_1 & c_2 & c_3 \\ c_2 & c_3 & c_2 \\ c_3 & c_2 & c_1 \end{bmatrix}$$

Equation 2.46

Consequently the $\boldsymbol{T}_{\boldsymbol{MMI}}$ matrix is fully populated irrespective of the parity of p and q.

$$\boldsymbol{T}_{\boldsymbol{MMI}} = \begin{bmatrix} c_0 & -c_2 & c_2 \\ -c_2 & c_0 & -c_2 \\ c_2 & -c_2 & c_0 \end{bmatrix} \quad even\ p\ or\ q$$

$$\boldsymbol{T}_{\boldsymbol{MMI}} = \begin{bmatrix} -c_1 & c_1 & -c_3 \\ c_1 & -c_3 & c_1 \\ -c_3 & c_1 & -c_1 \end{bmatrix} \quad odd\ p\ and\ q$$

Equation 2.47

The MMI transfer matrices inherit from the Talbot transfer matrix the property of having equal magnitude non-zero entries when p and q are relatively prime integers and the properties of being symmetric, persymmetric, and unitary. The Toeplitz property of the Talbot transfer matrix is not inherited consequent on the breaking of the translation symmetry by the sidewalls.

Suppose $\boldsymbol{T}_{MMI}$ corresponds to $p = 1$, then $\boldsymbol{T}_{MMI}^{p}$ is the Talbot transfer matrix for p equal to any integer even when p and q have common factors; in particular:

$$\boldsymbol{T}_{MMI}^{2q} = exp(i\varphi)\boldsymbol{I}$$

Equation 2.48

where φ is some overall phase[2]. The MMI transfer matrices modulo an overall phase factor therefore form a cyclic group.

---

[2] The overall phase plays no role in determining the intensity or relative phases of the light from the output ports. It will only have an impact if the MMI is placed within an interferometer of some kind. The overall phase can be accounted for by keeping track of the phase advance due to propagation along the axis and the phase of the Gauss sum. It is however simpler to define the transfer matrices as equivalence classes of matrices that differ only by a common phase.

2.5 Summary & Discussion

In this chapter it has been shown that the Talbot effect in free space provides an elegant description of MMI self-imaging phase relationships. By a particular choice of a transverse plane and a lattice of point sources, a circulant symmetric transfer matrix with Talbot phase factors as its entries has been introduced. It was found that $2q \times 2q$ Talbot effect transfer matrices map simply to $q \times q$ MMI transfer matrices. The nice properties of these transfer matrices facilitates the phase computations in coherent optical applications of MMI structures such as the generalised Mach-Zehnder based phased array beam-steering switches treated in the next chapter.

Chapter 3. The Optical Switch Architecture

3.1 Introduction

Chapter 1 provided some background and selected state-of-the-art on optical switches that motivated transparent route & select optical switch architectures that employ optical phased array (OPA) beam forming methods. Generalised Mach-Zehnder Interferometer (GMZI) switch elements were introduced as a specific embodiment of an OPA in the form of a planar Photonic Integrated Circuit (PIC). The GMZI structure consists of an array of phase-shift elements that connect two Multi-Mode Interference (MMI) couplers that respectively distribute light from an input port to the phase shift element array and then form the superposition of the output of the phase shift elements at each output port. In Chapter 2 the Talbot effect in free space was discussed and was mapped to the waveguide Talbot effect with a specific emphasis on the determination of the MMI port phase relations. Well defined and stable MMI port phase relations are critical to the operation of the GMZI structure as a $1 \times N$ route or an $N \times 1$ select switch.

This chapter elaborates on how the basic elements of the switch architecture combine to form an $N \times N$ optical route & select switch. In Section 3.2 the GMZI structure architecture is introduced, the role of its constituent components is described, and the principles of its operation are explained. The design principles of practical MMI couplers are outlined; a comparison is made between the predictions of the theory and the numerical simulation of the MMI port phase relations; and strategies for the mitigation of impairments are discussed. In Section 3.3 an architecture for an Optical Transpose Interconnection System (OTIS) is introduced, which may combine the route switch elements and the select switch elements into a $N \times N$ switch fabric while avoiding problems associated with very large numbers of crossover interconnects. The OTIS was conceived as a 3D free-space optical interconnection system employing bulk optics and, specifically, optical elements with rotational symmetry about an axis. In Section 3.4 in an original contribution; the architecture is adapted to spherically symmetric Lüneburg lenses and its operation verified for circularly symmetric cylindrical Lüneburg lenses by 2D FDTD simulation. This chapter closes with a summary in Section 3.5 of the most significant results. The considerations in this chapter provide the foundation for a planar implementation of the OTIS described in Chapter 4.

3.2 Generalised Mach-Zehnder Interferometer Switch Element

3.2.1 Switch Element Architecture & Operation

A $N \times N$ Generalized Mach-Zehnder Interferometer (GMZI), consists of an array of M independently controllable waveguide phase shift elements placed between a $N \times M$ MMI and a $M \times N$ MMI where $M \geq N$. Most often $M = N$ and both MMIs are of identical design with N input and N output ports although, typically, only one input port of the first MMI is used. A schematic of an example of a 4×4 GMZI is shown in Figure 3.1.

The MMIs are designed to direct a precisely equal fraction of the power entering each of their input ports to each of their output ports. The relative phase differences between the MMI ports are then intrinsic to the MMI and very well controlled over a broad bandwidth. The optical power injected into one port of the first MMI is equally split between the M waveguide phase modulators. The $M \times N$ coupler at the output re-combines the optical beams. The role of the phase shift elements is to control the interference at each output port and thereby directing the input light to the desired output port.

Jenkins *et al* [28] demonstrated 10×10 and 1×10 GMZI switches on a GaAs material integration platform. Switching uniformity, maximum crosstalk, and insertion loss levels achieved were $+9$ %, -10 dB, and -12 dB, respectively. Tomofuji *et al* [29] demonstrated a 1×4 GMZI on an InP material integration platform. A crosstalk and an extinction ratio level of -14.47 dB and 23.39 dB, was measured respectively. In addition, they demonstrated dynamic switching with a rise and fall time of ~ 1 ns. Wang *et al* [30] demonstrated a 1×3 GMZI on a CMOS compatible Si material integration platform. A crosstalk and an extinction ratio level achieved 21.9 dB and 22.9 dB, respectively, at a wavelength of 1550 nm. Jin *et al* [31] reported the results of a design study for a low-contrast SiO_x/Si material integration platform. The feasibility is claimed of switches of dimension up to 1×32 with insertion losses of $1\ dB$ and crosstalk as low 31.7 dB.

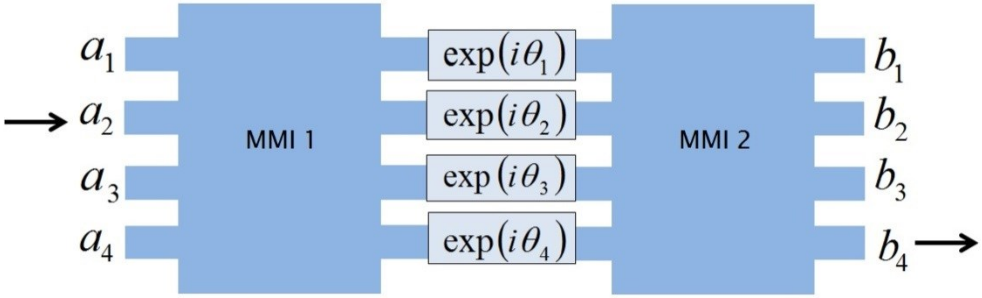

Fig. 3.1. A schematic diagram of a 1×4 planar waveguide optical phased array switch using a generalised Mach-Zehnder interferometer structure. a_n and b_n are the overall complex amplitudes of the monomode fields of the input and output access waveguides respectively. The phase shift elements are located on arms that connect the ports of the two MMIs. By appropriate setting of the phase shifts, the beam entering input port 2, exits from output port 4

To understand the switching operation, consider the transfer matrix $\boldsymbol{T}$ that characterises the two MMIs. Ideally there is no loss[3] and $\boldsymbol{T}$ unitary:

$$\boldsymbol{T}^{\dagger}\boldsymbol{T} = \boldsymbol{I}$$

Equation 3.1

where † denotes the adjoint (Hermitian transpose) operation. The reversible MMI design and the reciprocity property of electromagnetic scattering also ensure that the transfer matrix is symmetric (see Appendix II):

$$\boldsymbol{T}^{t} = \boldsymbol{T}$$

Equation 3.2

where t specifies the real transpose operation on the matrix.

Hence:

$$\boldsymbol{T}^{-1} = \boldsymbol{T}^{\dagger} = (\boldsymbol{T}^{t})^{*} = \boldsymbol{T}^{*}$$
$$\Longrightarrow$$
$$\boldsymbol{b} = T\boldsymbol{a} \;\; => \;\; \boldsymbol{a}^{*} = T\boldsymbol{b}^{*}$$

Equation 3.3

In other words, if an optical excitation defined by the vector of amplitudes $\boldsymbol{a}$ is applied to the input ports of an MMI and thereby produces an optical output defined by the vector of amplitudes $\boldsymbol{b}$**,** then an optical excitation defined by the vector of amplitudes $\boldsymbol{b}^{*}$ applied to the

---

[3] If there is uniform loss then $\boldsymbol{T}$ remains proportional to a unitary matrix.

input ports of the same MMI produces an optical output defined by the vector of amplitudes $\boldsymbol{a}^*$**.** This symmetry is illustrated in Figure 3.2 for extra clarity.

As a consequence, one needs to consider only the output due to the excitation of a single input port to know the excitation needed to be applied to each input port to ensure that all the light is steered to a single corresponding output port.

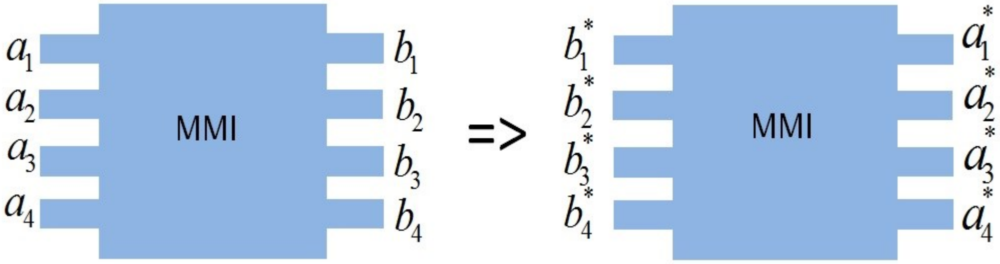

Fig. 3.2. The MMI on the left transforms a set of input amplitudes, $\boldsymbol{a}$, to a set of output amplitudes, $\boldsymbol{b}$**.** If these are conjugated to $\boldsymbol{b}^*$ and applied to the input of an identical MMI on the right, they are transformed into a set of output amplitudes, $\boldsymbol{a}^*$, equal to the complex conjugate of the original input amplitude, $\boldsymbol{a}$.

Let $\boldsymbol{e_n}$ denote a vector of amplitudes with all zero entries except for a unit in position n.

Suppose one wishes that light applied to input port n is steered only to output port m. That is:

$$\begin{gathered} \boldsymbol{b}_L = \boldsymbol{T}\boldsymbol{a}_L = \boldsymbol{T}\boldsymbol{e_n} \\ \boldsymbol{b}_R = \boldsymbol{T}\boldsymbol{a}_R = \boldsymbol{e_m} \\ \Longrightarrow \\ \boldsymbol{a}_R = (\boldsymbol{T}\boldsymbol{e_m})^* \end{gathered}$$

Equation 3.4

where the subscript L, R refers to the MMI on the left or right of Fig.3.2, respectively.

Let $\boldsymbol{D}$ denote a diagonal matrix that describes the action of the phase shift array with non-zero entries:

$$D_{jj} = exp(i\theta_j)$$

Equation 3.5

The problem is therefore solved by choosing $\boldsymbol{D}$ so that it satisfies:

$$(\boldsymbol{Te_m})^* = \boldsymbol{DTe_n}$$
$$\Longrightarrow$$
$$exp(i\theta_j) = \frac{T_{jm}^*}{T_{jn}}$$

Equation 3.6

From Chapter 2, it is known that the elements of the transfer matrices have equal magnitude entries with phases that are quantised. Hence the phase states required of the phase shift elements to perform beam steering are similarly quantised.

3.2.2 The Phase Shift Element

When contemplating a silicon photonics implementation of the phase shift element arrays, three options present themselves that differ in the physical mechanism responsible for the phase change of the light in the waveguide: thermo-optic; electro-optic; opto-mechanical.

Silicon is a material with a high thermo-optic coefficient of refractive index.

$$\frac{dn}{dT} = 1.84.10^{-4}K^{-1} \qquad at\ \lambda = 1.5\mu m$$

Equation 3.7

It is therefore possible to temperature tune the optical path-length of a section of waveguide. In practice, a heater element is fabricated over a waveguide section so that when a controlled current is applied the temperature rise causes a large refractive index change without significant optical loss [25]. The speed of operation is low (~ 1 ms) and the power consumption high (~ 10 mW per element). The merit of the approach is its simplicity.

Since silicon has a centro-symmetric crystal structure, it lacks a linear electro-optic effect. The only recourse has been to the weak plasma dispersion effect which involves the variation of the refractive index by the injection or depletion of charge carriers usually via a *p-n* or *p-i-n* junction integrated into the waveguide structure. It has been a considerable challenge to avoid carrier induced excess absorption, slow effects due to resistive heating by forward currents or difficulties removing excess charge (injection), and the difficulty of fabricating depletion mode devices. High speed electro-optical modulators are an enabling technology for the deployment of future coherent telecommunication systems operating at 100 Gbps and beyond [55]. Spurred on by this imperative combined with the economic promise of CMOS compatibility, remarkable progress has been achieved [7-16]. Bandwidths of up to 42.7 GHz

[10]; half-wave voltage unit interaction length product as low as 2 V*mm* [13], and RF energy consumption as low as 200 fJ/bit [14] have been achieved. In the context of this thesis the major issue with electro-optic modulators in silicon is the device footprint which is measured in millimetres compared to the MMI and photonic wire waveguide dimensions that are measured in microns. In particular, the aspect ratio of these devices does not allow the phase shift array pitch to match the MMI access waveguide pitch. It is therefore necessary to use a waveguide tree to break-out the waveguides from the MMI without imbalance to the optical path-lengths. Any errors in the path length balance thereby caused compromise the well-defined intrinsic phase relations provided by the MMI couplers.

Acoleyen et al [56] recently introduced a new nano-electro-mechanical-system (NEMS) approach that achieves phase modulation by varying the gap width of a suspended slotted waveguide using electrostatic forces. The minute mass of the cantilevers than make up the two halves of the slotted waveguide lead to a mechanical resonant frequency of the order of 100 MHz. As a consequence sub-microsecond switching times are feasible even with this mechanical approach. Furthermore, the device is ultra compact with a length of a few tens of micrometres and a width only slightly wider than the optical waveguide which better matches the pitch of the MMI access ports.

Although active device design falls outside the scope of this thesis, this brief survey of the state of the art of active phase modulators shows that implement options exist now for a GMZI that can switch on sub-microsecond and even nanosecond timescales. Moreover, progress is so rapid that one may anticipate the same performance in increasingly compact device footprints.

3.2.3 The Multi-Mode Interference Couplers

The MMI couplers form the heart of the GMZI structure. The basic principles that underpin their operation have been explained in Chapter 2 in the context of the Talbot effect. The achievement of the desirable properties of low excess loss, uniformity of power splitting, and precisely defined port phase relationships depends critically upon the validity of the quadratic dependence with mode number of the differences between the mode propagation constants expressed by Equation 2.33. The quadratic dependence rests on the assumption of tight confinement and the paraxial approximation both of which become questionable as the mode number increases. As a consequence the number of modes supported in the multimode region is limited by design. However, there must be enough modes to describe well the field presented by the access guides to the MMI to ensure minimal transmission loss and reflections. The access guides are therefore tapered to maximally expand the access port mode to ensure it is well represented by a superposition of only a few modes of the multimode region. Typically, the taper expands sufficiently that it can support higher order modes. To avoid the fundamental mode in the access guide being converted to the higher order modes within the taper, care must be taken to ensure the taper is adiabatic. Finally, the access waveguides must be sufficiently separated that coupling between them outside the multimode region is negligible. Halir *et al* [56] provide details of the design procedure for high performance MMI couplers.

Although the theory provides vital design guidelines, the assumptions necessary for a tractable theory are not accurate in practice and hence numerical simulation tools must be used for the precise design of MMI couplers. The principal tool used to generate the results in this thesis is FimmProp, part of the Photon Design suite of tools, which can model a variety of 2D and 3D waveguide structures. The Finite Difference Mode (FDM) numerical mode solver was employed in all the simulation results presented herein. This solver models accurately waveguides with high step refractive index profiles. Figure 3.3 shows the slab waveguide layers used to define the MMI structure. The waveguide structure is defined to be compatible with Silicon on Insulator (SOI) with standard parameters: 220 nm thick silicon layer above a 2 μm thick buried oxide layer (silica).

Consider a 1×4 MMI with a multimode waveguide region of width 5.25 μm, and input and output access waveguides of width 1 μm. In the simulations only the fundamental mode of these access waveguides is excited in order to emulate adiabatic tapers which are separately designed and optimised. This is done to avoid the co-simulation of tapered access ports and the multimode waveguide region which is too computationally demanding. The beat length L_π is found from Equation 2.33 to be 67.853 μm given the propagation constants of the two lowest order modes of the multimode waveguide region of $\beta_0 = 11.4817\ \mu\text{m}^{-1}$ and $\beta_1 = 11.4354\ \mu\text{m}^{-1}$ which correspond to an effective refractive index for the fundamental mode of 2.832 and for the second order mode of 2.821 at a vacuum wavelength of $\lambda_0 = 1550$ nm. Hence, the Talbot distance Z_T is obtained as 203.56 μm and the primary self-imaging distance $2 \times Z_T = 407.12$ µm. However, since the access guide is placed at the mid-point between the multimode sidewalls, selective excitation reduces by fourfold the apparent Talbot distance to 50.89 µm (see Figure 2.12 and text that refers to which).

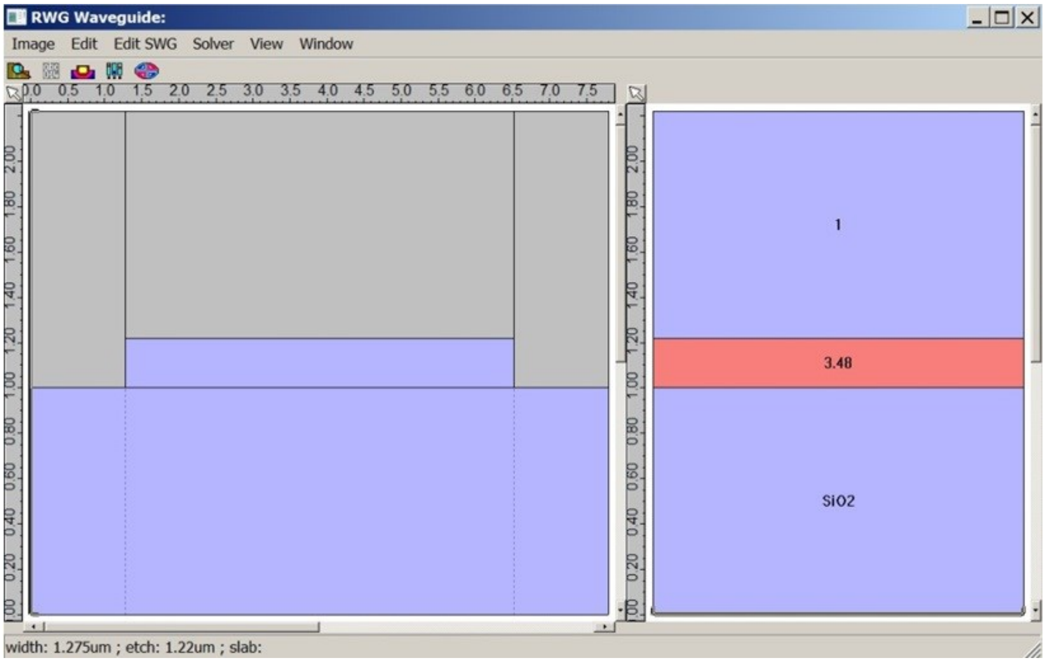

width: 1.275um ; etch: 1.22um ; slab:

Fig. 3.3. The cross section of the slab waveguide used for the MMI structure.

Theory predicts that a multimode waveguide length of 12.7 µm , that is one quarter of the apparent Talbot distance will provide the basis for a 1×4 MMI splitter. Figure 3.4 shows the simulation of the corresponding 1×4 MMI splitter. Although no attempt was made to perform an optimisation, the performance was judged best with 23% of the input power on each output port for a multimode waveguide length of 11.5 µm.

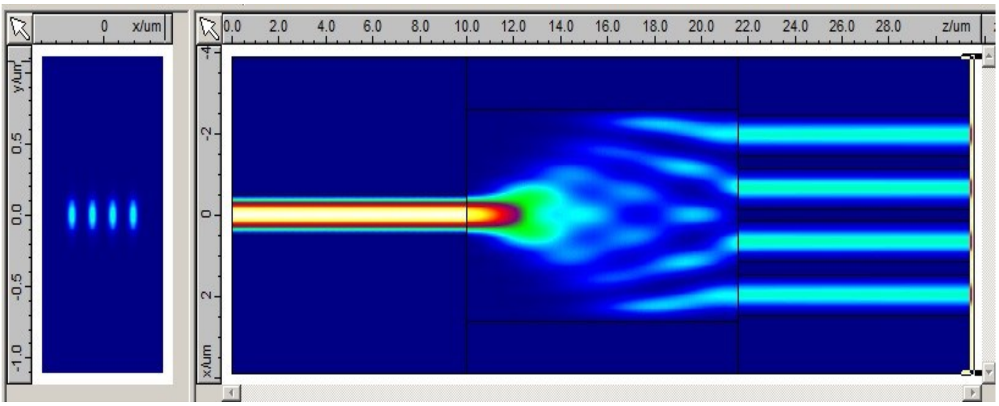

Fig. 3.4. A symmetric 1×4 MMI power splitter.

Figure 3.5 shows the fundamental mode of the multimode region and the fundamental modes of each of the four output ports.

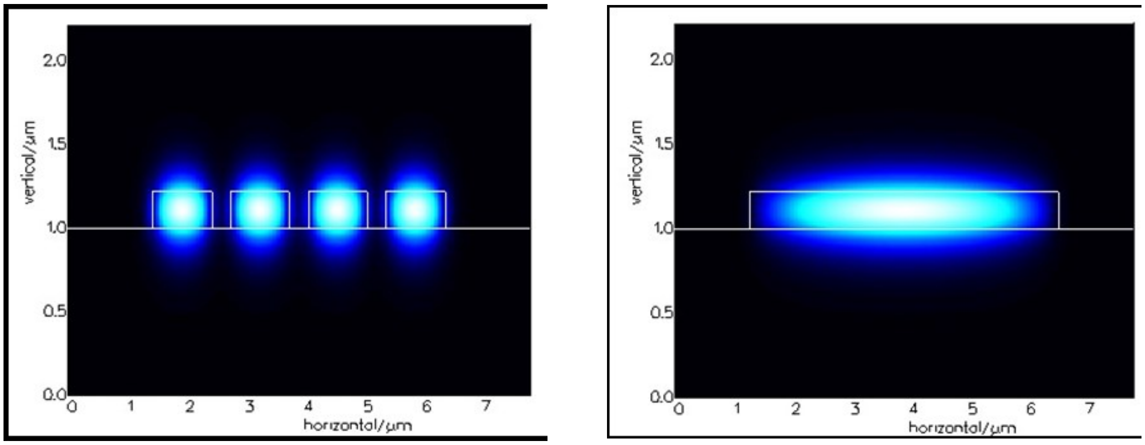

(a) (b)

Fig. 3.5. The fundamental mode profile in the multimode region (right) and the fundamental mode in each of the output ports (left) of the 1 × 4 MMI

The E_x field and the power split between the four outputs are shown in Figure 3.6, which confirms a uniform splitting ratio between the output ports and clean mode field profiles.

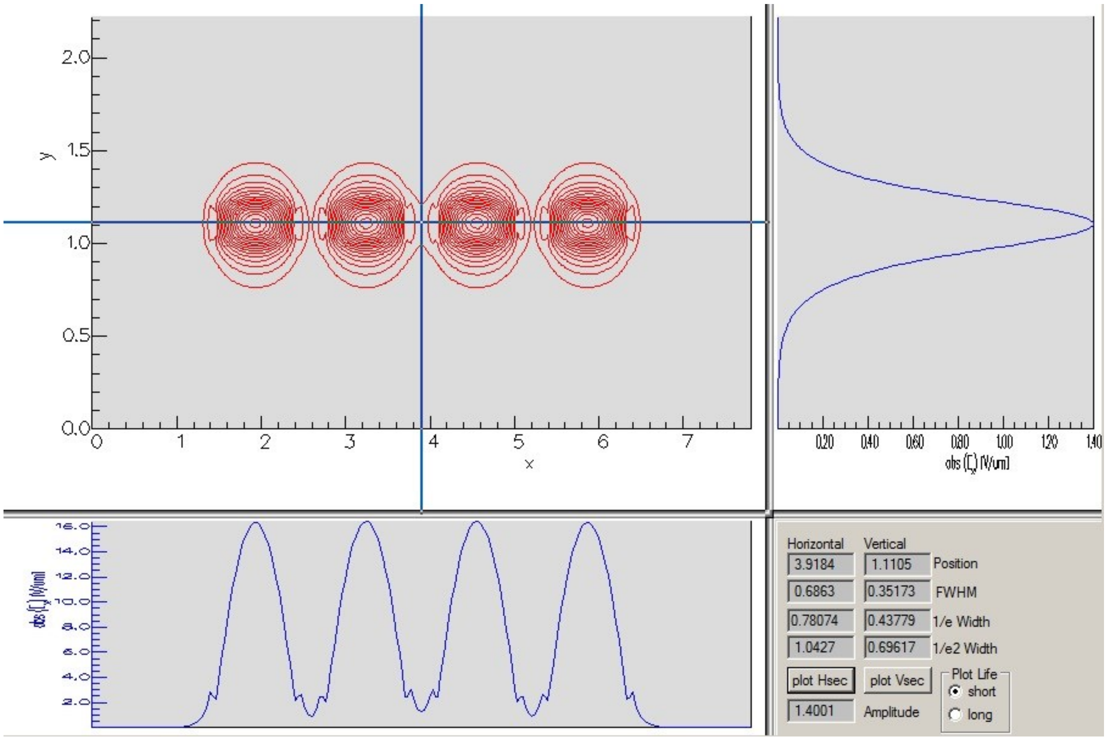

Horizontal	Vertical	
3.9184	1.1105	Position
0.6863	0.35173	FWHM
0.78074	0.43779	1/e Width
1.0427	0.69617	1/e2 Width

1.4001 Amplitude

Plot Life: ● short ○ long

Fig. 3.6. The E_x field profile on the four output ports of the 1 × 4 MMI with 23% splitting ratio on each port.

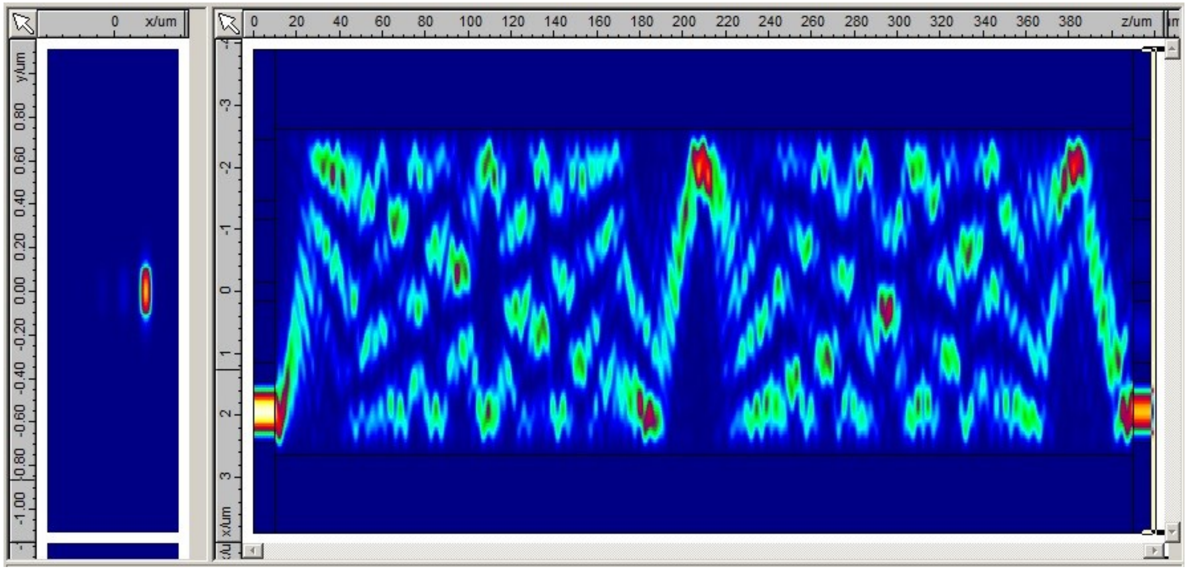

Fig. 3.7. A 4 × 4 MMI with a primary self-image at the distance of 400 μm compared to a prediction of 407.12 μm

For a 4 × 4 MMI, with the same width of 5.25 μm, the input and output access waveguides with width 1 μm are spaced 1.3 μm centre-to-centre. L_π is unchanged as 67.853 μm and the primary self-image is located at $2 \times Z_T = 407.12$ μm.

To use this structure as a splitter the output waveguides should be located at a distance of 50.89 μm. Figure 3.8 shows the result obtained corresponding to a distance of 51.8 μm.

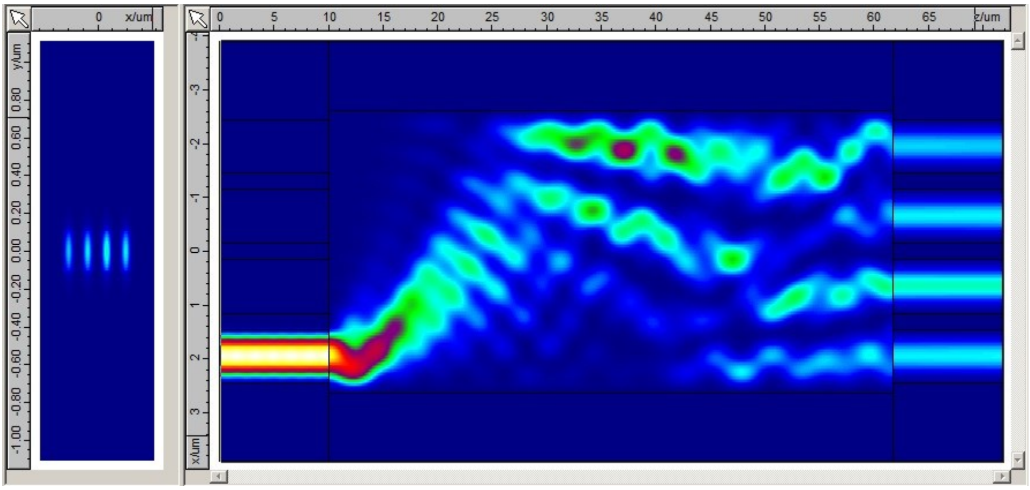

Fig. 3.8. A 4 × 4 MMI used as a 1 × 4 power splitter.

Figure 3.9 shows the fundamental mode on each of the four output ports.

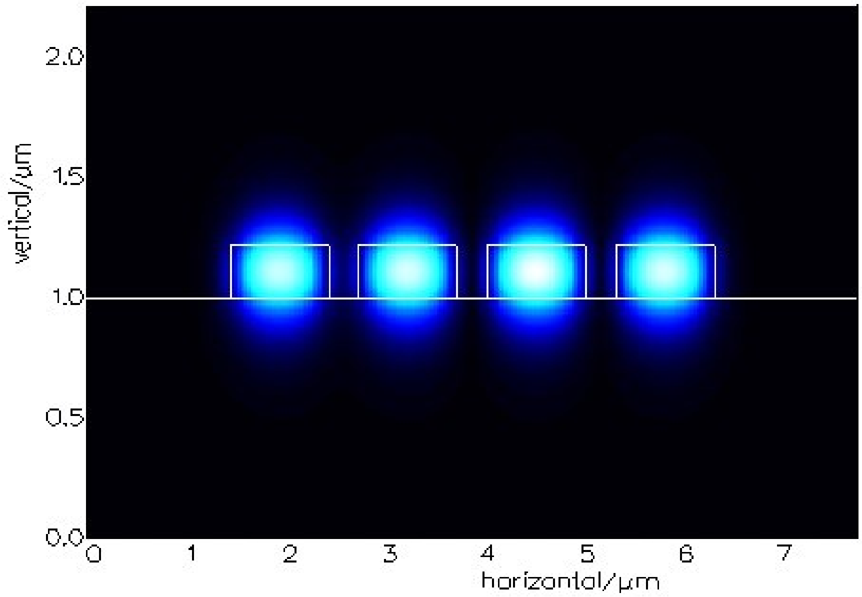

Fig. 3.9. The fundamental mode propagation on the output ports of the 4×4 MMI.

Figure 3.10 shows the E_x profile on the four outputs. A reasonably uniform splitting ratio of between 19% to 24% for the different outputs is obtained.

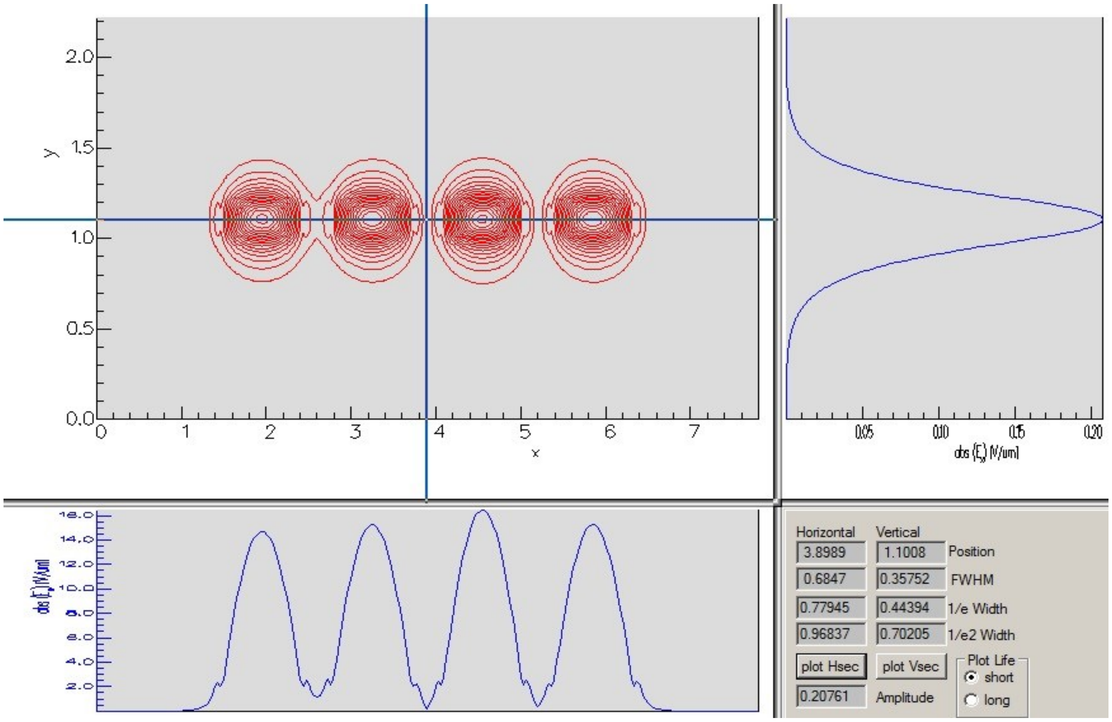

Horizontal	Vertical	
3.8989	1.1008	Position
0.6847	0.35752	FWHM
0.77945	0.44394	1/e Width
0.96837	0.70205	1/e2 Width
0.20761	Amplitude	

Fig. 3.10. The E_x field profile on the four output ports of a 4×4 MMI used as a 1×4 power splitter.

The phase $\varphi(\boldsymbol{T})$ of the elements of transfer matrix $\boldsymbol{T}$ that was obtained from the scattering matrix calculated by FimmWave for the 4×4 MMI was:

$$\varphi(\boldsymbol{T}) = \begin{bmatrix} 2.9947 & 0.4838 & -2.4247 & 2.9535 \\ 0.4817 & 3.0707 & 2.9655 & -2.4313 \\ -2.4313 & 2.9655 & 3.0707 & 0.4817 \\ 2.9535 & -2.4247 & 0.4838 & 2.9947 \end{bmatrix}$$

Equation 3.8

which should be compared to the theoretical prediction

$$\varphi(\boldsymbol{T}) = \begin{bmatrix} 0.0 & -0.75 & 0.25 & 0.0 \\ -0.75 & 0.0 & 0.0 & 0.25 \\ 0.25 & 0.0 & 0.0 & -0.75 \\ 0.0 & 0.25 & -0.75 & 0.0 \end{bmatrix} \pi$$

Equation 3.9

To make the comparison clearer an average is taken of the entries of the experimentally measured matrix that correspond to a unit entry in the theoretically predicted matrix. Since the overall phase is arbitrary, this average of 2.9961 is subtracted from each entry and the remainder expressed as a fraction of π modulo 2π

$$\varphi(\boldsymbol{T}) = \begin{bmatrix} -0.0005 & -0.7997 & 0.2745 & -0.0136 \\ -0.8004 & 0.0237 & -0.0097 & 0.2724 \\ 0.2724 & -0.0097 & 0.0237 & -0.8004 \\ -0.0136 & 0.2745 & -0.7997 & -0.0005 \end{bmatrix} \pi$$

Equation 3.10

The residual is:

$$\boldsymbol{\varepsilon} = \begin{bmatrix} -0.0005 & -0.0497 & 0.0245 & -0.0136 \\ -0.0504 & 0.0237 & -0.0097 & 0.0224 \\ 0.0224 & -0.0097 & 0.0237 & -0.0504 \\ -0.0136 & 0.0245 & -0.0497 & -0.0005 \end{bmatrix} \pi$$

Equation 3.11

Figure 3.11 illustrates the comparison of the phases found by simulation with those predicted by theory using the unit circle.

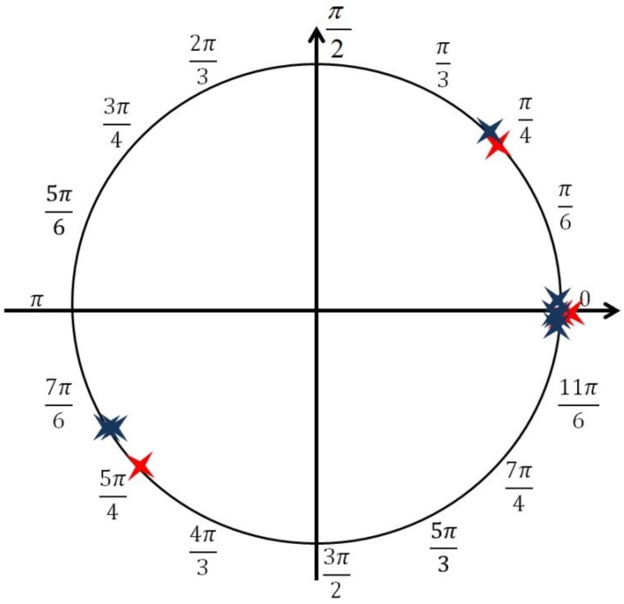

Fig. 3.11. The unit circle showing a comparison of the relative phases calculated from theory (red), and those found from the simulation (blue)

The agreement between simulation and theory is seen to be good. The *rms* deviation is 3% of π radians. It can be expected that use of the Kallistos (Photon Design) optimiser to adjust the design parameters towards improved performance (i.e. less non-uniformity and excess loss) will also improve the agreement of the relative port phases. Engineering of the dispersion relation of the modes in the multimode region to better fit the assumptions of the theory may also improve the accuracy of the phases. This can be achieved by sub-wavelength structuring of the MMI as described by Maese-Novo *et al* [58] and is redolent of the approach taken in this work to implement a planar Lüneburg lens as described in Chapter 4.

3.3 The optical switch fabric

3.3.1 The Transpose Interconnection

The previous section was concerned with a $1 \times N$ switch element with the Generalised Mach-Zehnder Interferometer (GMZI) architecture that makes use of optical phased array (OPA) principles to steer a light beam from a single input port to one of N output ports. As such, it provides the function of a route switch, i.e. light from an incoming port is routed to one of N outgoing ports. Fortunately, the same structure may be reversed to operate as a select switch, i.e. light from one of N incoming ports is selected and passed on to a single outgoing port. It is then possible to construct a switch fabric that combines N route switches of dimension $1 \times N$ with N select switches of dimension $N \times 1$ to form a $N \times N$ route & select switch. Further scaling of port dimension is then possible in principle by treating the $N \times N$ route & select switch as the switch elements in a larger switch fabric.

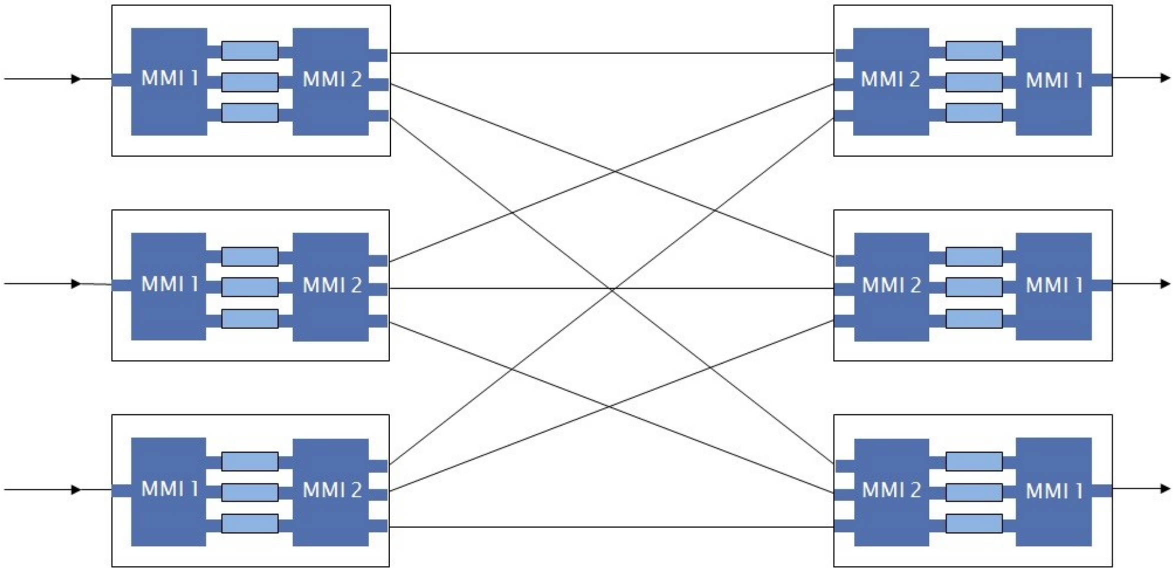

Fig.3.12. The route & select switch architecture, using optical phased array beam steering as switch elements

Figure 3.12 shows a 3×3 route & select switch architecture using 3 GMZI OPA 1×3 route switch elements in a first stage and 3 GMZI OPA 3×1 select switch elements in a second stage. Note the 9×9 interconnection network between the two stages. This network is often called a 'full mesh' interconnection but calling it a transpose interconnection is more descriptive of its function: if the ordered number (j, k) represents module j port k then the interconnection effects a transposition:

$$(j, k) \longrightarrow (k, j)$$

Equation 3.12

where in the first stage the port is an output port of a route switch element and in the second stage the port is an input port of a select switch element.

The transpose interconnection is a ubiquitous structure within switch fabrics. Restricted to a plane, it features a very large number of crossovers which seriously hampers electrical and optical waveguide implementations. Crossovers are natural in free-space optical systems and present no particular problems; the challenge for free-space optical systems is the stringent alignment requirements.

3.3.2 Fourier Optical Transpose Interconnection

A free-space Optical Transpose Interconnection System (OTIS) was introduced first by Marsden *et. al* [59]. Two micro-lens arrays formed a collection of off-axis telescopes which imaged input ports onto their associated output ports. The use of decentred optics causes severe aberrations [60-61], which are a source of insertion loss and crosstalk if the system is used to image between mono-mode waveguides.

An alternative architecture [32, 33, 62] draws its inspiration from the observation that a Fourier transform lens effects a transposition by interchanging the position (intercept) and momentum (angle) co-ordinates of a ray, as is illustrated in Figure 3.13. As a consequence, an optical transpose in space can be performed by a system consisting of a first and third stage array of Fourier transform microlenses on either side of a second stage Fourier transform macrolens in a confocal arrangement as shown in Fig. 3.14. The input ports (sources) are located in the focal plane of the first stage microlenses and the output ports (sinks) are located in the rear focal plane of the third stage microlenses.

From a first perspective, spatially displaced rays parallel to the optical axis entering a first stage microlens are angularly multiplexed in its rear focal point. Conversely, angularly multiplexed rays passing through the front focal point of a third stage microlens are angularly de-multiplexed into spatially displaced rays parallel to the optical axis. The second stage macrolens performs the actual transposition by interchanging ray position and ray momentum (angle) co-ordinates of a ray between its front and rear focal planes.

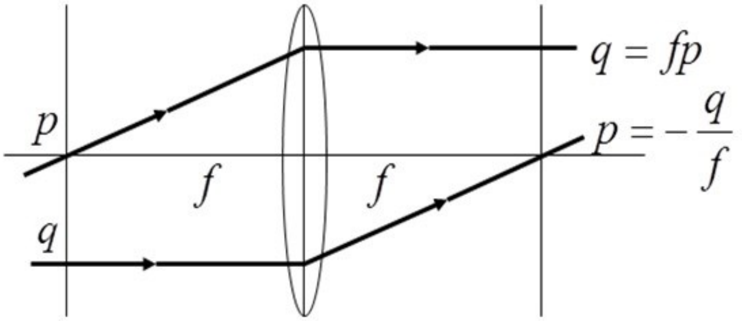

Fig. 3.13. The interchange of the position q and angle p co-ordinates of a ray between the front and rear focal planes of a Fourier transform lens with a focal length of f

From a second perspective, each microlens in the first stage together with the central macrolens acts as an off-axis telescope that forms a magnified image of its respective input port group. The magnified images from each telescope are overlaid but angularly multiplexed in the rear focal plane of the central lens. Conversely, each microlenses in the third stage with the central lens acts an off-axis telescope which forms a magnified image its respective output port group. The magnified images from each telescope are overlaid but angularly multiplexed in the front focal plane of the central lens.

A non-intuitive property of the Fourier Optical Transpose Interconnection System (FOTIS) is that the mapping between an input port field distribution and its associated output field distribution is a Fourier transform rather than the imaging relation of the orthodox OTIS system. Indeed, concave lenses may be used in the first and third stages to reduce the system length. If it is desired to connect identical monomode ports then the modal field must closely approximate an eigenfunction of the Fourier transform. Fortunately, the modal field of monomode waveguides is in general close to a Gaussian and a Gaussian with an appropriate width and given vacuum wavelength can be found that is invariant to the action of a Fourier transform lens of given focal length.

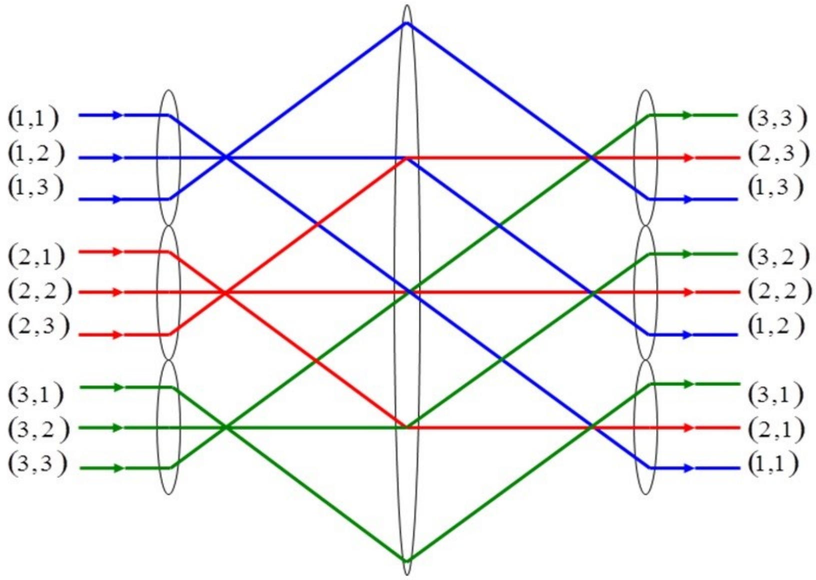

Fig. 3.14. A three stage optical transpose interconnection system. The rays at the input are labeled first by input group and then by input port within the input group. The rays at the output retain the label assigned at the input which may be reinterpreted as a label first by output port within an output group and then by output group. The rays are colour coded by input group to ease tracking their path across the system and to clearly illustrate their transposition.

Rays close to the chief rays sketched in Fig. 3.14 experience a transformation corresponding to a Fourier transform lens of effective focal length given by:

$$f = \frac{f_1 f_3}{f_2}$$

Equation 3.13

where f_1 , f_2 and f_3 are the focal lengths of the lenses in the first, second and the third stages respectively.

The corresponding radius w_0 of the beam waist of a Gaussian beam invariant to this transformation is:

$$w_0^2 = \frac{1}{\pi}\frac{\lambda_0}{n} f$$

Equation 3.14

where λ_0 and n are the wavelength in vacuum and refractive index of the ambient media respectively (here assumed identical at input and output).

The optical architecture is capable of implementing a $(L \times M) \leftrightarrow (M \times L)$ transposition with the inputs and outputs arranged on any convenient two dimensional lattice (the regular hexagonal lattice is advantageous from a packing perspective). For simplicity here the symmetric case $(N^2 \times N^2) \leftrightarrow (N^2 \times N^2)$ with ports and port groups arranged on a regular square lattice (i.e. as an $(N \times N)$ array of $(N \times N)$ arrays) only will be considered.

Let δ denote the pitch of the input / output ports within a microlens group; Δ denote the pitch of the first/third stage microlenses; and D denote the diameter of the aperture of the second stage lens; and introducing design margins $\eta_\Delta, \eta_D, \eta_\delta$ which are factors of the order of unity.

For circular lens apertures:

$$\Delta = \eta_\Delta N\delta \quad \eta_\Delta > \sqrt{2}$$

Equation 3.15

$$D = \eta_D N\Delta \quad \eta_D > \sqrt{2}$$

Equation 3.16

Furthermore to avoid beam overlap:

$$\delta = \eta_\delta 2w_0 \quad \eta_\delta > \sim 3$$

Equation 3.17

From the previous description of the imaging relations:

$$\frac{f_2}{f_1} = \frac{f_2}{f_3} = \frac{\Delta}{\delta} = \eta_\Delta N$$

Equation 3.18

which implies:

$$\begin{gathered} f_1 = f_3 = \eta_\Delta N f \\ f_2 = \eta_\Delta^2 N^2 f \end{gathered}$$

Equation 3.19

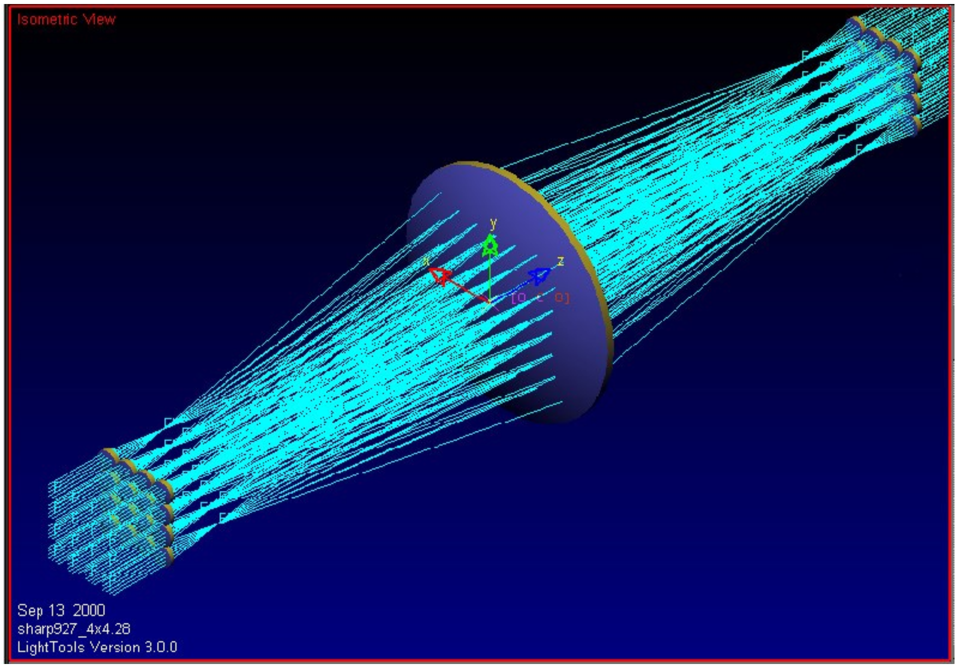

Fig 3.15. A ray trace of a $(4^2 \times 4^2) \leftrightarrow (4^2 \times 4^2)$ free space optical transpose interconnection system. There are a total of 256 beams passing through this optical system.

For example, the design parameters for the optical transpose shown in Figure 3.15 might be chosen to be:

$$\lambda_0 = 1.55\ \mu m$$
$$n = 1$$
$$w_0 = 3\mu m$$
$$\Longrightarrow$$
$$f = 18.24\ \mu m$$
$$N = 4$$
$$\eta_\Delta = 1.6$$
$$\Longrightarrow$$
$$f_1 = f_3 = 116.74\ \mu m$$
$$f_2 = 747.11\ \mu m$$

This conservative[4] design illustrates how compact in principle a FOTIS can be.

3.4 The Planar Lüneburg Lens Optical Transpose Interconnection

3.4.1 Lüneburg Lens

As originally conceived, the FOTIS employed rotationally symmetric Fourier transform lenses. It may suffice to implement the first and third stage lenses as thin or gradient index microlenses as their small size limits their aberrations but, most likely, a well-corrected

---

[4] The use of a hexagonal lattice would permit a reduction of the parameter η_Δ.

compound lens is required in the second stage to control distortion. Implementations are also possible using spherical mirrors [33].

It is known [63] that a reversible lens capable of stigmatic imaging in its rear focal plane of an object at infinity is a perfect Fourier transform lens, although asymmetric designs are known [64] with fewer surfaces than a reversible design. In an original contribution the conventional lenses of FOTIS, which have cylindrical symmetry about their axis, is replaced by graded index lenses which are spherically symmetric about a central point. A number of lenses within this class are known to be capable of perfect geometrical optical imaging such as the Maxwell fish-eye, Eaton, Miñano and Lüneburg lenses [65]

The Lüneburg lens was first introduced by Rudolf Karl Lüneburg in 1944 [66]. The graded refractive index of a Lüneburg lens is described by:

$$\begin{aligned} n(r) &= n_0\sqrt{2-(r/a)^2} && r \leq a \\ &= n_0 && r > a \end{aligned}$$

Equation 3.20

where a is the outer radius of the lens, r is the distance from the centre of the lens, and n_0 is the ambient refractive index.

In Appendix III, Hamilton's method is applied to the ray analysis of the Lüneburg lens with the result shown in Figure 3.16. No paraxial approximation is involved in the derivations. Rays entering the lens where the surface of the lens intersects the optical axis, $\boldsymbol{q} = (-a, 0)^T$ and incident at an angle θ to the normal to the lens $\boldsymbol{p} = n_0(cos(\theta), -sin(\theta))^T$, are found to exit the lens parallel to the optical axis at the point $\boldsymbol{q}= a(cos(\theta), -sin(\theta))^T$. The optical path length from the impact point to the plane tangent to the rim of the lens and normal to the optical axis is found to be a constant independent of $\boldsymbol{p}$. All other possible ray trajectories follow by rotation around the centre due to the spherical symmetry of the lens.

Hence:

$$\begin{bmatrix} \boldsymbol{q_2} \\ \boldsymbol{p_2} \end{bmatrix} = \begin{bmatrix} 0 & a \\ -\frac{1}{a} & 0 \end{bmatrix} \begin{bmatrix} \boldsymbol{q_1} \\ \boldsymbol{p_1} \end{bmatrix}$$

Equation 3.21

where $(\mathbf{q_1}, \mathbf{p_1})^\mathbf{T}$ and $(\mathbf{q_2}, \mathbf{p_2})^\mathbf{T}$ characterise the incoming and outgoing rays respectively; $\mathbf{q_1}, \mathbf{p_1}, \mathbf{q_2}, \mathbf{p_2}$ are vectors all lying in the same plane passing through the centre of symmetry.

The matrix in Equation 3.21 is identical to the ray transformation between the focal planes of a thin lens of focal length $f = a$. A Lünburg lens brings an incident plane wave to a focus on the lens surface at a point where the surface is intersected by an axis parallel to the incident wavevector that passes through the centre of symmetry. However, Equation 3.21 is not the equation of linear matrix optics because $\mathbf{q_1}, \mathbf{q_2}$ and $\mathbf{p_1}$, $\mathbf{p_2}$ are not coordinate functions of points on plane surfaces but rather co-ordinate functions of points on spherical surfaces:

$$\begin{gathered} \|\boldsymbol{q_1}\| = \|\boldsymbol{q_2}\| = a \\ \|\boldsymbol{p_1}\| = \|\boldsymbol{p_2}\| = n_0 \end{gathered}$$

Equation 3.22

That is the tips of $\mathbf{q_1}, \mathbf{q_2}$ are restricted to lie on the surface of a sphere of radius a (the surface of the lens) and the tips of $\mathbf{p_1}$, $\mathbf{p_2}$ are restricted to lie on the surface of a sphere of radius n_0.

The linear part of the response to small changes about a chief ray is however described by:

$$\begin{bmatrix} \boldsymbol{\delta q_2} \\ \boldsymbol{\delta p_2} \end{bmatrix} = \begin{bmatrix} 0 & f \\ -\frac{1}{f} & 0 \end{bmatrix} \begin{bmatrix} \boldsymbol{\delta q_1} \\ \boldsymbol{\delta p_1} \end{bmatrix}$$

Equation 3.23

where $\boldsymbol{\delta q_1}$, $\boldsymbol{\delta q_2}$ are vectors in the tangent planes to the surface of the lens at the impact and escape points of the chief ray; and $\boldsymbol{\delta p_1}$, $\boldsymbol{\delta p_2}$ are vectors in the co-tangent planes (Fourier conjugate planes) at the impact and escape points of the chief ray. This relation shows that in the linear optics approximation, the Lüneburg lens maps rays between its entrance and exit tangent planes like a thin lens of focal length, f, maps rays between its focal planes forming the Fourier transform of the incident field in its rear focal plane.

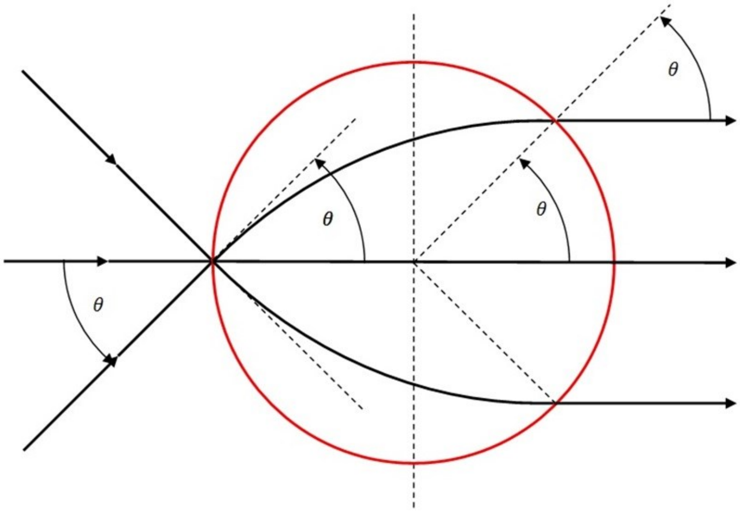

Fig. 3.16. Ray trajectories through a Lüneburg lens. It follows from the spherical or cylindrical symmetry that all other ray paths may be found by rotation about the origin.

The curvature of the field and the fact that the impact & escape ray intercepts and the centre of symmetry are not necessarily co-linear is accommodated by placing micro-Lüneburg lenses around and in osculation with the macro-Lüneburg lens. Figure 3.17 shows a planar section through a $(3^2 \times 3^2) \leftrightarrow (3^2 \times 3^2)$ Lüneburg Optical Transpose Interconnection System (LOTIS) and also illustrates some example ray trajectories which, while unfamiliar, confirm operation as a transpose interconnection. The 3D structure of LOTIS (i.e. a sphere coated by smaller spheres) would resemble a raspberry.

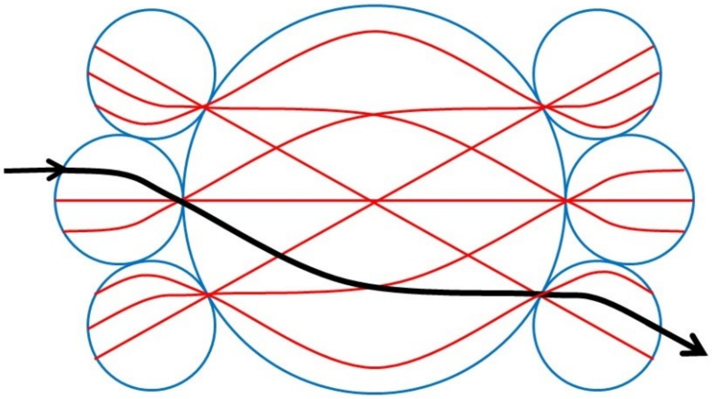

Fig. 3.17. A planar section through a $(3^2 \times 3^2) \leftrightarrow (3^2 \times 3^2)$ optical transpose interconnection system using Lüneburg lense showing the trajectories of the chief rays between input and output ports. The same diagram also suffices to illustrate a $(3 \times 3) \leftrightarrow (3 \times 3)$ optical transpose interconnection system employing cylindrical Lüneburg lenses.

A 3D optical system presents formidable packaging and alignment issues. Moreover, while a 3D Lüneburg lens can be fabricated for use at microwave frequencies [67], a means of fabricating a 3D Lüneburg lens for use at optical frequencies is not yet available. It is straightforward to eliminate one transverse dimension to yield a system that employs cylindrical optics. The penalty is a reduction of port dimension: the dimension of the example given in Section 3.4 would reduce to $(4 \times 4) \leftrightarrow (4 \times 4)$ with a total of 16 beams passing through this optical system. However, this reduction of port dimension may be partially compensated by the possibility of sub-wavelength confinement of the light possible in silicon photonic wire waveguides and the precision alignment offered by the lithographic processes used in micro-fabrication.

3.4.2 Waveguide Confinement Correction of the Lüneburg Refractive Index Profile

Optical systems that are spherically symmetric about a point or rotationally symmetric about an axis are described completely in terms of the ray paths restricted to a plane that includes the centre of symmetry or the optical axis respectively. If a cylindrical lens has the refractive index profile that was defined in Equation 3.20, the same theory will apply to rays restricted to a plane normal to the axis of the cylindrical lens. The light may be confined close to the normal to the cylinder by placing a thin slice of the cylinder between an upper and lower cladding as illustrated schematically in Figure 3.18. Although the light is bound to the core material an evanescent field extends on either side of the core material into the lower index cladding material. Assuming the refractive index of the cylinder varies slowly on the scale of the wavelength, the local propagation constant in the plane of the slab corresponds to the effective index seen by the fundamental mode in a slab with a core with refractive index equal to the local value of the graded index. To obtain the desired behaviour it is necessary to ensure that the graded index is such that after correction for confinement the resultant effective index varies as desired i.e. for a planar waveguide Lüneburg lens it is the local effective index of the fundamental slab mode that must vary according to Equation 3.20.

In Appendix IV, the analytic wave theory of the modes of an asymmetric slab waveguide is elaborated. A transcendental equation is found for the effective index of the modes in terms of the vacuum wavelength and the waveguide parameters: slab thickness and refractive indices of core, upper cladding and lower cladding. With the aid of a numerical root finder, one may solve for the effective index versus the core index which enables the waveguide confinement correction to the core refractive index to be calculated given a desired effective index, as provided by Equation 3.20. An example is given in Figure 3.19.

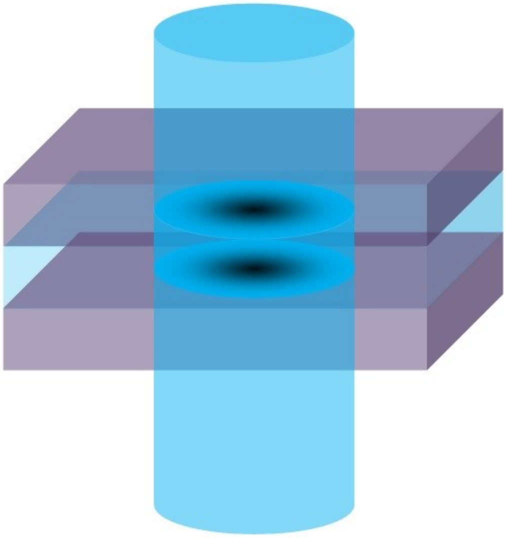

Fig. 3.18. A schematic diagram illustrating a slice of a cylindrical graded index lens used as the core material of a slab waveguide to restrict the rays essentially to a plane normal to the axis of the cylinder. The light is confined in the direction normal to the slab as the local fundamental transverse mode of a graded index slab waveguide. The refractive index profile of the cylinder must be corrected for the effect of confinement in the slab as explained in the text.

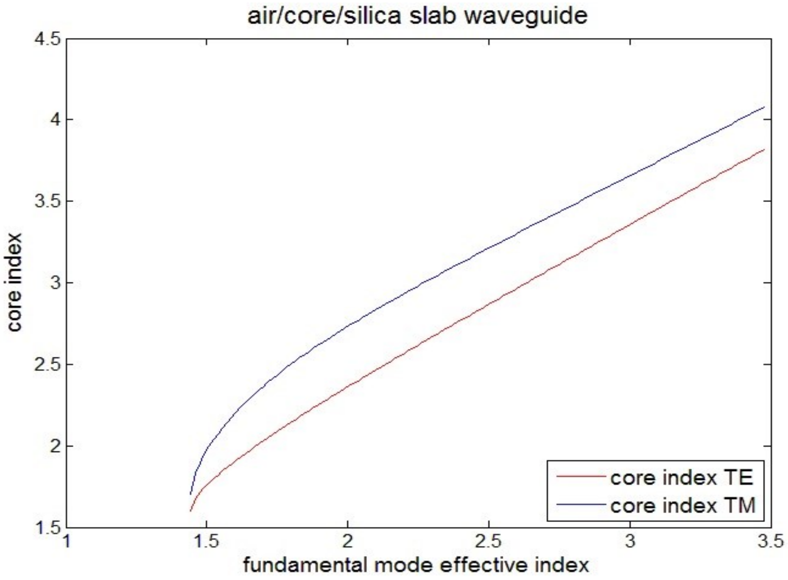

Fig. 3.19. A plot illustrating the dependence of the effective index of the TE or TM fundamental mode and the refractive index of a 350 nm core on a silica substrate (refractive index 1.44402) in air (refractive index 1.0) at a vacuum wavelength of 1550 nm. To correct for waveguide confinement the mode effective index must be equated to a desired refractive index (for a Lüneburg lens given by Equation 3.20) and the corresponding required value of the core index read-off from the plot.

3.4.3 Design Procedure

A symmetric design is considered and hence $f_1 = f_3$.

The principal layout issue is fitting the access waveguides around the rim of the micro-Lüneburg lenses to ensure that they are separated sufficiently and are sufficiently within the aperture of the lens for their emission to be properly captured. This layout difficulty is exacerbated by the requirement that the access waveguides of an individual micro-Lüneburg lens are parallel while most often inclined to the normal of their plane of incidence. To accommodate this layout constraint, a parameter $\eta \geq 1$ is defined that essentially preserves all relative features of a particular design but allows the overall expansion of the lens system relative to the waveguides:

$$f_1 = f_3 = \eta N f$$

$$f_2 = \eta^2 N^2 f$$

Equation 3.24

These equations have been chosen to ensure the magnification of the telescopes scales in proportion to and exceeds N as required

$$\frac{f_2}{f_1} = \frac{f_2}{f_3} = \eta N$$

Equation 3.25

while keeping the effective focal length of the Fourier transform lens seen by light following a chief ray:

$$f = \frac{f_1 f_3}{f_2}$$

Equation 3.26

The micro-Lüneburg have attached input and output waveguides which must have a mode half-width w_0 at $1/e$ field amplitude that satisfies:

$$w_0^2 = \frac{1}{\pi}\frac{\lambda_0}{n_0} f$$

Equation 3.27

which determines f.

It is then only necessary to check that the micro-Lüneburg lenses fit around the macro-Lüneburg lens. The angle θ subtended by the micro-Lüneburg lenses at the centre of the macro- Lüneburg is given by.

$$sin(\theta/2) = \frac{f_3}{(f_2 + f_3)}$$

Equation 3.28

To be feasible:

$$N\theta < \pi$$

Equation 3.29

For example, for a $(4 \times 4) \times (4 \times 4)$ LOTIS one may choose the following parameters:

$$
\begin{aligned}
&\lambda_0 = 1.55\ \mu\text{m}\\
&n = 2\\
&w_0 = 0.78\mu\text{m}\\
&\Longrightarrow\\
&f = 2.466\ \mu\text{m}
\end{aligned}
$$

$$
\begin{aligned}
&N = 4\\
&\eta = 1.1374\\
&\Longrightarrow\\
&f_1 = f_3 = \ 11.22\ \mu\text{m}\\
&f_2 = 51.05\ \ \mu\text{m}\\
&\Longrightarrow\\
&\theta = 20.76°\\
&N\theta = 83.04°
\end{aligned}
$$

3.4.4 2D FDTD Simulation of LOTIS

The parameters above were used to design a $(4 \times 4) \times (4 \times 4)$ LOTIS with 4 input and 4 output micro-Lüneburg lenses with diameter of $22.44\ \mu\text{m}$ surrounding a central macro-Lüneburg with a diameter of $102.10\ \mu\text{m}$. Each micro-lens is fed by four ridge waveguides with a width of 1.575 µm. The layout is shown in Figure 3.20.

In this design, the effective refractive index is changing from 2 on the rim of the Lüneburg lens to 2.828 in the centre of the Lüneburg in accordance with Equation 3.20. The access waveguide core width was adjusted to match the effective refractive index seen by its fundamental mode to the refractive index on the lens rims to minimise reflections at the interface. Correct operation of the design was verified by simulation using the 2D Finite Difference Time Domain (2D-FDTD) method which is a grid-based differential time-domain numerical modeling method introduced by Yee [68] and now regularly used to simulate nanophotonic devices.

Figure 3.21 shows a sequence of frames from a recording of the progress of the simulation. The frames track a light pulse from when it first exits access waveguide 2 of microlens 3 (counted from the bottom up) in the first stage (on the left); to when it enters access waveguide 3 of the microlens 2 (counted from the top down) in the third stage (on the right) after passing through the central lens, as predicted. Figure 3.22 shows the mode profiles of the pulse in the input access waveguide on entrance and in the output access waveguide on exit. The insertion loss was measured as -0.25 dB and the worst case crosstalk as -24.12 dB.

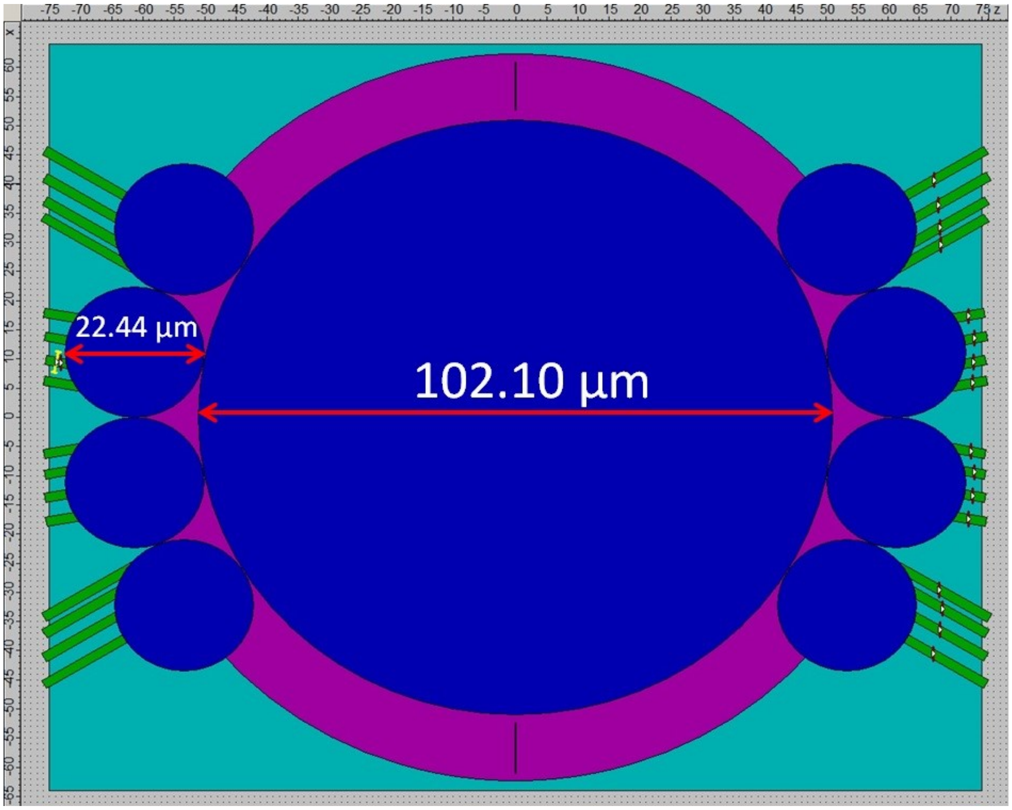

Fig. 3.20. The layout of a $(4 \times 4) \times (4 \times 4)$ planar three stage optical transpose interconnection system using Lüneburg lenses for simulation using 2D FDTD.

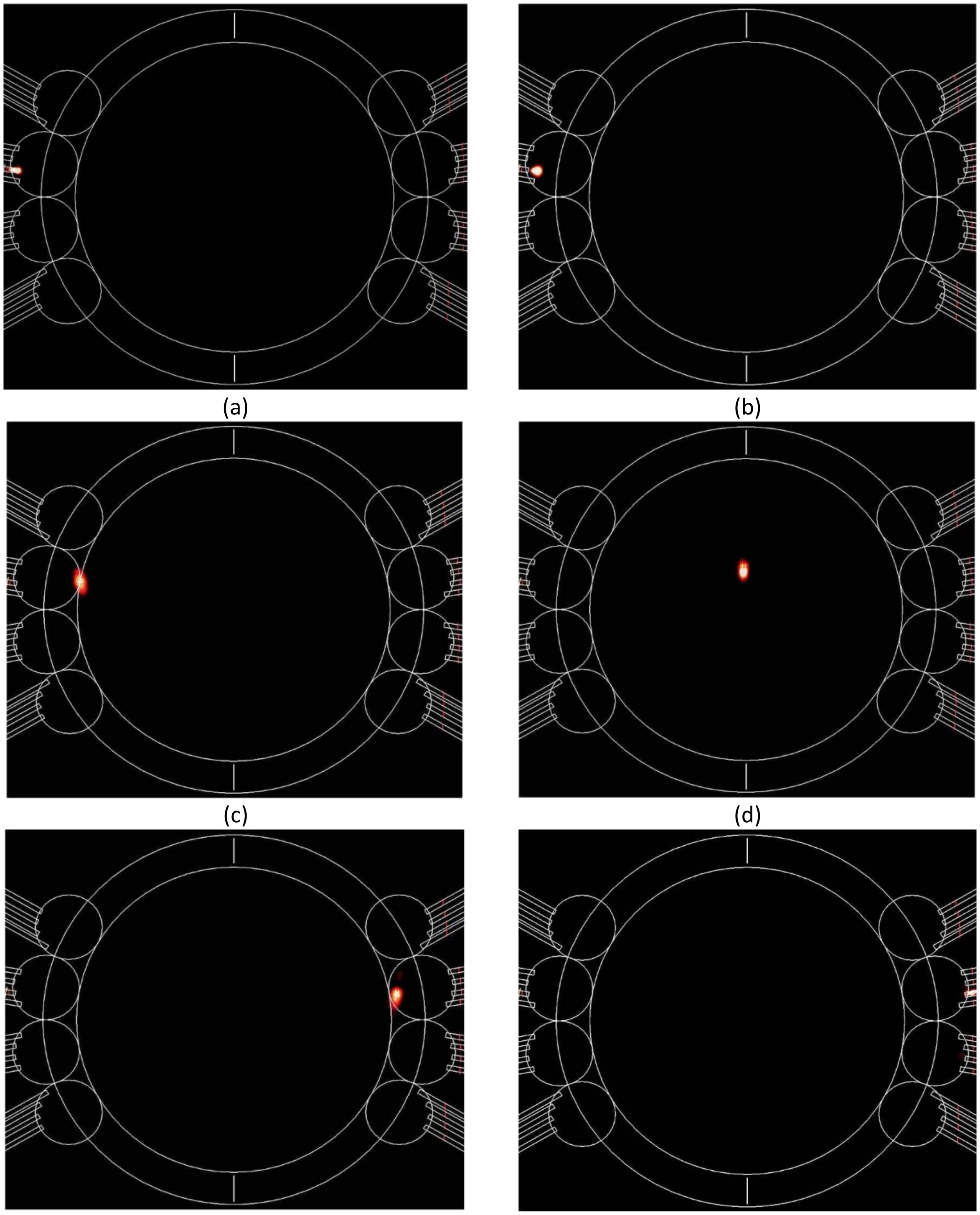
(a) (b) (c) (d) (e) (f)

Fig. 3.21. A sequence of frames of a 2D FDTD simulation of a light pulse propagating from an entrance waveguide, traversing through the Lüneburg lens system, and then leaving by an exit waveguide.

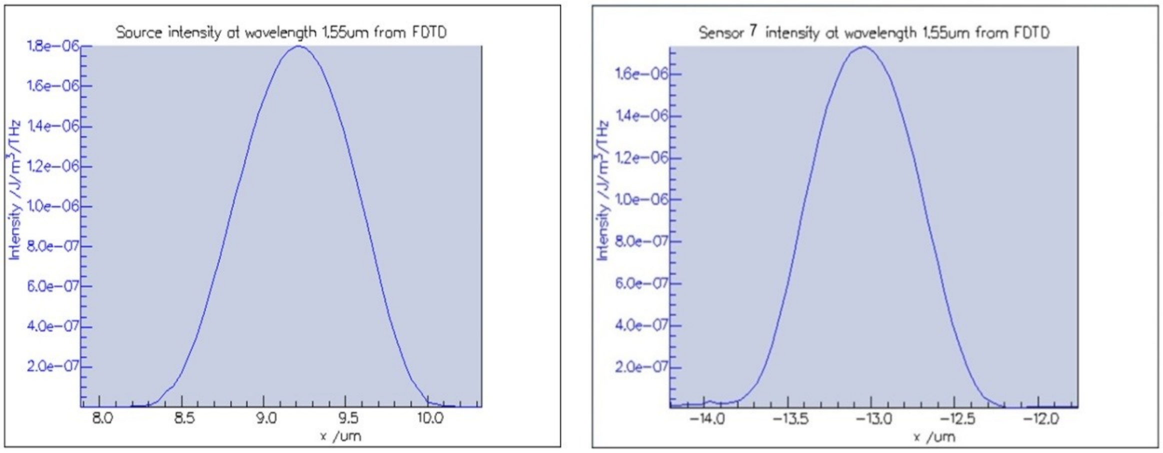

Fig. 3.22. The intensity of the wave on the input waveguide (left), and output waveguide (right). The insertion loss was measured as -0.25 dB.

This system is scalable to increase the number of input and output ports, hence it creates the potential to increase the number of ports in the switch fabric without the concern of large numbers of crossover waveguides for the interconnection of input and output stages.

3.5 Summary & Discussion

This chapter has considered the component parts of an $N \times N$ route & select switch constructed from generalised Mach-Zehnder interferometer switch elements combined using a planar optical transpose system. Procedures were outlined for the design of both the switch elements and the switch fabric. Special emphasis was placed on the phase relations between the ports of the MMI couplers that, together with electro-optic phase shift elements, are at the heart of the switch elements. The determination of the phase shifts necessary to steer a beam into a specified port were elaborated. An original planar Lüneburg Optical Transpose Interconnection system was introduced; its design, including waveguide confinement correction elaborated; and the feasibility of a $(4 \times 4) \times (4 \times 4)$ design demonstrated by 2D FDTD simulation. It was found that laying-out the access guides appropriately presented a significant challenge to scaling the LOTIS to higher port counts. It is noted here that the access guides form the connections between an MMI of the switch element and the micro-Lüneburg lens. One option to investigate is therefore whether the access guides may be eliminated by merging the MMI and the micro-Lüneburg lens. It is possible that a line-tapered MMI design [69] could more closely pack beams with smaller spot sizes at the effective entry of the micro-Lüneburg lens.

The question of how the planar Lüneburg lens may be fabricated has been left open in this chapter. In the next chapter, a very promising graded metamaterial approach to the realisation of the Lüneburg lenses is studied.

Chapter 4. Planar Metamaterial Lüneburg Lens

4.1 Introduction

In Chapter 4 the Lüneburg Optical Transpose Interconnection System (LOTIS) was described and the insertion loss and cross-talk were evaluated by a 2D FDTD simulation. The insertion loss was found to be low, which augurs well for implementation in a planar integration technology although how the Lüneburg lenses might be implemented in planar form was left as an open question.

The utility of planar waveguide lenses goes beyond the specific application of interest in this thesis. Optical information processing systems have traditionally been demonstrated using 3D free-space optical systems employing bulk optical components. These systems are bulky and unstable due to the stringent alignment tolerances that must be met. Taking advantage of the alignment accuracy offered by a photonic integrated circuit, these issues may be overcome by confining the light in a planar slab waveguide. The limitation on scaling, consequent on the loss of one dimension is offset by the nanoscale component footprints attainable in a silicon integration platform. A key component of this free-space-optics-on-a-chip concept is a waveguide lens, which may be used to implement, *inter alia*, the complex crossover interconnections of a switch fabric; the application of interest here.

Initially consider a planar slab waveguide structure with a solid core (for example a silicon core with an air upper cladding and silica substrate). The structure confines the light in the direction normal to the plane as a 1D asymmetric slab waveguide. For simplicity, assume the slab only supports the fundamental mode of this 1D waveguide. The wavevector of this mode can point in any direction within the plane. Hence the slab acts as a region of '2D free-space'. The effective index the mode experiences is not the refractive index of the core but somewhere between the refractive index of the core and the lower cladding because of the waveguide confinement. The effective index depends upon the slab waveguide parameters: the vacuum wavelength; the thickness of the core; and the refractive indices of core, upper cladding and lower cladding. For example, variations in the thickness of the core can be used to change the effective refractive index seen by the mode. If the thickness is varied spatially but sufficiently gradually (on the scale of the wavelength) the mode will adapt to the change adiabatically and the net effect will be that the mode experiences a 'graded' effective index.

Fourier transform lenses were fashioned by these means in the $LiNbO_3$ material integration platform in the context of integrated optics acousto-optic RF-spectrum analysers [70]. In most applications, the precision to which the effective refractive index must be defined places stringent tolerances on the accuracy of the fabrication process. High precision multiple-step or continuous level etching presents a formidable fabrication challenge; ensuring that any solution involves complicated processes that are time consuming and costly.

Advances in lithography, however, now enable sub-wavelength scale nanostructuring of a material in a single etch step while still offering continuous control over the dimensions of the features of the nanostructure. Essentially, the patterning creates a binary composite material consisting of inclusions of one material within a host of a different material. Traditionally, the term 'artificial dielectric' was used to describe these nanostructured materials. The term 'metamaterial' is now in more common parlance. Now, instead of varying the thickness of the core, suppose the core is such a binary composite, the refractive index of the composite may be varied between that of the host (say silicon) and that of the inclusion (say air) by adjusting its composition. It remains the case that the effective index seen by the mode is not the same as the refractive index of the bulk composite material. To obtain good designs, the desired effective index of the mode must be corrected for the vertical waveguide confinement to obtain the desired local 'effective medium' index of the composite.

E-beam lithography offers the patterning of deep subwavelength structures: the propagating wave then experiences a homogenous material with an effective refractive index that may be predicted using simple mixture formulae [71]. In the long-wavelength limit, the distribution of inclusions within the host may be random; only the local expected filling fraction is of significance.

Deep UV optical lithography is currently just capable of patterning photonic crystal structures which operate in the resonance regime where the lattice constant is close to half a wavelength. When the mean spacing of inclusions is only just sub-wavelength, a random distribution of inclusions will badly scatter light. It is then preferable to use a (locally) perfectly periodic distribution (i.e. a photonic crystal structure), which, in principle, supports lossless Floquet-Bloch modes with a dispersion relation that defines the photonic band structure.

As illustrated in Fig. 4.1, the period must remain sufficiently sub-wavelength to avoid photonic crystal band-gap effects (resonance phenomena caused by Bragg scattering) which cause curvature of the band. If the band is curved, there is no simple mixture formula for the effective index and the design effort is considerably more involved.

The design effort required is exacerbated by the necessity of proximity correction of the process for feature sizes less than 400 nm. The optical proximity effects involve interference and are too complex to model by other than empirical methods. Nevertheless, holes as small as 130 nm on a 250 nm pitch may be fabricated using, for example, the IMEC 193 nm process [72]. Photonic crystal waveguide losses of 4 dB/cm have been reported [73] and are accounted for largely by fabrication errors. In contrast, sub-wavelength grating waveguides that have feature sizes within the reach of 193 nm UV lithography are reported [74] to have losses of ~2.5 dB/cm. Photonic crystal waveguides operate at wavelength near the band-edge and are very sensitive to placement errors whereas subwavelength grating waveguides operate in the long-wavelength limit and are insensitive to placement errors. It can therefore be expected that much lower losses will be found in the long-wavelength region of operation of a nanostructured material.

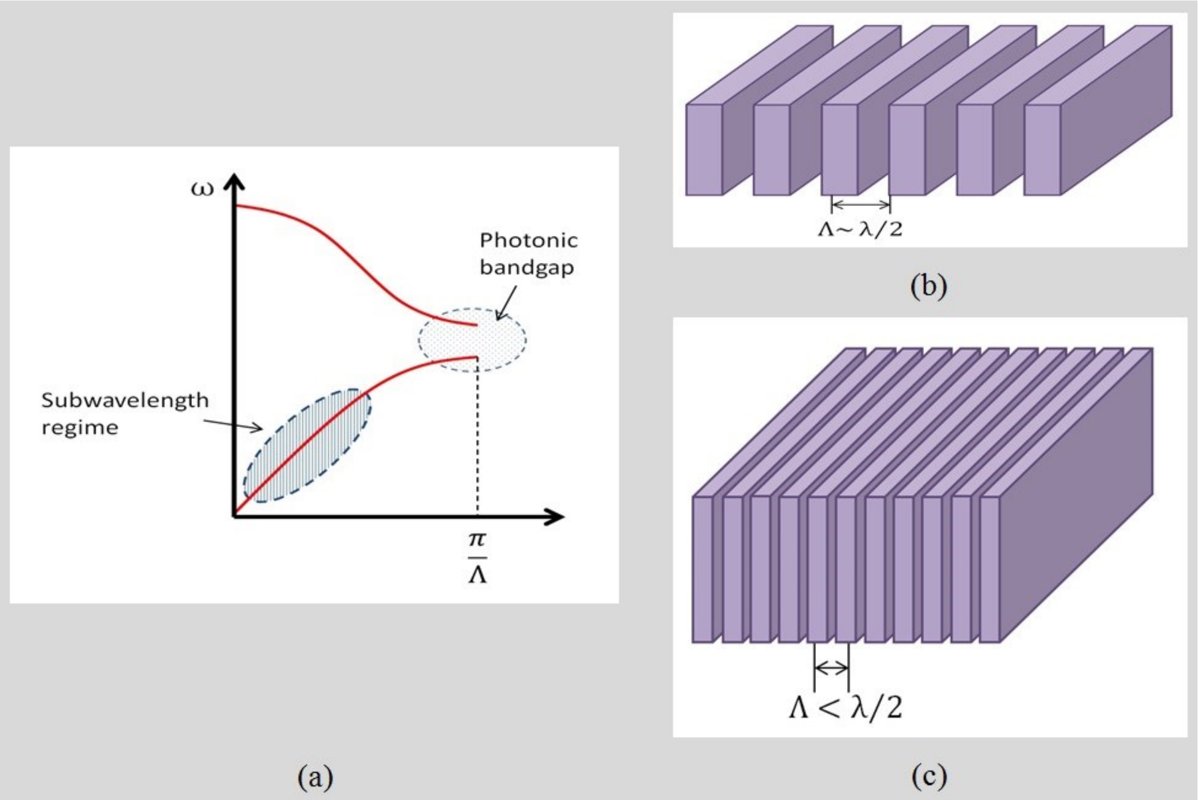

Fig. 4.1. (a) A dispersion diagram illustrating the first two bands of the photonic crystal band structure of the 1D grating shown in (b) & (c). The gratings consist of a periodic stack of plane slabs with alternating high (solid) and low (void) refractive index. The Bloch mode propagates in the direction normal to the plane slabs with a wave-vector $k = 2\pi/\lambda$ and a temporal frequency ω. The resonant region $\Lambda \sim \lambda/2$ corresponding to (b) is shown as the light blue shaded region on (a). The sub-wavelength regime $\Lambda < \lambda/2$ corresponding to (c) is shown in darker blue; in this region the structure behaves as a homogeneous effective medium with an effective refractive index $n_{eff} = c(k/\omega)$ where c is the velocity of light.

In this chapter, it is proposed that the graded (effective media) refractive index of the Lüneburg lens is engineered by patterning a Silicon-On-Insulator (SOI) slab waveguide core layer, using a single etch step, into a dense distribution of cylindrical inclusions; either solid (silicon) or voids (air); in a host that is either void (air) or solid (silicon) respectively. The cylinders may have variable diameters and be placed on a regular lattice, that is advantageously hexagonal, with sub-wavelength pitch. In the case of voids, the patterned silicon may be suspended in air (as is standard practice for photonic crystal slabs) to form the core of a symmetric slab waveguide. Solid cylinders must be supported by the $Si0_2$ layer leading to an asymmetric waveguide structure of reduced effective index range. Photonic wire feeder waveguides at different positions around the lens can be used to launch light into the lenses or collect light from the lenses.

Independently of this work, Gao [75] has reported a design procedure for metamaterial Lüneburg lenses to explain impairments observed in an earlier experimental demonstration. The design procedure draws upon analytic results for the effective media index obtained for 1D lamella gratings and applies them necessarily in an ad hoc fashion to a structure of cylindrical silicon rods on a square lattice to which the design procedure is restricted. The design procedure reported in this thesis is applicable to structures with holes or rods on any lattice.

In Section 4.2, a procedure is developed to determine the local effective media index of a periodic metamaterial in terms of the parameters of its unit cell. In Section 4.3, this calibration is applied to layout a metamaterial with graded parameters. In Section 4.4, the results of FDTD simulations of wave propagation through this graded structure are reported that verify operation as a Lüneburg lens. The results are reported of a full 3D FDTD simulation of light relayed by a telescope formed from two metamaterial Lüneburg lenses between two photonic wire waveguides. The predicted insertion loss of $< 0.25\,dB$ establishes the feasibility of the approach. The chapter closes with a summary in Section 4.5 of the most significant results

4.2 Homogenisation of photonic crystal structure

To enable design, an abstraction procedure is required that summarises the detail of the nanostructure of the metamaterial. The goal is to replace the metamaterial conceptually by some effective media that captures the larger scale behaviour of electromagnetic wave propagation in the bulk and at the surface of the metamaterial preferably in such a way that conventional notions of wave-propagation (e.g. Snell's law and the Fresnel relations) are preserved. The metamaterial of interest in this work has the structure of a 2D photonic crystal slab with 'atoms' in the shape of cylindrical prisms with variable diameter placed on a regular lattice. The first approximation made to attain the goal is to assume that the variation of atom diameter occurs sufficiently gradually spatially that the environment around any unit cell may be accurately approximated by the periodic replication of that unit cell. In other words, locally the graded metamaterial behaves as if it was a perfectly regular photonic crystal with a fixed atom diameter equal to the diameter of the atom found in the local unit cell. This approximation enables one to focus on the homogenisation of a uniform photonic crystal of infinite extent or equivalently a single unit cell with periodic boundary conditions.

It is noted in this context that a natural crystalline material is a composite 'material' of similar structure. It has atoms arrange on a regular lattice that form the inclusions in a vacuum host. Landau and Lifshitz [76] explain how the fundamental equations of the electrodynamics of continuous media are obtained by averaging the equations of the electromagnetic field in a vacuum (in the case of a crystal over its elementary unit cell); a method due to H. A. Lorentz. The averaging process may be considered to define the macroscopic fields and the material constitutive relations between them (i.e. in the case of a dielectric, the relative permittivity). The analysis is tractable because a representative lattice constant a is so much smaller than the wavelength ($ka \ll 1$) and the problem, for a dielectric, reduces to a problem in electrostatics. The macroscopic representation of the fields is highly accurate. Indeed, in this work, the electromagnetic properties of the constituent components of a photonic crystal are described by this representation.

The photonic crystal structure may be homogenised in a similar way. The macroscopic fields of continuous media then play the role of the microscopic fields. New macroscopic fields are obtained by suitable averaging over the unit cell. Linear constitutive relations for the effective medium are then defined by these fields to ensure they obey the macroscopic form of Maxwell's equations. The fact that the representative lattice constant a is only just smaller than the wavelength ($ka \sim 1$) results in linear constitutive relations that can be spatially dispersive (i.e. depend upon $\boldsymbol{k}$) even when the component of the composite material are not spatially or temporally dispersive. Moreover, phenomena which do not occur in nature are possible, such as magnetoelectric coupling [77] and negative refraction [78], which explains the vibrant interest in metamaterials.

A tractable analytic approach to determining the microscopic fields for averaging is not available for $ka \sim 1$ because it is necessary to take full account of retarded fields. However, today advantage may be taken of the availability of numerical tools to compute the microscopic fields of a unit cell which may then be averaged by a suitable homogenisation procedure. The semi-numerical approach was first introduced by Smith & Pendry [77] and placed on a firmer mathematical foundation by Tsukerman [79, 80]. Various flaws in Pendry's approach have been identified by Gozhenko [81]. Xiong [13] identifies a potential pitfall: it may be incorrect to assume the usual boundary conditions for the electromagnetic field at an interface between the homogenised and regular material (this assumption is implicit in the approach described in the sequel to the 1D waveguide confinement correction of the effective index of a 2D photonic crystal slab). The method of Perez-Huerta [83] is appealing because the homogenised permittivity can recreate the entire photonic band structure.

In this work an engineering approach is taken: a photonic crystal band structure solver is used to calibrate the dependence of the effective index on atom diameter. This is equivalent to ignoring the details of the Bloch mode within a unit cell while taking full account of the phase change of the Bloch mode from one side to the other side of the cell. This information is provided by the bandstructure. Two approaches to calculating the effective index as a function of atom diameter have been considered.

1) A 2D band structure solver is used to obtain the effective index of the fundamental Bloch mode in an extended 2D photonic crystal. This effective index is then used as the refractive index of the core of an asymmetric slab waveguide with an upper cladding of air and a lower cladding of silica to calculate the effective index of the fundamental waveguide mode. This correction for waveguide confinement is performed by a Matlab script that finds the roots of the dispersion relation for an asymmetric slab waveguide derived in Appendix IV. This perspective is illustrated in Figure 4.2.

2) A 3D band structure solver for a 2D periodic medium is used to directly solve for the effective index of the fundamental mode. The 3D solver assumes a 3D elemental unit cell with periodic boundary conditions. The 3D unit cell is defined in the plane of the slab by the 2D unit cell of the photonic crystal slab lattice, and it is defined by the device structure in the direction normal to the plane of the slab, i.e. the air / metamaterial / substrate layers. The implicit assumption that there are an infinite number of replications of the 3D unit cell normal to the plane of the slab is an approximation given that the slab

is only one unit cell thick. The real structure is not at all periodic in the third direction. However, the Bloch modal fields found decay rapidly away from the core and are essentially zero at the device boundaries for air and substrate cladding layers 2 μm thick; there should be little error in the fields caused by the assumed periodicity. It is therefore expected that the 3D band structure solver for a 2D periodic medium yields an accurate value of the effective index of the metamaterial that fully accounts for the 1D waveguide confinement. This perspective is illustrated in Figure 4.3.

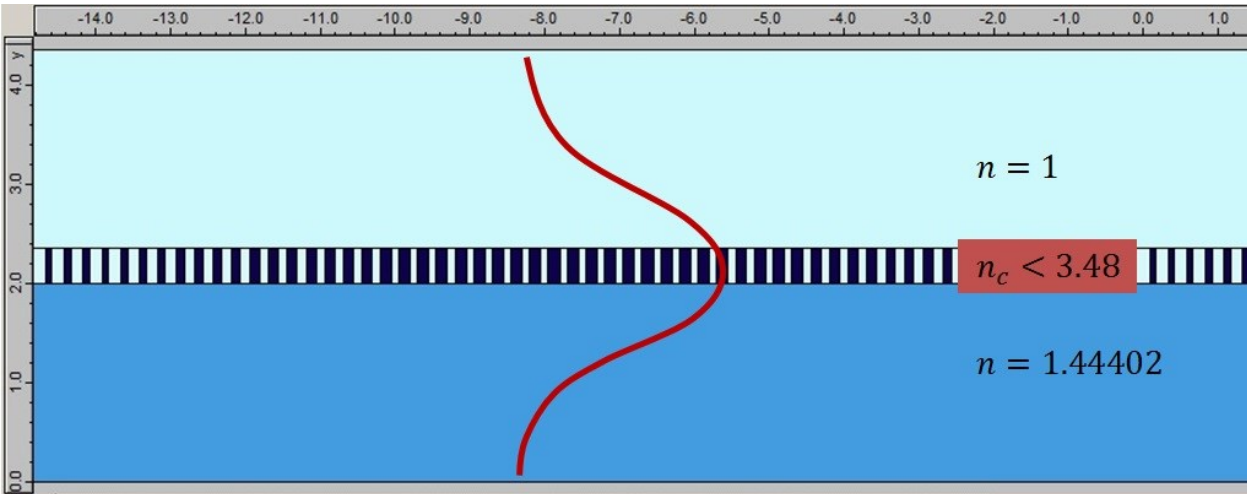

Fig. 4.2. A side view of the planar metamaterial lens structure with an overlaid schematic of the fundamental mode field amplitude distribution emphasising the waveguide perspective. The subwavelength binary structure acts locally as a continuous effective medium with a graded refractive index that forms the core material of an asymmetric slab waveguide that confines the mode.

The goal of either method is to obtain an accurate value of the '3D' effective index as a function of atom diameter to enable a script that creates the device structure to generate atoms of the correct diameter given a specified local effective index. The design can then be verified by a 3D FDTD simulation of propagation in a graded 'metamaterial' i.e. a 3D FDTD simulation of a photonic crystal slab with a spatially slowly varying atom size. In this work, the slab has an upper cladding of air and a lower cladding of silica and the 'atoms' are either silicon rods in an air host or air holes in a silicon host.

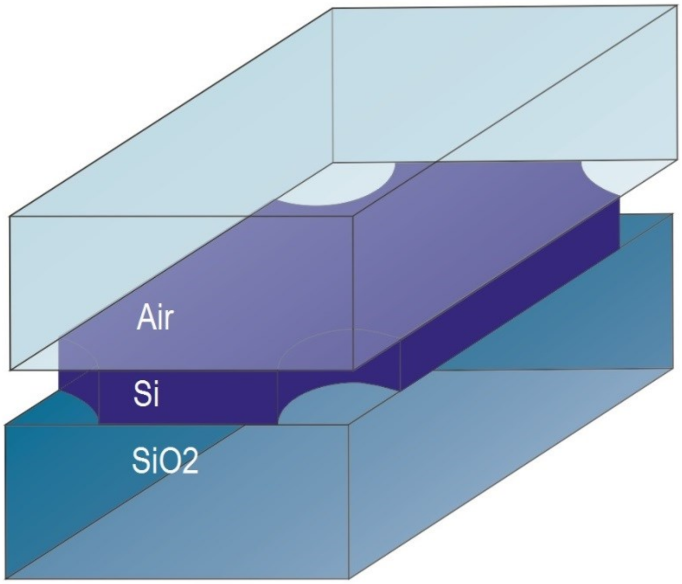

Fig. 4.3. A view of a 3D unit cell emphasising the 3D photonic crystal perspective. The 3D cell is formed by the 2D unit cell of the photonic crystal slab lattice extended in the normal to the plane of the slab through the lower cladding, photonic crystal slab core, and upper cladding layers of the device.

4.3 Effective index versus atom diameter calibration

The validity of the homogenisation procedures discussed in the Section 4.2 was investigated by numerical experimentation using the CrystalWave package of the Photon Design suite of software tools. Consistent with the emphasis of this thesis, a SOI integration platform was selected with a silicon layer 220 nm or 350 nm thick. Cylindrical atoms on a regular hexagonal lattice with a lattice constant of 250 nm were selected because cylinders are more easily fabricated than other shapes and a pitch of 250 nm is within the range of deep UV lithography. The hexagonal lattice then offers higher packing densities than other plane lattices. The fill factor f for cylinders of diameter d arranged on a hexagonal lattice with lattice constant p is:

$$f = \frac{\pi}{2\sqrt{3}} \frac{d^2}{p^2} \leq 0.9$$

Equation 4.1

For comparison, the corresponding fill factor for a square lattice is:

$$f = \frac{\pi}{4}\frac{d^2}{p^2} \le 0.79$$

Equation 4.2

The choice of silicon rods or air holes for the inclusions has an effect on the range of effective media indices that may be reached. Air holes permit the highest effective medium index to reach the refractive index of silicon ($n_{si} = 3.47772$) and silicon rods permit the lowest effective medium index to reach the refractive index of air ($n_{air} = 1.0$). However, the effective index of the mode cannot be lower than the higher of the refractive index of the upper or lower cladding. Mechanical considerations mean that silicon rods must be supported on a silica substrate limiting the lowest effective index of the mode to the refractive index of silica ($n_{SiO_2} = 1.44402$). A slab with air holes can be suspended by an under etch which permits the effective index of the mode to reach below the refractive index of silica. The effective index of the mode is always lower than the refractive index of the core as a consequence of waveguide confinement. The thickness of the silicon layer determines the height of the rods or holes and therefore has a bearing on the highest achievable effective index of the mode.

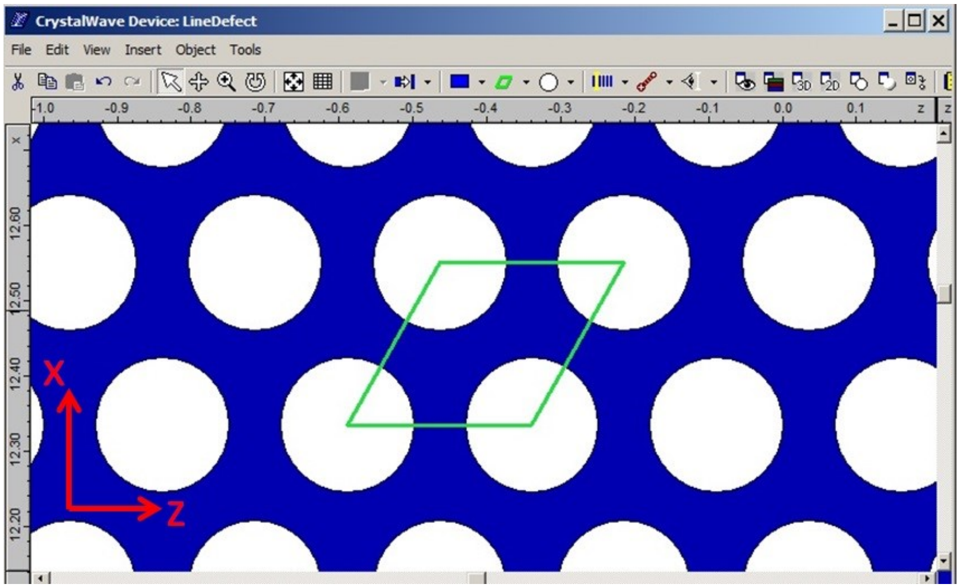

Fig. 4.4. A unit cell for silicon rods of diameter 180 nm in an air host on a regular hexagonal lattice of lattice constant 250 nm.

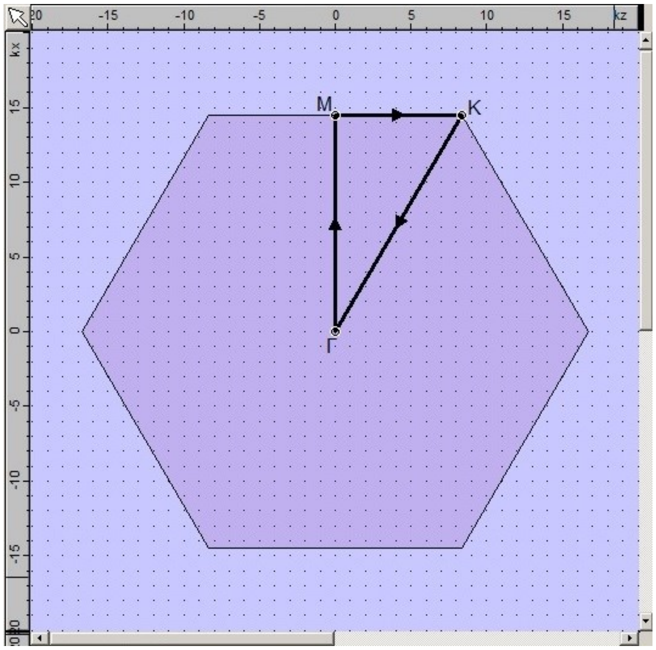

Fig. 4.5. The k-space diagram of the conventional ΓMKΓ path for a 2D hexagonal lattice with the lattice constant of 250 nm.

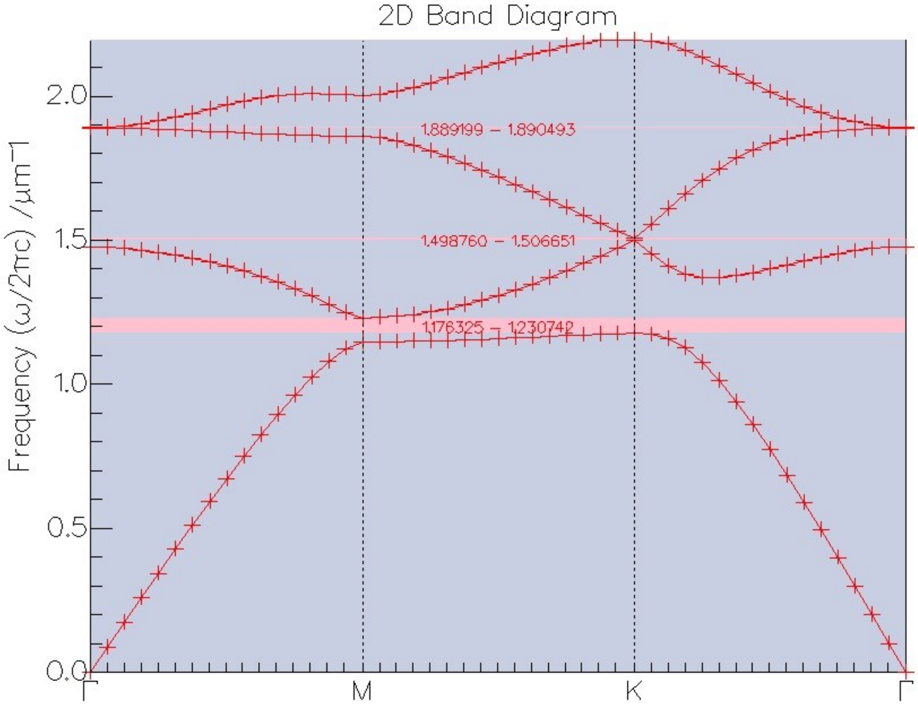

Fig. 4.6. The 2D photonic crystal band diagram for TE polarisation for silicon rods of diameter 180 nm on a regular hexagonal unit cell with a lattice constant of 250 nm. The plot is a section along the ΓMKΓ path through the 2D band surfaces above the 2D wavevector plane. Note there are 16 equispaced axis markers along each segment of the ΓMKΓ path.

Figure 4.4 shows an example of the unit cell in the CrystalWave window for silicon rods with a diameter of 180 nm in an air host. Figure 4.5, Figure 4.6 and Figure 4.7 provide different views of the corresponding 2D photonic band structure diagram for the TE mode as calculated by the CrystalWave 2D band solver. As illustrated in Fig 4.1, the working region of interest is the lower band in Fig. 4.6, preferably close to the Γ point where the band is most linear. This region corresponds to the conical depression of the band surface shown in Fig.4.6. The local rotational symmetry of the base region of this cone is confirmed by the equifrequency contours shown in Figure 4.7, which remain close to circles for a broad range of frequencies up to and to a certain extent beyond $0.7\ \mu\text{m}^{-1}$. This is indicative of a minimal dependence of the effective index on the direction of propagation. However, at the operating vacuum wavelength of $\lambda_0 = 1550\ \text{nm}$, which corresponds to a frequency of $0.6451\ \mu\text{m}^{-1}$ in the units used in Fig. 4.6, there is a slight deviation from the long-wavelength asymptote. The effective index versus atom diameter dependence was therefore calibrated by reading from a sequence of the 2D band structure diagrams the datum at the closest point to a frequency of $0.6451\ \mu\text{m}^{-1}$ as the diameter of the atoms was varied from 10 nm to 236 nm. The results are plotted in Figure 4.9 and Fig 4.10.

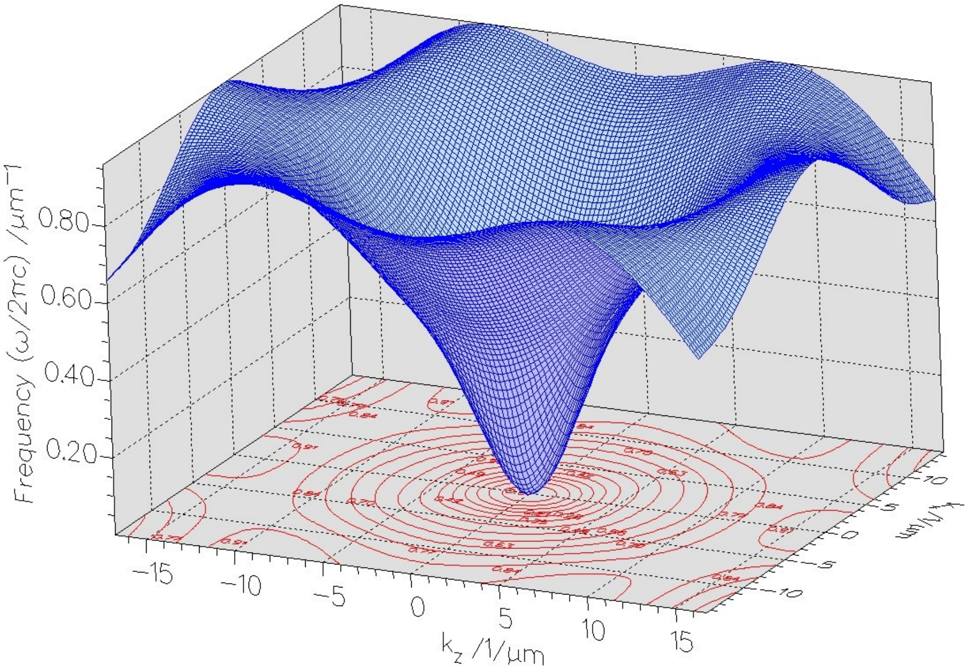

Fig. 4.7. The lower band of Fig 4.6 displayed in perspective over the whole of the wavevector space.

Although the Maxwell-Garnet mixture formula [71]:

$$n_{eff}^2 = n_h^2 \frac{(1+2f)n_i^2 + 2n_h^2(1-f)}{(1-f)n_i^2 + (2+f)n_h^2}$$

Equation 4.3

predicts the general trend there is a significant difference between its prediction and the effective index obtained from the band structure data.

The 2D analysis assumes inclusions that are infinitely long cylinders whereas in practice the inclusions are slices of cylinders with lengths of the same order as their width. In Fig 4.12(a) a comparison is made between the two approaches described in Section 4.2 for predicting the effective index of the fundamental mode of a 2D photonic crystal slab. The agreement can be seen to be excellent ($< 2\%$ error). To obtain good results from the 3D solver for a 2D periodic medium, the effective index was evaluated for different sampling resolutions in the direction normal to the plane of the slab waveguide. Good accuracy was found with 128 samples, which was selected as a compromise between precision and computation time. The dependence of the effective index is monotonic on the resolution, which suggests that a further increase in sampling resolution might reduce the apparent systematic, albeit small, disagreement between the 3D band solver result and the 1D confinement corrected 2D band solver result.

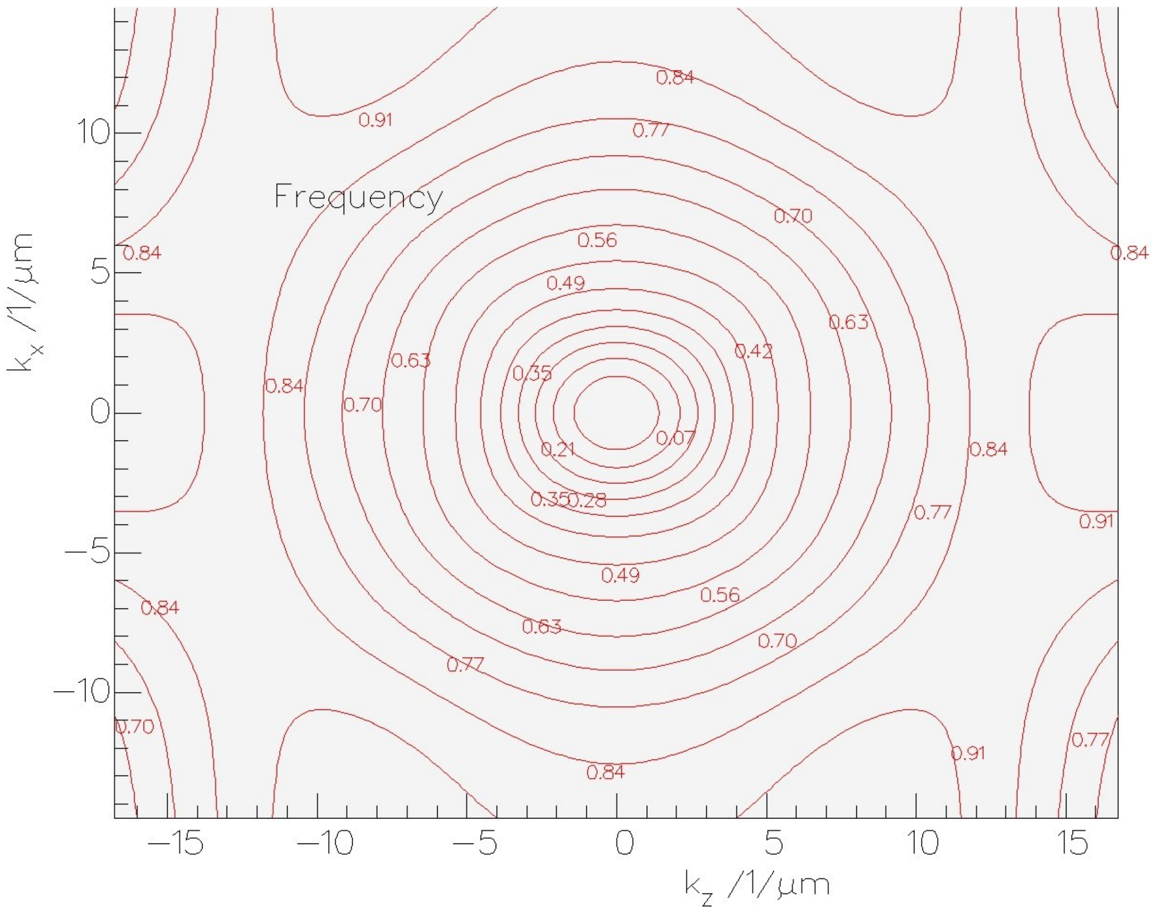

Fig. 4.8. The equifrequency contours of the band surface shown in Fig. 4.7 displayed on the wave vector plane.

The close agreement between the bulk refractive index of a 2D photonic crystal corrected for 1D waveguide confinement and the effective index found from a fully 3D photonic band structure calculation augurs well that the nanostructured core material is behaving as continuous effective medium.

The final result, Fig. 4.12, is remarkable for its close fit to a linear dependence on fill-factor except close to cut-off where one would expect a linear extrapolation to fail because it would predict an effective index close to or lower than the lower cladding index.

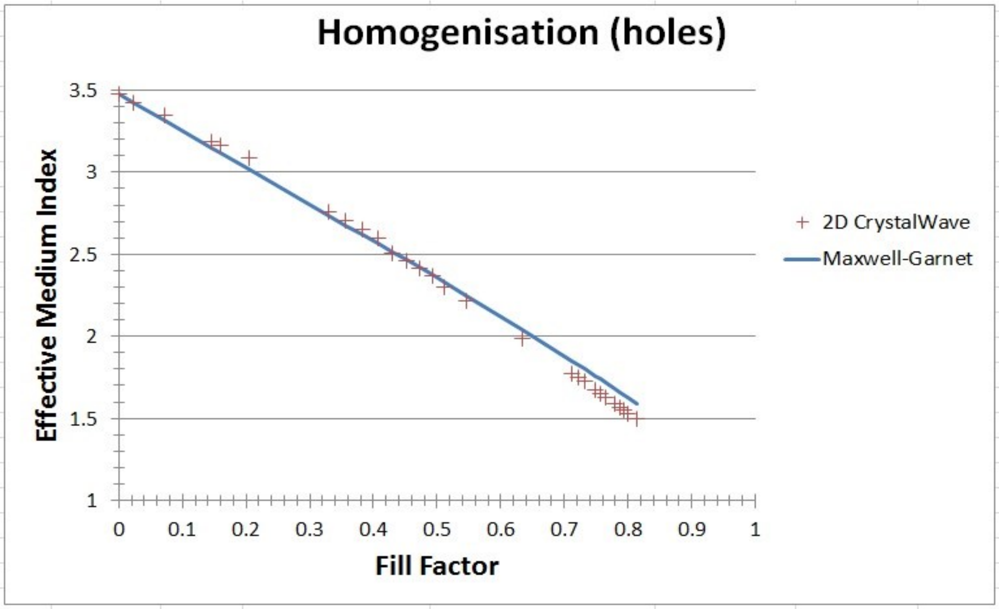

Fig. 4.9. The effective medium index of a 2D Photonic Crystal with cylindrical air holes placed on a regular hexagonal lattice with a lattice constant of 250 nm in a silicon host.

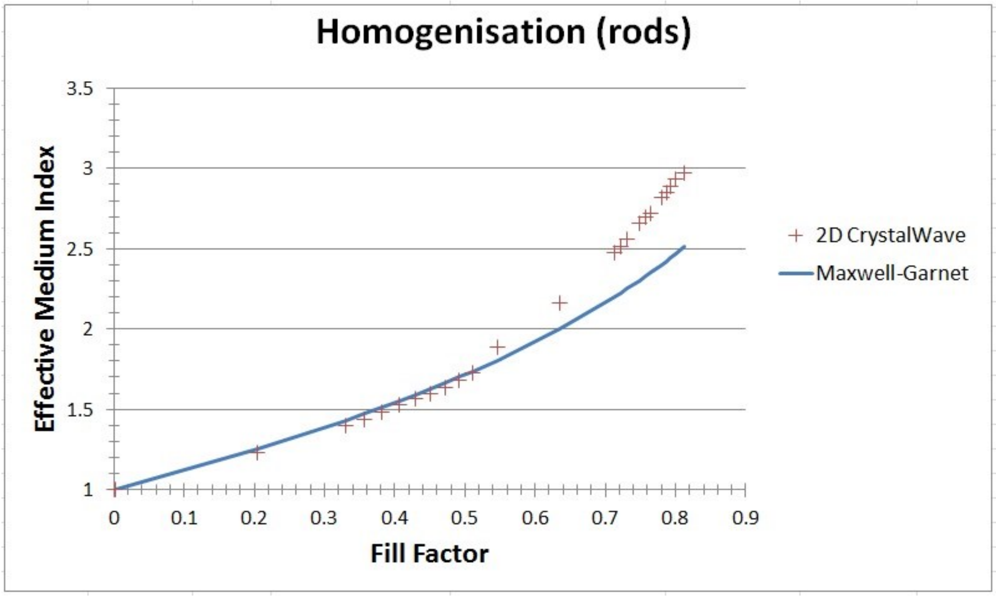

Fig. 4.10. Effective Medium Index of a 2D Photonic Crystal with cylindrical silicon rods placed on a regular hexagonal lattice with a lattice constant of 250 nm in an air host

The 3D analysis is done using the 3D band solver for 2D periodic structure. The solver obtains the periodic conditions in the plane from the silicon layer that has a 2D periodic structure. Then it approximates the problem by replicating the whole device structure out of the plane, hence, finding a 3D unit cell with 3D boundary conditions. However here the device is not periodic out of plane, it is being approximated by a structure that is periodic. The field is near zero at the top and bottom boundaries which are equated under the replication. The effective refractive index is calculated from the TE band of the band diagram in figure 4.11, which is an example for the hole size of 180 nm.

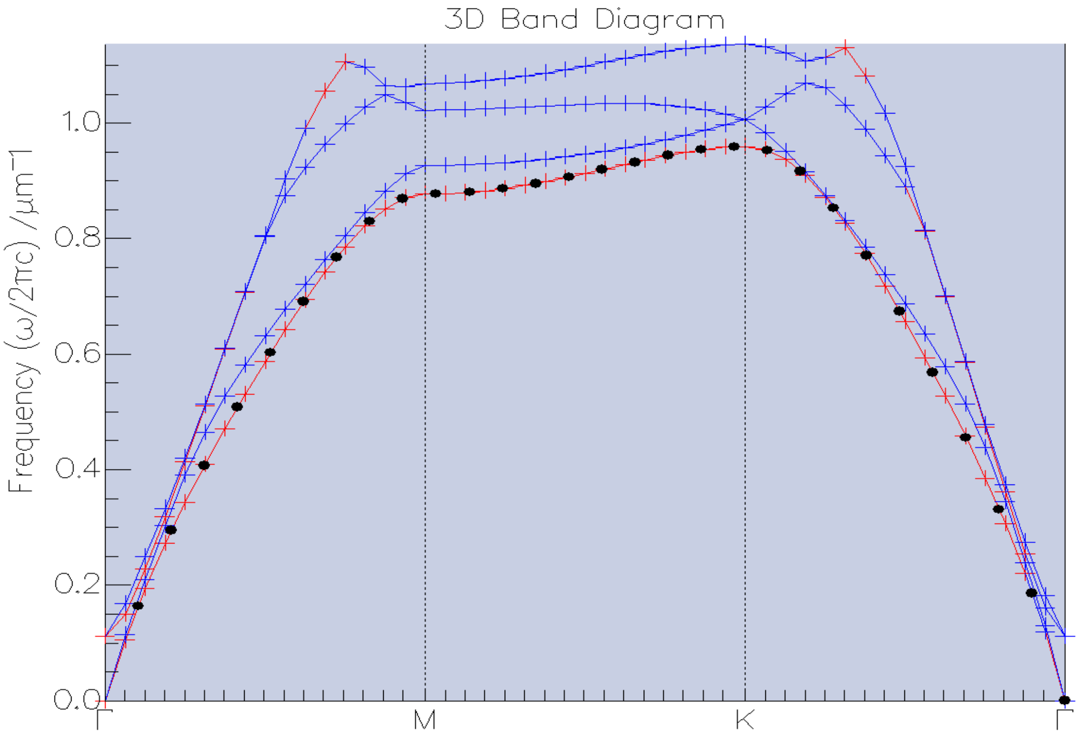

Fig. 4.11. The 3D photonic crystal band diagram for TE (red), also highlighted by the bold dots) and TM (blue) polarisations for silicon holes of diameter 180 nm on a regular hexagonal unit cell with a lattice constant of 250 nm. Note there are 16 equispaced axis markers along each segment of the ΓMKΓ path.

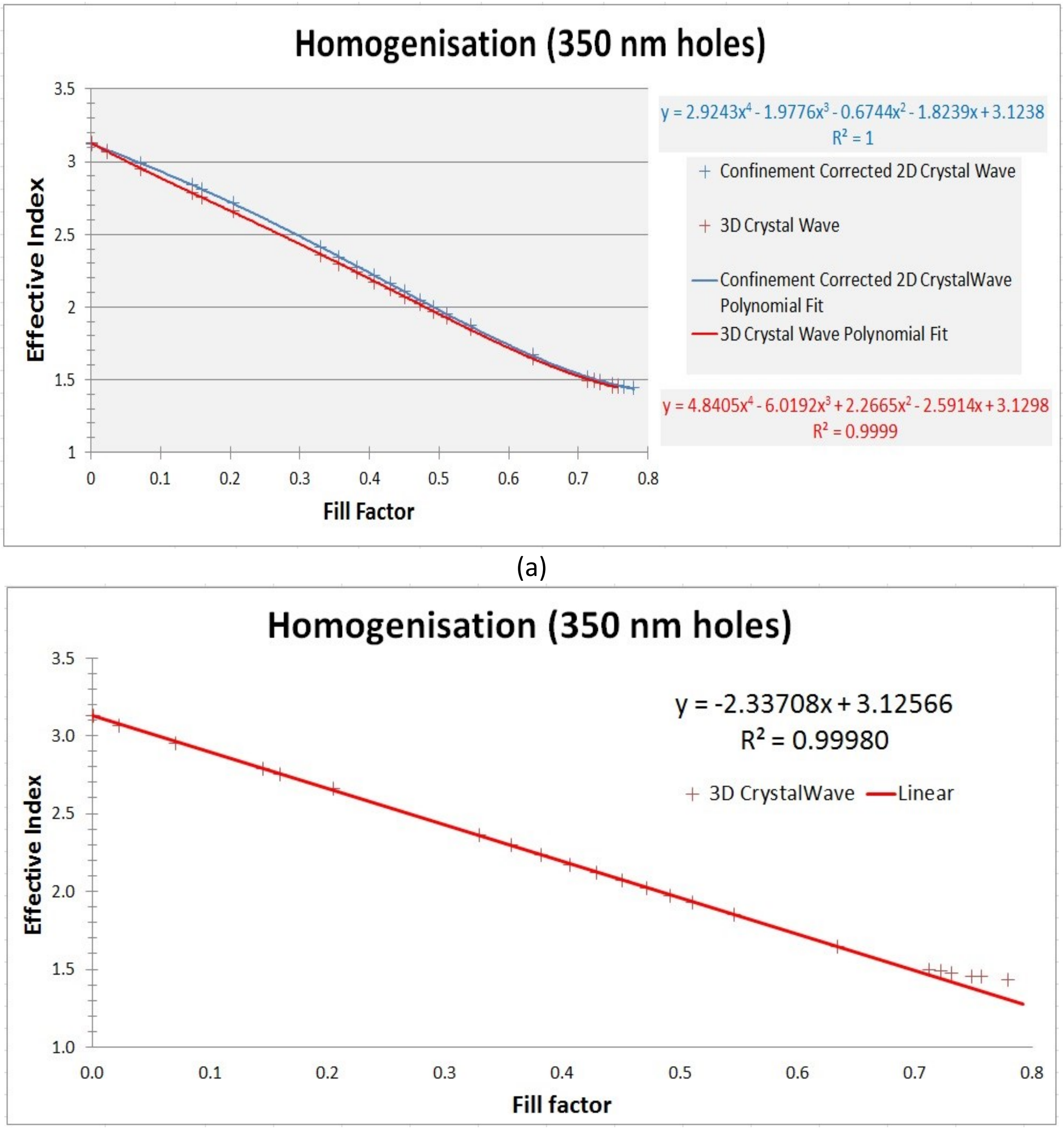

(a)

(b)

Fig. 4.12. The effective index for the fundamental mode of a photonic crystal slab waveguide with a 350 nm thick silicon core host with cylindrical air holes placed on a regular hexagonal lattice with a lattice constant of 250 nm; (a) there is good agreement between 3D band structure solver and the 1D confinement corrected 2D band structure solver methods of finding the effective index; (b) there is excellent agreement between the dependence of the data on fill factor and a linear dependence except near to cut-off where the effective index approaches the refractive index of the lower cladding.

4.4 FDTD simulations of metamaterial lenses & telescopes

2D and 3D FDTD simulations were performed using CrystalWave to verify the optical behaviour of the graded metamaterials. These simulations required the definition of the graded nanostructure just as masks are required for fabrication. These nanostructures are so complex that their layout must be automated. Fortunately, the CrystalWave tool may be automated using a Python script and the device structure may be exported as a GDSII file into a layout tool to facilitate mask generation. An outline is given in this section of the Python script that was developed to generate the structure of the metamaterial Lünburg lenses that were simulated in this work. It also explains why a form of quantisation is necessary to automate layout.

Two Bravais vectors $\boldsymbol{b}_1$ and $\boldsymbol{b}_2$ are defined to describe the position of the atoms on the plane (Figure 4.13).

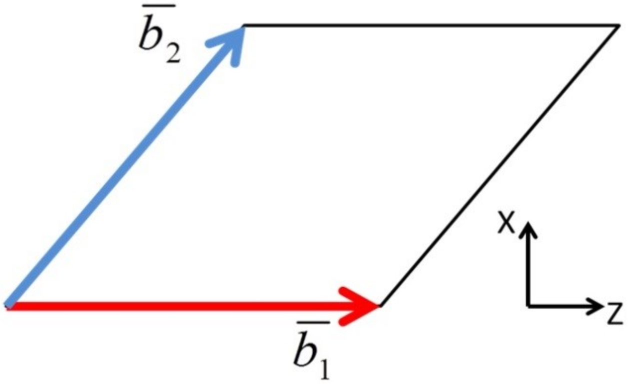

Fig. 4.13. The Bravais vectors that define the unit cell of a lattice in the plane.

For a regular hexagonal lattice with lattice constant b and a Cartesian co-ordinate system these vectors may be expressed as:

$$\boldsymbol{b}_1 = b\begin{bmatrix}1\\0\end{bmatrix} , \qquad \boldsymbol{b}_2 = b\begin{bmatrix}\frac{1}{2}\\\frac{\sqrt{3}}{2}\end{bmatrix}$$

Equation 4.4

Since these two vectors are linearly independent, any vector in the plane $\boldsymbol{q}$ may be expressed as:

$$\boldsymbol{q} = c_1\boldsymbol{b}_1 + c_2\boldsymbol{b}_2$$

Equation 4.5

where c_1 and c_2 are scalars.

Let $\boldsymbol{b}_1{}^{\perp}$ and $\boldsymbol{b}_2{}^{\perp}$ denote two vectors that are orthogonal to $\boldsymbol{b}_1$ and $\boldsymbol{b}_2$ respectively. That is:

$$\begin{gathered} \boldsymbol{b}_1.\boldsymbol{b}_1{}^{\perp} = 0 \\ \boldsymbol{b}_2.\boldsymbol{b}_2{}^{\perp} = 0 \end{gathered}$$

Equation 4.5

a suitable choice is:

$$\begin{gathered} \boldsymbol{b}_1{}^{\perp} = \boldsymbol{J}\boldsymbol{b}_1 \\ \boldsymbol{b}_2{}^{\perp} = \boldsymbol{J}\boldsymbol{b}_2 \\ \boldsymbol{J} = \begin{bmatrix} 0 & 1 \\ -1 & 0 \end{bmatrix} \end{gathered}$$

Equation 4.6

It follows that the lattice coordinates corresponding to the position $\boldsymbol{q}$ are:

$$c_1 = \frac{\boldsymbol{q}.\boldsymbol{b}_2{}^{\perp}}{\boldsymbol{b}_1.\boldsymbol{b}_2{}^{\perp}}\ , \qquad c_2 = \frac{\boldsymbol{q}.\boldsymbol{b}_1{}^{\perp}}{\boldsymbol{b}_2.\boldsymbol{b}_1{}^{\perp}}$$

Equation 4.7

In CrystalWave the atoms on a lattice are indexed by integers that correspond to the values (c_1, c_2) take when the position vector $\boldsymbol{q}$ points to the lattice site. By appropriately incrementing c_1 and c_2 atoms may be visited sequentially in an area that contains a region of interest. At each lattice point visited $\boldsymbol{q}$ may be tested to determine if the atom lies in the region of interest. If it does then the required effective index at that point is looked-up, for example, using the Lüneburg refractive index distribution (Equation 3.20). A polynomial fit of the fill factor as a function of the effective index determined by the calibration process described in Section 4.3 then permits the diameter of the atom to be determined. Ideally, the atom's properties could then be updated with the new diameter. In practice, an atom from a predetermined palette of atoms is substituted that is closest in terms of the desired property (effective index). The palette is constructed by quantising the desired refractive index range and defining a representative atom for each quantisation level using the calibration polynomial. A palette containing 100 atoms was used in the simulations herein. Note that the calibration polynomial used depends upon whether a 2D or 3D simulation is to be performed.

As an example, Figure 4.14 shows a circular Lüneburg lens that was defined with a diameter of 15 μm and the centre at $(0\ \mu\text{m}, 7.5\ \mu\text{m})$ with rod diameters that vary from 151 nm on the rim to 202 nm in the centre placed on a hexagonal lattice with a lattice constant of 250 nm. The effective refractive index on the rim was set to 1.4 and consequently in the centre it will be $1.4 \times \sqrt{2} = 1.98$. The calibration polynomial was appropriate to a 2D FDTD simulation.

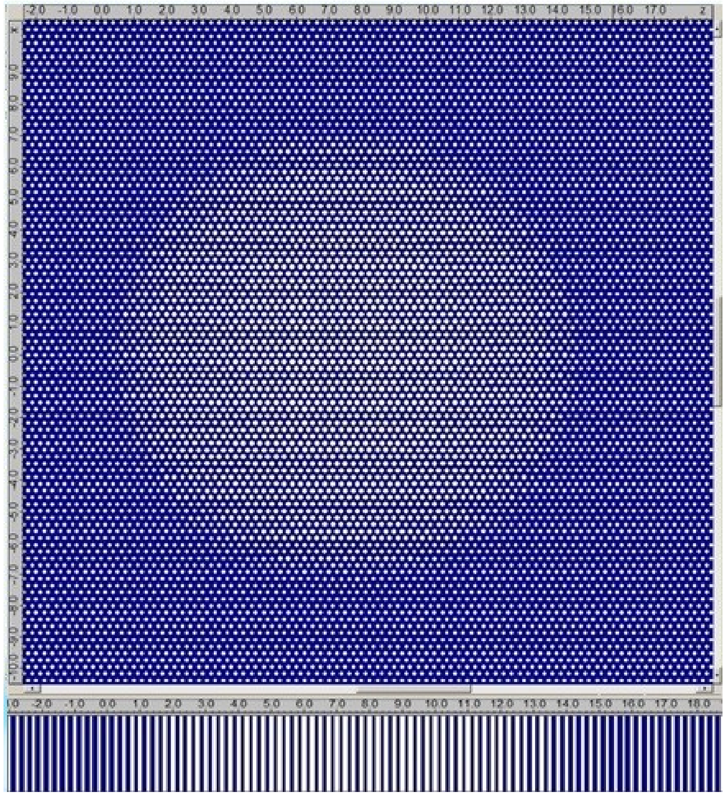

Fig. 4.14. A metamaterial Lüneburg lens with a diameter of 15 μm; centre at $(0\ \mu\text{m}, 7.5\ \mu\text{m})$ with the rod diameters varying from 151 nm on the rim to 202 nm in the centre placed on a hexagonal lattice with lattice constant of 250 nm. The effective refractive index on the rim was set to 1.4, which leads to an effective index at the centre of the lens of 1.98. The calibration used was appropriate to 2D FDTD simulation.

Figure 4.15 illustrates a 2D FDTD simulation of the collimation of a wave emitted by a continuous wave (CW) point source with vacuum wavelength 1550 nm placed on the rim of the lens. The transformation by the metamaterial lens of the spherical wave emitted by the point source into a plane wave is clearly evident.

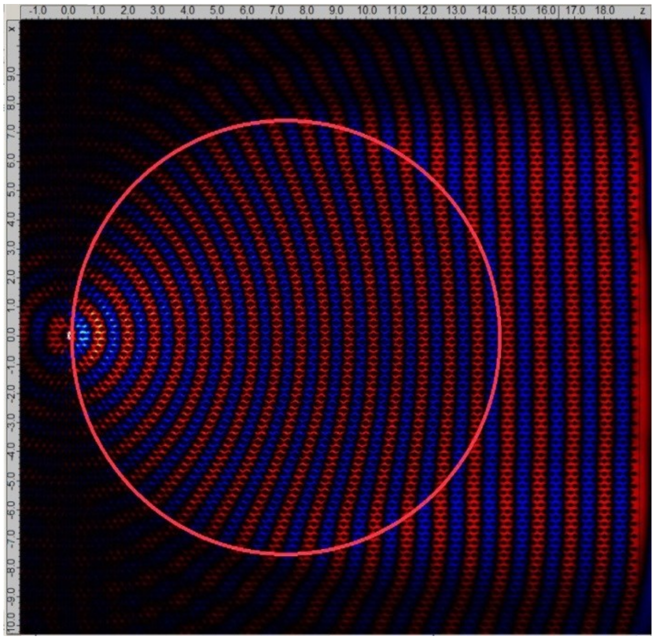

Fig. 4.15. A 2D FDTD simulation of the lens shown in Fig 4.14 excited by a CW point source with vacuum wavelength 1550 nm placed on the rim of the lens.

To assess any degradation in insertion loss as a consequence of approximating a continuous graded index material by a graded metamaterial, two lenses are placed side-by-side with their rims touching on axis to form a confocal telescope (Figure 4.16). Two monomode waveguides are used as input and output ports. The waveguides are designed to have a mode effective index of 1.4 to match the effective refractive index of the lens on the rim to avoid any reflection because of a sudden change of refractive index. The width of the waveguides is 1.575 μm, and the diameter of the lenses is 15 μm.

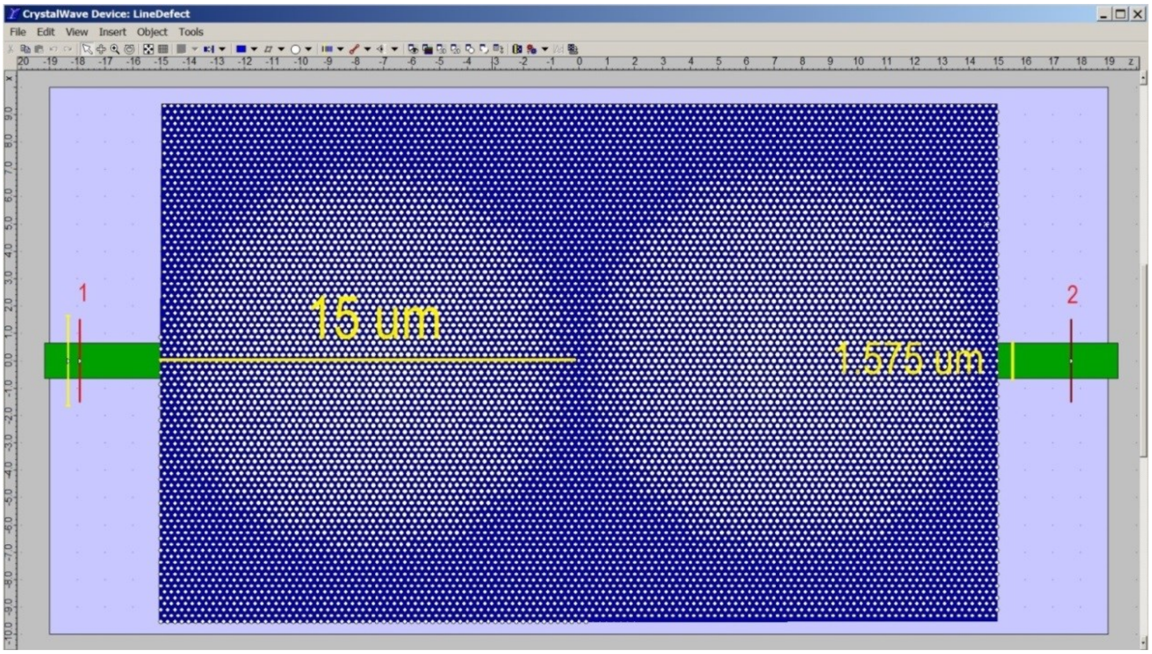

Fig. 4.16. Two lenses side-by-side with rims touching at a point on axis with two feeder waveguides providing an input and output port are used to assess the excess insertion loss of a metamaterial implementation of Lüneburg lenses. The effective refractive index of the waveguides is 1.4 matching the effective refractive index of the lens at the rim. The width of the waveguides is 1.575 µm, and the diameter of the lenses is 15 µm.

A 2D FDTD simulation was performed. The small size of the rods required a computational with grid spacing of 7 nm to adequately represent their shape and hence deliver an accurate result. Figure 4.17 shows a simulation of the successful imaging by the metamaterial Lüneburg lens telescope of the field exiting input waveguide excited by a CW source to the field entering the output waveguide.

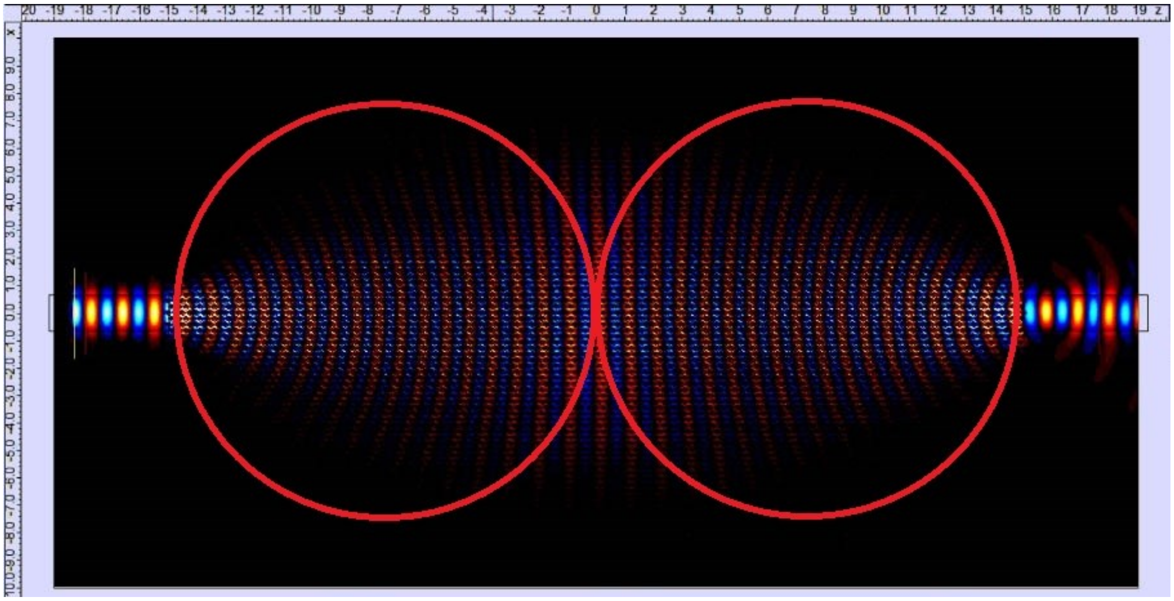

Fig. 4.17. A 2D FDTD simulation of a confocal metamaterial Lüneburg lens telescope between two optical waveguides. A computational grid spacing of 7 nm and a CW source were used.

Although useful for visualisation, CW sources do not provide accurate relative flux measurements. For the analysis of the insertion loss, a TE mode excitor using a pulsed sinusoidal field with duration of 50 fs was used. The 2D FDTD simulation yielded an -0.45 dB insertion loss from waveguide to waveguide via the two lenses. Figure 4.18 shows the intensity profile at input and output waveguide, which confirms minimal aberrations of the modal field.

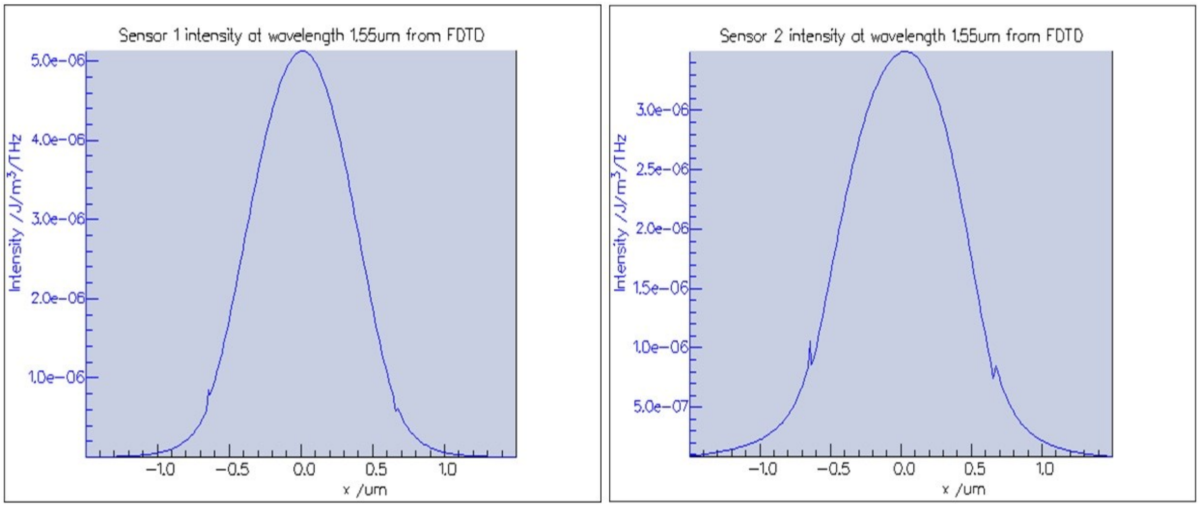

Fig. 4.18. The intensity profile of the field at the input waveguide (left), and at the output waveguide (right) for the two metamaterial lens system.

The insertion loss measured by 2D FDTD for metamaterial Lüneburg lenses is commensurate with the loss measured by 2D FDTD for continuous graded index Lüneburg lenses which augers well that a metamaterial implementation of the Lüneburg lenses will not significantly degrade performance.

The 3D simulation was performed by defining the three layers as is shown in Figure 4.19, air, silicon and silica with the thickness of 2 µm, 0.35 µm and 2 µm respectively. However the 3D simulation needs more memory RAM and takes a longer time for a simulation run. There is a possibility of using a computer cluster to solve the problem of lack of memory on a single computer, but that also introduces the complexity of dividing the sensors across several cluster nodes to calculate the field on the sensor. The accuracy of the simulation may be compromised by both a too coarse computational grid due to inadequate sampling of nanostructure and by a too fine computational grid due to the accumulation as the wave propagates of numerical round-off errors.

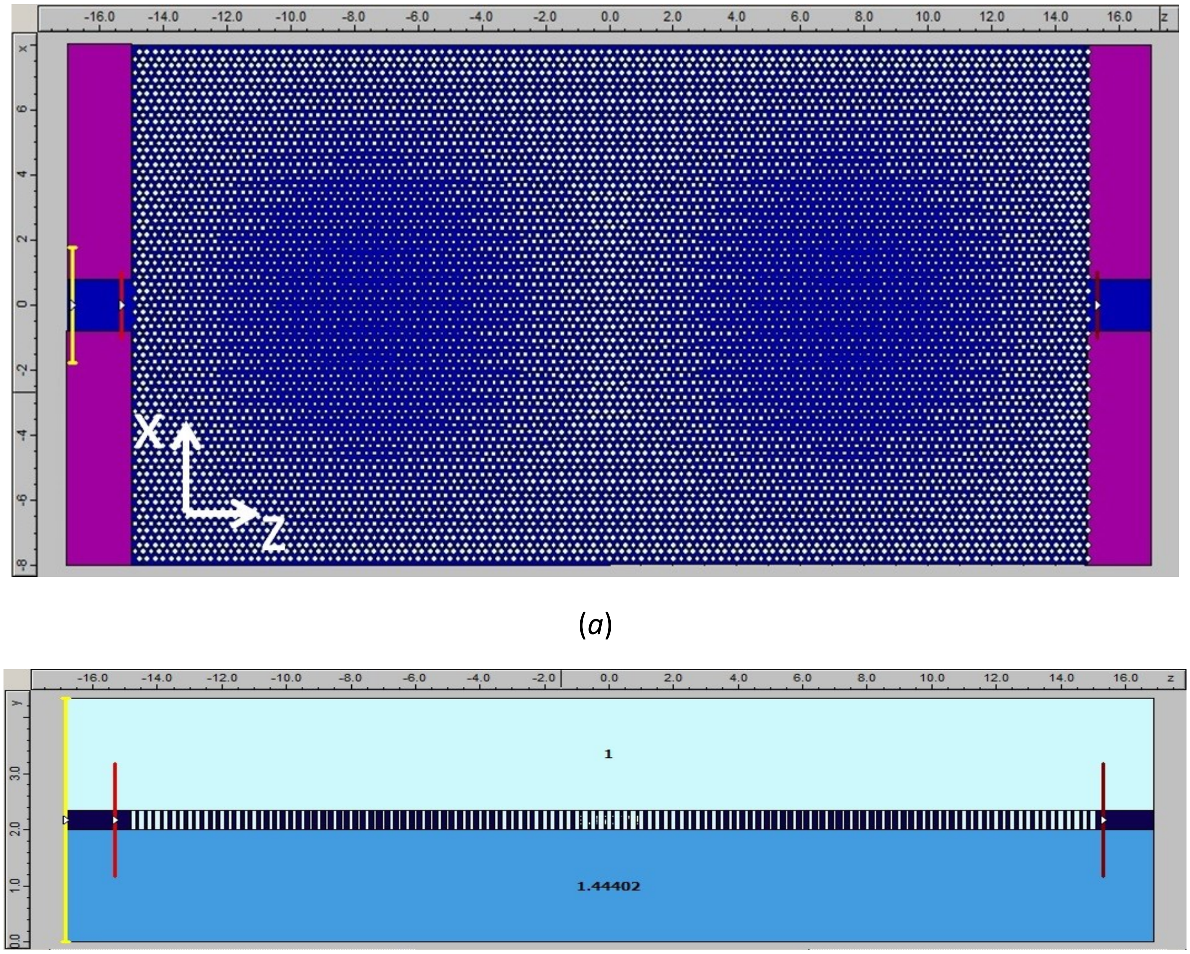

(a)

(b)

Fig. 4.19. Two lenses side-by-side in a 3D structure with three layers of air, silicon and silica with the thickness of 2 μm, 0.35 μm and 2 μm respectively. The rims are touching at a point on axis. Two feeder ridge waveguides provide an input and output port to assess the excess insertion loss of a metamaterial implementation of Lüneburg lenses. The width of the waveguides is 1.575 μm, and the diameter of the lenses is 15 μm. The diameter of the holes varies from 0.1821 μm at the rim to 0.0938 μm at the centre. (*a*) is the top view of the structure and (*b*) is the cross section at $x = 0$, showing the variation of the diameter of holes in lens structures.

Moreover, as refreshing the simulation field view makes the cluster run slower, the simulation must be performed blind, i.e. without observing the field propagation. This creates difficulties in the estimation of the duration of simulation which must be set in advance and in the interpretation of an unexpected result of the identification of an error in the way the simulation is set-up that can be corrected.

Figure 4.20 shows a sequence of frames of 3D simulation of a telescope structure, similar to Figure 4.17 but with the full three layers and a waveguide width of 1.575 μm. To produce this figure it was necessary to set the grid spacing to 28 nm to be able to perform the simulation on a single node. This grid spacing is too coarse for this problem and is likely the main cause of the lower quality of the field profile on exit shown in Fig. 4.21. Nevertheless the predicted insertion loss is -0.83 dB which is acceptable.

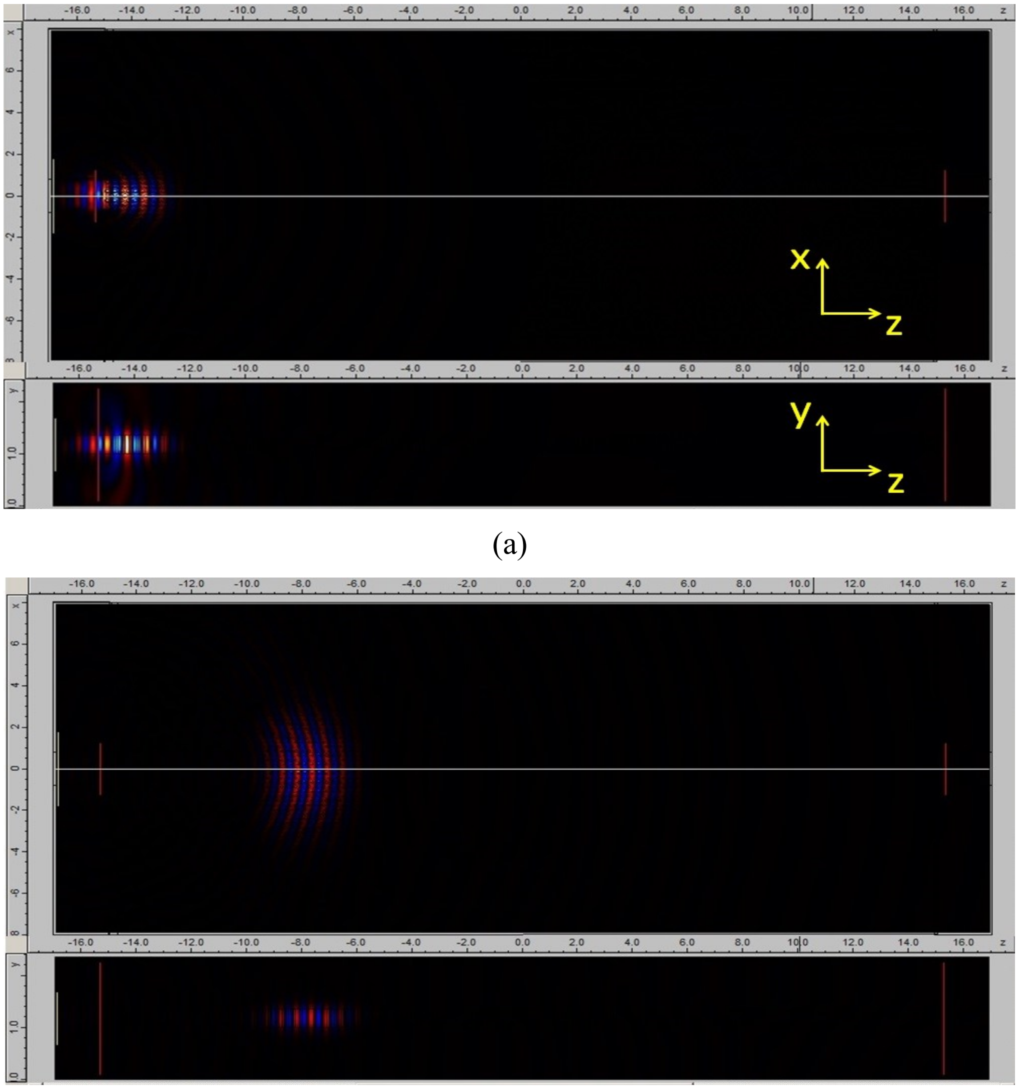

(a)

(b)

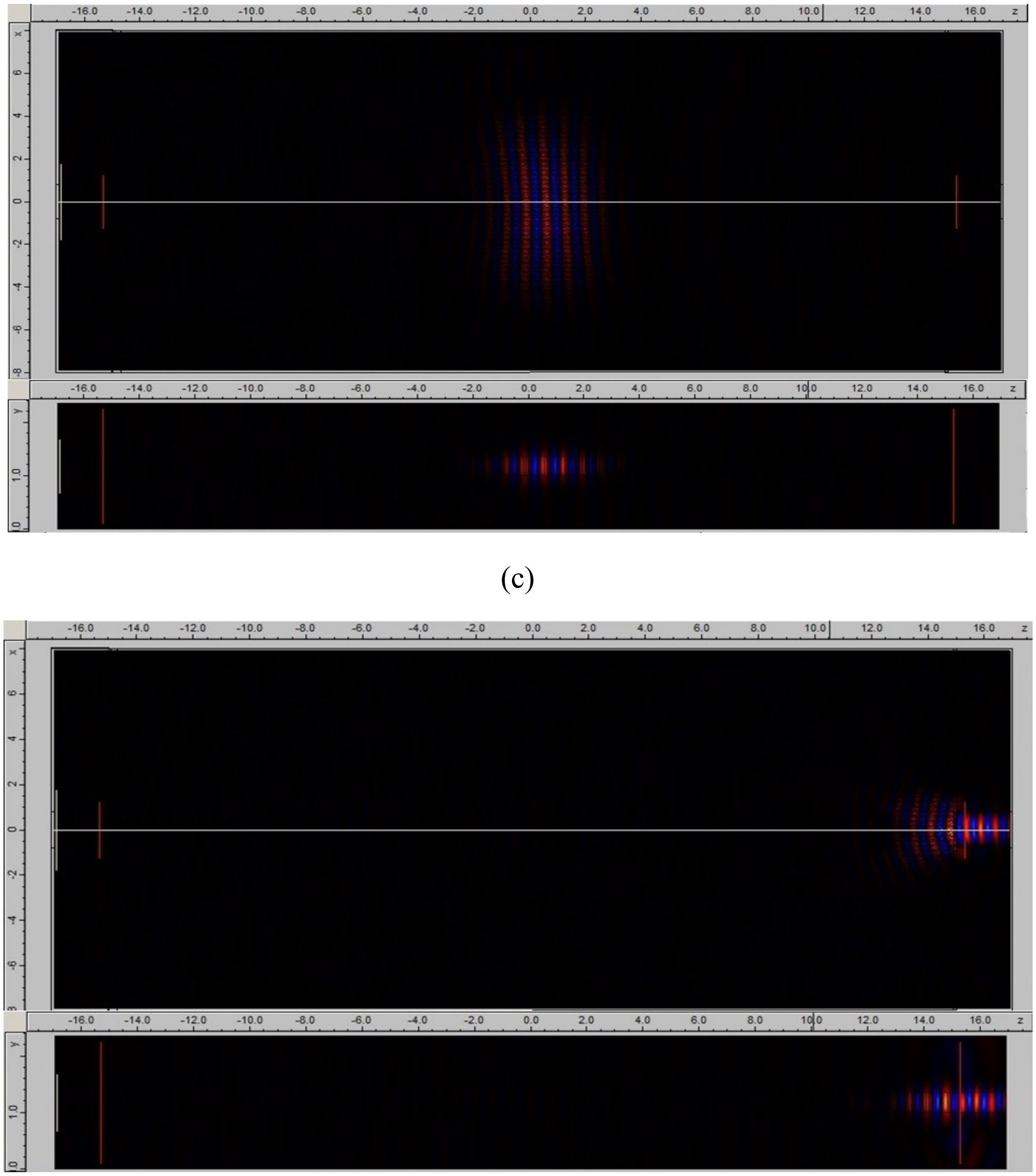

(c)

(d)

Fig. 4.20. A sequence of frames of a 3D FDTD simulation of a confocal metamaterial Lüneburg lens telescope between two optical waveguides. A computational grid spacing of 28 nm and a mode excitor source with the sinusoidal pulse of 50 fs duration, for hole diameter changing from 0.1821 μm on the rim to 0.09381 μm in the centre.

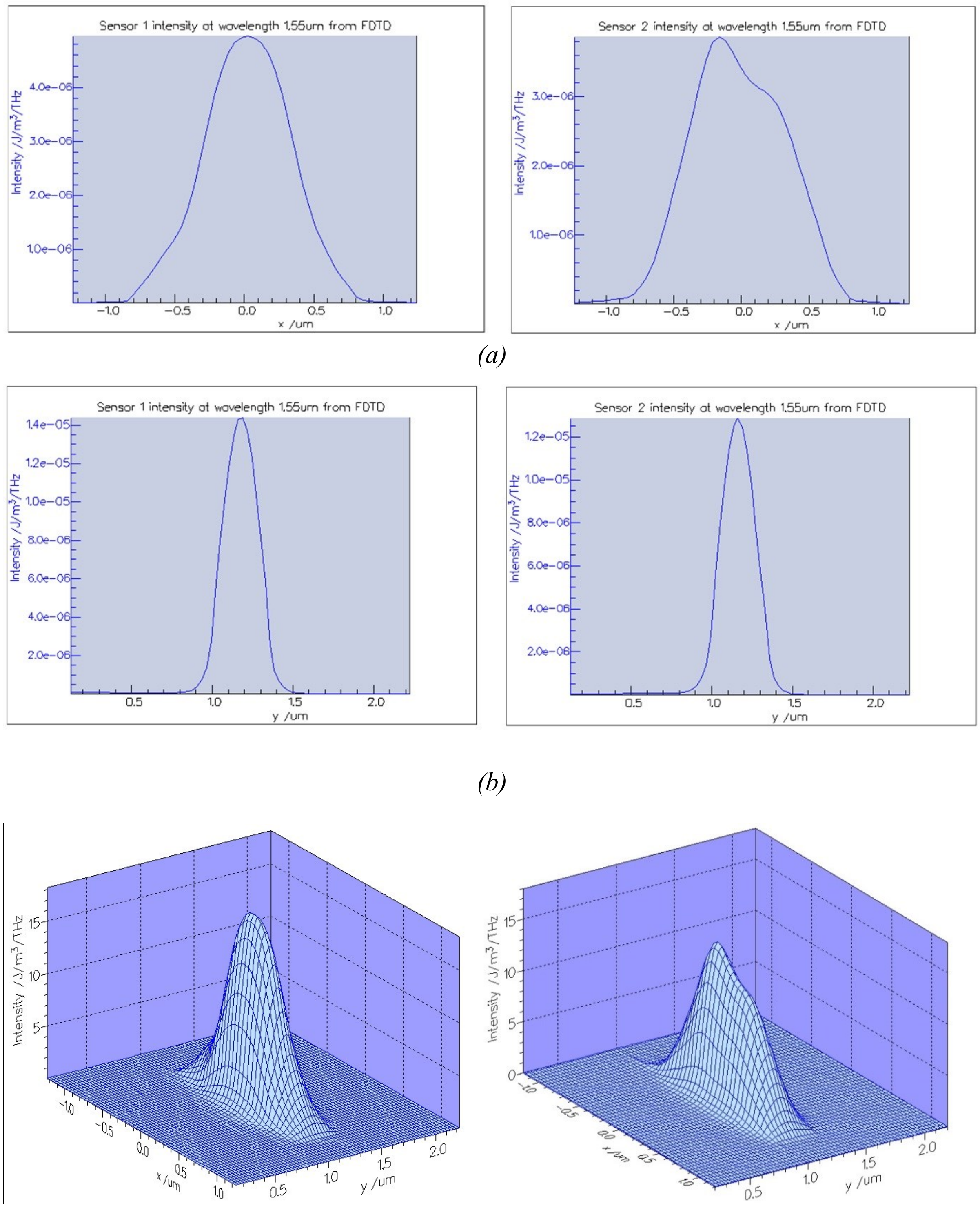

(a)

(b)

(c)

Fig. 4.21. The intensity profile at the input waveguide (left), and at the output waveguide (right) for the two metamaterial lens system from a 3D FDTD simulation, *a*) the cross-section of the field in the x direction, *b*) the cross-section of the field in the y direction, *c*) a perspective plot.

4.5 Summary & Discussion

In this chapter, it has been shown that a planar metamaterial Lüneburg lens can be implemented in an SOI slab waveguide structure by patterning the silicon core with variable sized holes. The subwavelength patterning of binary nanocomposite material to form the metamaterial offers the major advantage of fabrication by a single etch step while demanding feature sizes that can be accessed by deep UV lithography in addition to e-beam lithography. A numerical calibration procedure has been described that is used to find the relation between fill factor and effective refractive index and which improves upon the predictions of analytic effective media theory used by other researchers. The 2D FDTD simulation of a two lens telescope system with waveguide feeds implemented in a metamaterial shown a low insertion loss of -0.45 dB with a reliable field profile at exit. A 3D FDTD simulation of the same two lens telescope system that takes full account of the SOI layers, their finite thickness, and the ridge waveguide feeds also predicts a low loss of -0.83 dB. Less reliance however can be placed on this result due to the coarseness of the computational grid that was necessary. Nevertheless both results are encouraging for planned fabrication trials.

Chapter 5. Conclusions

5.1 Summary & Conclusions

In this thesis, a transparent optical route & select circuit switch architecture has been proposed that consists of a set of switch elements, which steer beams on the basis of the principles of phased array antennas, interconnected by an optical transpose interconnection system. It was further proposed that the switch elements have the structure of generalised Mach-Zehnder interferometers; that the optical transpose interconnects use Lüneburg lenses; and, that the Lüneburg lenses have the structure of a planar metamaterial slab waveguide. By these expedients the complete switch may be fabricated on a single photonic integrated circuit using a suitable integration material platform, such as silicon on insulator, which has been the focus of this work.

The thesis then examines key elements of the overall concept, thereby taking the reader on an intellectual journey to appreciate the beauty of the photonic crystal band structure; the Talbot effect; self-imaging in multimode waveguides; and, the elegance of Fourier, Fresnel and Hamiltonian optics; with a brief a detour on the way to discover some number theory; and all towards a practical engineering goal.

Chapter 1 provided some motivation for the proposed architecture by discussing the anticipated requirements for optical switches in next generation optical communications networks and the relevant state-of-the-art. The subsequent chapters then examined more closely key elements of the overall concept. In Chapter 2 the Talbot effect in free space was discussed and was mapped to the waveguide Talbot effect with a specific emphasis on the determination of the MMI port phase relations. An original contribution is the introduction of Talbot transfer matrices. The nice properties of these transfer matrices facilitate the phase computations in coherent optical applications of MMI structures. In Chapter 3, the behaviour and characteristics of MMI couplers and their role in the GMZI OPA switch elements is explained; the optical transpose interconnection system (OTIS) is introduced and, in an original contribution, adapted to make use of the Lüneburg lens. In Chapter 4 it is explained how a Lüneburg lens may be implemented in a graded 'metamaterial', i.e. a composite material consisting of 'atoms' arranged on a regular lattice suspended in a host material. For parameters accessible to contemporary lithography, it is found that the metamaterial is not accurately described by a simple Maxwell-Garnet mixture formula: a more sophisticated theory is required. Nevertheless, asymmetric slab waveguide theory adequately predicts the effective index of the fundamental mode of a slab waveguide with a metamaterial core, which suggests the metamaterial is behaving similarly to a homogenised continuous medium. An engineering approach to homogenisation is therefore possible which involves the calibration of the effective index of the metamaterial either using a 2D photonic band structure solver with 1D waveguide confinement correction or by a fully 3D photonic band structure solver. This enabled the automation of the layout of metamaterial Lüneburg lenses and telescopes and their verification by 2D and 3D FDTD. Measured insertion losses and crosstalk suggest that a metamaterial implementation results in minimal impairment compared to a continuous medium implementation.

The results established in this thesis together with known results on active phase modulator structure (reviewed in Section 3. 2. 2), establish the feasibility of the overall optical switch concept.

5.2 Discussion & Suggestions for Further Work

The simulation results are encouraging for further work. It is in the nature of research that it can raise more questions than it answers. A selection of these questions follows:

1) A priority is to embark upon fabrication and testing. Indeed, it was hoped that some experimental work could be included in this thesis but the other demands and timescales of a Master’s programme did not permit. Nevertheless, fabrication via the Nano-SOI process funded by CMC has been approved. The Nano-SOI process was originally intended for Nano-Electro-Mechanical System’s (NEMS) research and is not well characterised in respect to standard optical structures (such as grating & edge couplers and waveguides) and proximity effects for features less than 200 *nm* are unknown. A first fabrication run must by necessity involve numerous test structures to permit the calibration of structure-property relations. It is planned to layout the necessary masks in the next period. There are also some photonic integrated circuits in hand or under fabrication at IME, Singapore, funded by CMC which contain active devices in circuits

similar to the GMZI structure. Experiments on these chips will provide data on the active devices that are envisaged to be used in the switch.

2) A second priority is to address the challenge of large scale simulation of nano-photonic systems to accelerate progress. A common recourse in nanophotonics research is to use FDTD as was the case in this thesis. However, FDTD is really only useful for devices with overall dimensions of a few wavelengths. One rapidly meets memory or execution time limitations when attempting to simulate structures with sub-wavelength features with overall dimensions that extend over a large number of wavelengths, such as the Optical Transpose System based upon metamaterial Lüneburg lenses. The problem is exacerbated if 3D FDTD is required. Often only 2D FDTD calculations are viable but extreme care is required to ensure the result is then physically meaningful to the 3D problem at hand. The way forward for this work is to establish confidence in an accurate homogenisation procedure, that allows the larger scale circuits to be accurately simulated using, for example, beam propagation methods designed for continuous media.
3) A third priority is to address the challenge that was found in accommodating the access waveguides around the rim of the micro-Lüneburg lenses of the optical transpose system. These access guides are used to relay the self-image formed by the second MMI of the GMZI structure. This suggests dispensing with these waveguides and merging the second MMI and the micro-Lüneburg lens into a single integrated component. The switch element would then steer beams in angle similar to a Micro-Electro-Mechanical-System (MEMS) mirror but with no moving parts. A line tapered MMI structure (a segment of an annulus) may provide the demagnification sought. The recent application of refractive index engineering to perfect MMI performance [19] suggests that the integrated MMI – micro-Lüneburg lens component as a whole may be implemented as a structured metamaterial.
4) Finally, the sub wavelength crossovers that were introduced in Chapter 1 are perhaps best not considered as a competing technology but as a different manifestation of the use of a metamaterial to guide light between access waveguides of an optical interconnection system. One can envisage a nanostructure which has been engineered to combine the longer range light guidance of the metamaterial Lüneburg lens with the shorter range light guidance of the subwavelength grating waveguide. Advantage might then be taken

of the low loss and cross-talk of free-space crossovers while fine-tuning alignment using the waveguide structures outside of cross-over regions.

Appendix I:
The Fractional Talbot Effect Impulse Response

In Chapter 2 the Talbot Effect Impulse response was found to be given by:

$$h(x,z) = e^{ikz}\frac{1}{\Lambda}\sum_{n=-\infty}^{\infty} e^{i2\pi n\frac{x}{\Lambda}} e^{-i\pi n^2\frac{z}{z_T}}$$

Equation I.1

where:

h is the impulse response;

x is the transverse co-ordinate;

Λ is the transverse period;

z is the longitudinal co-ordinate;

$z_T = \frac{\Lambda^2}{\lambda}$ is the Talbot distance;

n is an integer index;

$k = \frac{2\pi}{\lambda}$ is the wave-number.

In this appendix a closer inspection of the second exponential term within the summation is made when a transverse observation plane intersects the optical axis at rational integer multiples of the Talbot distance. The analysis in this Appendix follows the approach of Berry et al [47].

It is always possible to rearrange the elements of a sequence into a set of sub-sequences, each of length q, and then find the sum of the sequence by summing the subsequence sums:

$$\sum_{n=-\infty}^{\infty} a_n = \sum_{s=0}^{q-1}\sum_{l=-\infty}^{\infty} a_{lq+s}$$

Equation I.2

Application of this strategy to the sum in Equation I.1 yields:

$$h(x,z) = e^{ikz}\frac{1}{\Lambda}\sum_{s=0}^{q-1}\sum_{l=-\infty}^{\infty} e^{i2\pi(lq+s)\frac{x}{\Lambda}} e^{-i\pi(lq+s)^2\frac{z}{z_T}}$$

Equation I.3

Equivalently:

$$h(x,z) = e^{ikz}\frac{1}{\Lambda}\sum_{s=0}^{q-1} e^{i2\pi s\frac{x}{\Lambda}} e^{-i\pi s^2\frac{z}{z_T}} \sum_{l=-\infty}^{\infty} e^{i2\pi lq\frac{x}{\Lambda}} e^{-i\pi\left(l^2 q+2ls\right)q\frac{z}{z_T}}$$

Equation I.4

on moving all terms to the left that do not depend on the index l.

Setting

$$e^{-i2\pi lsq\frac{z}{z_T}}$$

An immediate consequence of placing the observation plane at a rational fractional Talbot distance given by:

$$z = \frac{p}{q} z_T \quad p,q \in \mathbb{Z}$$

Equation I.5

is that the term:

$$e^{-i2\pi lsq\frac{z}{z_T}} = e^{-i2\pi lsp} = 1 \quad \forall\, l,s,p \in \mathbb{Z}$$

Equation I.6

and hence h simplifies to:

$$h(x,z) = e^{ikz}\sum_{s=0}^{q-1} e^{i2\pi s\frac{x}{\Lambda}} e^{-i\pi s^2\frac{p}{q}} \frac{1}{\Lambda}\sum_{l=-\infty}^{\infty} e^{i2\pi lq\frac{x}{\Lambda}} e^{-i\pi l^2 qp}$$

Equation I.7

Consider the final exponential in Equation I.7:

$$e^{-i\pi l^2 qp} = (-1)^{l^2 qp}$$

Equation I.8

Now:

$$\begin{aligned} (-1)^{l^2 qp} &= 1 && q\ or\ p\ even \\ (-1)^{l^2 qp} &= (-1)^{l} && q\ and\ p\ odd \end{aligned}$$

Equation I.

where a remarkable fact, verging on a coincidence, that:

$$(-1)^{l^2} = [(-1)^l]^l = (-1)^l \quad l \in \mathbb{Z}$$

Equation I.10

permits the replacement of the quadratic exponent in Equation I.9 by a linear exponent.

Hence, the second summation in Equation I.7 takes the following forms:

$$\frac{1}{\Lambda}\sum_{l=-\infty}^{\infty} e^{i2\pi lq\frac{x}{\Lambda}} e^{-i\pi l^2 qp} = \frac{1}{\Lambda}\sum_{l=-\infty}^{\infty} e^{i2\pi lq\frac{x}{\Lambda}} = \frac{1}{q}\sum_{m=-\infty}^{\infty} \delta\left(x - m\frac{\Lambda}{q}\right) \qquad q\ or\ p\ even$$

$$\frac{1}{\Lambda}\sum_{l=-\infty}^{\infty} e^{i2\pi lq\frac{x}{\Lambda}} e^{-i\pi l^2 qp} = \frac{1}{\Lambda}\sum_{l=-\infty}^{\infty} e^{i2\pi lq\left(\frac{x}{\Lambda}-\frac{1}{2}\right)} = \frac{1}{q}\sum_{m=-\infty}^{\infty} \delta\left(x - \left(m + \frac{1}{2}q\right)\frac{\Lambda}{q}\right) \qquad q\ and\ p\ odd$$

Equation I.11

The pre-factor to these comb distributions is sampled by the singular support of the combs. Interchanging the sum over m and q and performing this sampling, yields:

$$h(x,z) = e^{ikz}\sum_{m=-\infty}^{\infty} \frac{1}{\sqrt{q}}\left[\frac{1}{\sqrt{q}}\sum_{s=0}^{q-1} e^{i2\pi s\frac{m}{q}} e^{-i\pi s^2\frac{p}{q}}\right]\delta\left(x - m\frac{\Lambda}{q}\right) \qquad q\ or\ p\ even$$

Equation I.12

$$h(x,z) = e^{ikz}\sum_{m=-\infty}^{\infty} \frac{1}{\sqrt{q}}\left[\frac{1}{\sqrt{q}}\sum_{s=0}^{q-1} e^{i2\pi s\left(m+\frac{1}{2}q\right)\frac{1}{q}} e^{-i\pi s^2\frac{p}{q}}\right]\delta\left(x - \left(m + \frac{1}{2}q\right)\frac{\Lambda}{q}\right) \qquad q\ and\ p\ odd$$

Equation I.13

For relatively prime integer p and q , Equation I.12 and Equation I.13 show that, q multiple images of the initial field are formed that are spaced in the transverse plane by Λ/q .To satisfy energy conservation the overall amplitude of the images is reduced by a factor of $1/\sqrt{q}$. When p and q are odd the multiple images are additionally shifted by one half-period $\Lambda/2$ (i.e. has no dependence on q). However, the Dirac distributions that are shifted are indistinguishable from each other and the Talbot phase associated to any Dirac distribution is determined only by the location of its singular support. A Dirac distribution is shifted to a location midway between two locations previously occupied by a Dirac distribution. Consequently, the shift is equivalent to half a lattice pitch $(1/2)(\Lambda/\mathrm{q})$. To see this write: $\acute{m} = m + \lfloor q/2 \rfloor$. The infinite sum over m may be written as an infinite sum over

$\acute{m}$ and the accent may then be dropped. This suggests defining a lattice with a pitch of $\Lambda/2\mathrm{q}$ with the Dirac distributions occupying the even sites for p or q even and the odd sites for p and q odd.

In simpler terms:

$$h(x,z) = e^{ikz} \sum_{m=-\infty}^{\infty} \frac{1}{q^{1/2}} g(2m)\delta\left(x - (2m)\frac{\Lambda}{2q}\right) \qquad q\ or\ p\ even$$
$$h(x,z) = e^{ikz} \sum_{m=-\infty}^{\infty} \frac{1}{q^{1/2}} g(2m+1)\delta\left(x - (2m+1)\frac{\Lambda}{2q}\right) \quad q\ and\ p\ odd$$

Equation I.14

where:

$$g(n) = \frac{1}{q^{1/2}} \sum_{s=0}^{q-1} e^{i\frac{\pi}{q}(ns - ps^2)}$$

Equation I.15

The coefficients $g(n)$ are pure phase factors. To show this first note:

$$\sum_{t=0}^{q-1} z^{dt} = \frac{1-(z^d)^q}{1-(z^d)} = \frac{1-(z^q)^d}{1-(z^d)} = 0 \qquad if\ \ z^d \neq 1\ \&\ z^q = 1$$
$$= q \qquad\qquad if\ \ z^d = 1\ \ (e.g. d = 0)$$

Equation I.16

Now:

$$|g(n)|^2 = \frac{1}{q} \sum_{s,t=0}^{q-1} e^{i\frac{\pi}{q}[n(s-t) - p(s^2-t^2)]} = \frac{1}{q} \sum_{s,t=0}^{q-1} e^{i\frac{\pi}{q}[n(s-t) - p(s-t)(s+t)]}$$
$$= \frac{1}{q} \sum_{d=0}^{q-1} \sum_{t=0}^{q-1} e^{i\frac{\pi}{q}[nd - pd(d+2t)]} = \frac{1}{q} \sum_{d=0}^{q-1} e^{i\frac{\pi}{q}[nd - pd^2]} \sum_{t=0}^{q-1} e^{-i\frac{2\pi}{q}pdt} = 1$$

Equation I.17

I.1 To Evaluate the Talbot Phase for n Even

$$g(n) = \frac{1}{q^{1/2}} \sum_{s=0}^{q-1} e^{i\frac{\pi}{q}[ns - ps^2]}$$

Equation I.18

$$g(n) = \frac{1}{q^{1/2}} \sum_{s=0}^{q-1} e^{i\frac{\pi p}{q}(p\backslash q)^2\left(\frac{n}{2}\right)^2} e^{-i\frac{\pi p}{q}\left(s-(p\backslash q)\frac{n}{2}\right)^2} \qquad (p \setminus q)p = 1\ mod\ q$$

$$g(n) = e^{i\frac{\pi p}{q}(p\backslash q)^2\left(\frac{n}{2}\right)^2} \frac{1}{q^{1/2}} \sum_{s=0}^{q-1} e^{-i\frac{\pi p}{q}s^2}$$

$$g(n) = g(0)\, e^{i\frac{\pi p(p\backslash q)^2}{q}\left(\frac{n}{2}\right)^2}$$

$$g(0) = \frac{1}{q^{1/2}} \sum_{s=0}^{q-1} e^{-i\frac{p\pi}{q}s^2} \qquad \text{Gauss Quadratic Sum}$$

Equation I.19

Note $(p \setminus q)$ only exists if $gcd(p, q) = 1$ i.e. q and p are relatively prime. n is even only when $q\ or\ p$ is even. It is then necessary that q and p are of opposite parity avoid a common factor of 2. n is odd only when q and p are odd.

I.2 To Evaluate the Talbot Phase for n Odd

First note that setting:

$$w(s) = \mathrm{e}^{i\frac{\pi}{q}(ns-ps^2)}$$

Equation I.20

then:

$$w(s+q) = e^{i\frac{\pi}{q}(n(s+q)-p(s+q)^2)}$$
$$w(s+q) = e^{i\frac{\pi}{q}(ns+nq-ps^2-2psq+pq^2)}$$
$$= w(s)e^{-i2\pi ps}\, e^{i\pi(n-pq)}$$
$$= w(s)e^{i\pi(n-pq)}$$

Equation I.21

It has been established that n is odd only if p & q are odd. Hence $(n - pq)$ is always even and $w(s)$ is periodic in s with period q.

Now:

$$\sum_{s=0}^{q-1} w(rs) = \sum_{s=0}^{q-1} w(s) \quad r \in \mathbb{Z} \quad gcd(q, r) = 1$$

Equation I.22

This follows because $\{rs\}\ mod\ q$ goes through all the elements of $\{s\}\ mod\ q$ in some different order.

Since q is odd, it is convenient to take $r = 2$.

$$g(n) = \frac{1}{q^{1/2}} \sum_{s=0}^{q-1} e^{i\frac{\pi}{q}[2ns-2ps^2]}$$

$$g(n) = \frac{1}{q^{1/2}} \sum_{s=0}^{q-1} e^{i\frac{\pi 4\mathrm{p}}{q}((4p\backslash q)n)^2} e^{-i\frac{\pi 4p}{q}(s-(4p\backslash q)n)^2}$$

$$g(n) = e^{i\frac{\pi 4p(4p\backslash q)^2}{q}n^2} \frac{1}{q^{1/2}} \sum_{s=0}^{q-1} e^{-i\frac{\pi p}{q}(2s)^2}$$

$$g(n) = g(0) e^{i\frac{\pi 4p(4p\backslash q)^2}{q}n^2}$$

$$g(0) = \frac{1}{q^{1/2}} \sum_{s=0}^{q-1} e^{-i\frac{\pi p}{q}s^2} \qquad \text{Gauss Quadratic Sum}$$

Equation I.24

In summary, it has been established that the Talbot phase factor may be written:

$$g(n; p, q) = g(0; p, q) exp[i\theta(n; p, q)]$$

Equation I.25

$$\theta(n; p, q) = p(p \setminus q)^2 \left(\frac{n}{2}\right)^2 \frac{\pi}{q} \quad n\ even$$

$$\theta(n; p, q) = 4p(4p \setminus q)^2 n^2 \frac{\pi}{q} \quad n\ odd$$

Equation I.26

The Talbot phase factor is periodic in n with integer period $2q$ reflecting the transverse period Λ of the field. It is also periodic in p with integer period $2q$ reflecting the longitudinal period $2z_T$ of the field. $g(0; p, q)$ is the Gauss Quadratic Sum of analytic number theory [48].

Appendix II:
General Properties of Scattering Matrices

II.1 Fundamental Symmetry Properties

Consider a passive structure illuminated by an indexed collection of inward propagating modes each with overall amplitude a_j, which are scattered into a collection of outward propagating modes each with overall amplitude b_i. By time reversal symmetry, to every inward propagating wave there is an associated outward propagating wave which is a time reversed replica of the inward propagating wave, and vice versa. The modal fields are normalised such that the total power of an inward propagating mode is $|a_j|^2$and an outward propagating mode is $|b_j|^2$. The amplitudes corresponding to a mode and its time reversed partner share the same index. The amplitudes may be thought of as the input (inward propagating wave) and output (outward propagating wave) of ‘ports’ to an optical system. The problem is linear and so the amplitudes are related by a scattering matrix:

$$\boldsymbol{b} = \boldsymbol{U}\boldsymbol{a}$$
$$\boldsymbol{a} = \begin{bmatrix} a_1 \\ \vdots \\ a_n \end{bmatrix}$$
$$\boldsymbol{b} = \begin{bmatrix} b_1 \\ \vdots \\ b_n \end{bmatrix}$$
$$\boldsymbol{U} = \begin{bmatrix} c_{11} & \cdots & c_{1n} \\ \vdots & \ddots & \vdots \\ c_{n1} & \cdots & c_{nn} \end{bmatrix}$$

Equation II.1

If the system is lossless, i.e. all mode pairs excited have been included and there is no absorption, then the scattering matrix is *unitary*:

$$\|\boldsymbol{b}\|^2 = \|\boldsymbol{a}\|^2$$
$$\Longrightarrow$$
$$(\boldsymbol{b}, \boldsymbol{b}) = (\boldsymbol{U}^{\dagger}\boldsymbol{U}\boldsymbol{a}, \boldsymbol{a}) = (\boldsymbol{a}, \boldsymbol{a})$$
$$\Longrightarrow$$
$$\boldsymbol{U}^{\dagger}\boldsymbol{U} = \boldsymbol{I}$$

Equation II.2

Electromagnetic scattering is generally reciprocal (e.g. the radiation pattern of an antenna is the same whether it is used in transmission or reception). Hence, if inward propagating mode j has amplitude a_j and results in outward propagating mode i having amplitude b_i, then outward propagating mode j will have an amplitude of b_i if inward propagating mode i has an amplitude a_j. That is the scattering matrix is *symmetric*.

$$\begin{gathered} c_{ij} = c_{ji} \\ \Longrightarrow \\ \boldsymbol{U} = \boldsymbol{U^T} \end{gathered}$$

Equation II.3

Note:

$$\begin{gathered} \boldsymbol{b} = \boldsymbol{Ua} \\ \Longrightarrow \\ \boldsymbol{a} = \boldsymbol{U^{-1}b} = \boldsymbol{U^{\dagger}b} = (\boldsymbol{U^T})^{*}\boldsymbol{b} = \boldsymbol{U}^{*}\boldsymbol{b} \\ \Longrightarrow \\ \boldsymbol{a}^{*} = \boldsymbol{Ub}^{*} \end{gathered}$$

Equation II.4

That is, if a system with inward propagating wave amplitudes $\boldsymbol{a}$ gives rise to outward propagating wave amplitudes $\boldsymbol{b}$, then setting the inward propagating amplitudes to $\boldsymbol{b}^*$ gives rise to outward propagating waves of amplitudes $\boldsymbol{a}^*$**.** In other words, a wave that is a phase conjugated wave retraces its path through the same linear lossless optical system (i.e. *time reversal symmetry*).

Now suppose some ports of the system are partitioned into two disjoint sets (it is convenient but not necessary that they contain the same number of elements) which may be considered as a set of ports on the left and a set of ports on the right. Then the scattering matrix partitions in the same way:

$$\begin{bmatrix} \boldsymbol{b}_l \\ \boldsymbol{b}_r \end{bmatrix} = \begin{bmatrix} \boldsymbol{U_{ll}} & \boldsymbol{U_{lr}} \\ \boldsymbol{U_{rl}} & \boldsymbol{U_{rr}} \end{bmatrix} \begin{bmatrix} \boldsymbol{a}_l \\ \boldsymbol{a}_r \end{bmatrix}$$

Equation II.5

That is:

$\boldsymbol{U_{ll}}$ describes the back scattering of inward propagating waves at the ports on the left to outward propagating waves at the ports on the left;

$\boldsymbol{U_{lr}}$ describes the forward scattering of inward propagating waves at ports on the right to outward going waves at ports on the left;

$\boldsymbol{U_{rl}}$ describes the forward scattering of inward propagating waves at the ports on the left to outward going waves at the ports on the right;

$\boldsymbol{U_{rr}}$ describes the back scattering of inward propagating waves at the ports on the right to outward going waves at the ports on the right;

This partition makes most sense for the reduced problem when the back-scattering is negligible by design:

$$\begin{gathered}\boldsymbol{U_{ll}} \sim \boldsymbol{0}\\ \boldsymbol{U_{rr}} \sim \boldsymbol{0}\\ \Longrightarrow\\ \boldsymbol{b}_l = \boldsymbol{U_{lr}}\boldsymbol{a}_r\\ \boldsymbol{b}_r = \boldsymbol{U_{rl}}\boldsymbol{a}_l\end{gathered}$$

Equation II.6

Under the assumption of negligible back-scatter, $\boldsymbol{U_{lr}}$, $\boldsymbol{U_{rl}}$ inherit from $\boldsymbol{U}$ the following properties:

$$\begin{gathered}\boldsymbol{U_{lr}^{\dagger}}\boldsymbol{U_{lr}} = \boldsymbol{I}\\ \boldsymbol{U_{rl}^{\dagger}}\boldsymbol{U_{rl}} = \boldsymbol{I}\\ \boldsymbol{U_{rl}} = \boldsymbol{U_{lr}^{T}}\end{gathered}$$

Equation II.7

Equivalently:

$$\begin{gathered}\boldsymbol{b}_r = \boldsymbol{U_{rl}}\boldsymbol{a_l}\\ \boldsymbol{b}_r = \boldsymbol{U_{lr}^{T}}\boldsymbol{a_l}\\ \Longrightarrow\\ \boldsymbol{b}_r^{*} = \boldsymbol{U_{lr}^{\dagger}}\boldsymbol{a_l^{*}}\end{gathered}$$

Equation II.8

Hence:

$$\begin{gathered}\boldsymbol{a_r} = \boldsymbol{b}_r^{*}\\ \Longrightarrow\\ \boldsymbol{b_l} = \boldsymbol{a_l^{*}}\end{gathered}$$

Equation II.9

That is, the conjugate of the exit wave back-propagates through the system to emerge as the conjugate of the entrance wave.

The most important conclusion is that the transfer matrix for the reduced problem is unitary but not necessarily symmetric.

II.2 Geometrical Symmetry

A common symmetry of the system is that it is reversible. That is:

$$\begin{gathered} \boldsymbol{a_r} = \boldsymbol{a_l} \\ \Longrightarrow \\ \boldsymbol{b_r} = \boldsymbol{b_l} \end{gathered}$$

Equation II.10

but since:

$$\begin{gathered} \boldsymbol{b}_r = \boldsymbol{U_{rl}} \boldsymbol{a}_l \\ \boldsymbol{b}_l = \boldsymbol{U_{rl}^T} \boldsymbol{a_r} \end{gathered}$$

Equation II.11

this implies:

$$\begin{gathered} \boldsymbol{U_{rl}^T} = \boldsymbol{U_{rl}} \\ \boldsymbol{U_{lr}^T} = \boldsymbol{U_{lr}} \end{gathered}$$

Equation II.12

i.e. , the transfer matrix is symmetric.

Another common symmetry is a 180° rotation that inverts the order of the ports and reverses the system. That is:

$$\begin{gathered} \boldsymbol{a_l} \longrightarrow \boldsymbol{J a_r} \\ \Longrightarrow \\ \boldsymbol{b_r} \longrightarrow \boldsymbol{J b_l} \\ \Longrightarrow \\ \boldsymbol{U_{rl}} = \boldsymbol{J U_{rl}^T J} \end{gathered}$$

Equation II.13

where $\boldsymbol{J}$ is the exchange matrix with unit entries in its trailing diagonal.

The transfer matrix is then persymmetric, i.e. it is symmetric across the trailing diagonal.

II.3 Examples

2×2 MMI

Unitary

$$\boldsymbol{U} = \begin{bmatrix} a & b \\ -b^* & a^* \end{bmatrix}$$
$$|a|^2 + |b|^2 = 1$$

Equation II.14

Symmetric:

$$b = -b^*$$
$$\Longrightarrow$$
$$arg(b) = \pm\frac{\pi}{2}$$

Equation II.15

Persymmetric:

$$a = a^*$$
$$\Longrightarrow$$
$$arg(a) = 0$$

Equation II.16

Equal splitting ratio:

$$|a| = |b|$$
$$\Longrightarrow$$
$$|a| = \frac{1}{\sqrt{2}}$$
$$|b| = \frac{1}{\sqrt{2}}$$

Equation II.17

Hence:

$$\boldsymbol{U} = \frac{1}{\sqrt{2}}\begin{bmatrix} 1 & \pm i \\ \pm i & 1 \end{bmatrix}$$

Equation II.18

Used as a splitter with a single input there is a $\pi/2$ phase difference between the output ports.

2×1 y-branch

The two inputs combine to create two modes at the junction – the symmetric mode and the anti-symmetric mode. This may be described by a 2×2 matrix:

$$\boldsymbol{U} = \begin{bmatrix} a & b \\ -b^* & a^* \end{bmatrix}$$
$$|a|^2 + |b|^2 = 1$$

Equation II.19

Perfectly symmetric input zeros the anti-symmetric mode and perfectly anti-symmetric input zeros the symmetric mode:

$$a^* - b^* = 0$$
$$\Longrightarrow$$
$$a = b$$

$$a - b = 0$$
$$\Longrightarrow$$
$$a = b$$

Equation II.20

which implies:

$$|a| = |b|$$
$$\Longrightarrow$$
$$|a| = \frac{1}{\sqrt{2}}$$
$$|b| = \frac{1}{\sqrt{2}}$$

Equation II.21

Hence:

$$\boldsymbol{U} = \frac{1}{\sqrt{2}} \begin{bmatrix} e^{i\theta} & e^{i\theta} \\ -e^{-i\theta} & e^{-i\theta} \end{bmatrix}$$

Equation II.22

The y-join discards the anti-symmetric mode at the output and hence does not use the bottom row in $\boldsymbol{U}$**.** As a y-fork, one must consider the transpose:

$$\boldsymbol{U}^{\boldsymbol{T}} = \frac{1}{\sqrt{2}} \begin{bmatrix} e^{i\theta} & -e^{-i\theta} \\ e^{i\theta} & e^{-i\theta} \end{bmatrix}$$

Equation II.23

The y-fork does not excite the anti-symmetric mode and therefore the last column is unused.

The two output ports therefore have the same phase.

Appendix III:
Hamiltonian Optics of the Lüneburg Lens

In this Appendix, Hamilton's method [84] is applied to the ray analysis of the Lüneburg Lens. The Hamiltonian function depends upon both position $\boldsymbol{q}$ and momentum $\boldsymbol{p}$ co-ordinates and is a root of the dispersion relation that governs the propagation of plane electromagnetic waves in a medium with a uniform refractive index equal to the local value of the spatially varying refractive index $n(\boldsymbol{q})$. The advantage of the method is the ease by which it may be adapted to spatially dispersive constitutive relations [85,86], e.g. a refractive index that depends locally upon both position and momentum (wave-vector) co-ordinates that can arise from the homogenisation of the optical properties of a nanostructured material.

Hamilton's equations for the ray trajectories are:

$$\frac{d\boldsymbol{q}}{dt} = \frac{\partial H}{\partial \boldsymbol{p}}$$
$$\frac{d\boldsymbol{p}}{dt} = -\frac{\partial H}{\partial \boldsymbol{q}}$$

Equation III.1

with a Hamiltonian function given by:

$$H(\boldsymbol{q},\boldsymbol{p}) = \frac{1}{2}[\boldsymbol{p}.\boldsymbol{p} - n^2(\boldsymbol{q})]$$

Equation III.2

The Lüneburg lens has a refractive index profile n defined by:

$$n(\boldsymbol{q}) \quad = \begin{cases} n_0\sqrt{2-(\boldsymbol{q}.\boldsymbol{q}/a^2)} & |\boldsymbol{q}| \leq a \\ n_0 & |\boldsymbol{q}| > a \end{cases}$$

Equation III.3

where a is the radius of the lens and n_0 is the ambient refractive index.

Substitution of Equation III.3 into Equation III.2 and then substituting the result into Equation III.1, leads to the dynamical system:

$$\frac{d\boldsymbol{q}}{dt} = \boldsymbol{p}$$
$$\frac{d\boldsymbol{p}}{dt} \quad = \begin{cases} -\kappa^2\boldsymbol{q} & |\boldsymbol{q}| \leq a \\ 0 & |\boldsymbol{q}| > a \end{cases}$$

Equation III.3

where:

$$\kappa = \frac{n_0}{a}$$

Equation III.4

The ray consequently executes simple harmonic motion (SHM) in the interior of the lens.

$$\frac{d^2\boldsymbol{q}}{dt^2} + \kappa^2\boldsymbol{q} = 0$$

Equation III.5

The SHM equation admits any linear combination of $sin(\kappa t)$ and $cos(\kappa t)$ as its solution.

In the exterior the rays are straight line segments.

With the initial condition specified by the impact parameters:

$$\boldsymbol{q}(0) = (0, 0, -a)$$
$$\boldsymbol{p}(0) = \left(n_0 sin(\theta), 0, n_0 cos(\theta)\right)$$

Equation III.6

the solution to Equation III.5 is:

$$q_1(t) = a\ sin(\theta)sin(\kappa t)$$

$$q_3(t) = a\ cos(\theta)sin(\kappa t) - a\ cos(\kappa t)$$

$$p_1(t) = n_0\ sin(\theta)\ cos(\kappa t)$$
$$p_3(t) = n_0 cos(\theta)cos(\kappa t) + n_0 sin(\kappa t)$$

Equation III.7

By direct substitution:

$$\boldsymbol{q} \cdot \boldsymbol{q} = a^2[1 - cos(\theta)sin(2\kappa t)]$$

Equation III.8

As a consequence, the closest approach of the ray to the centre of the lens is attained when $\kappa t = (\pi/4)$:

$$|\boldsymbol{q}|_{\boldsymbol{min}} = a\sqrt{1 - cos(\theta)}$$

Equation III.9

The ray escapes the lens $\boldsymbol{q}\cdot\boldsymbol{q} > \mathrm{a}$ when $\kappa\mathrm{t} = (\pi/2)$ and the exit position and momentum are:

$$q_1 = a\,sin(\theta)$$

$$q_3 = a\,cos(\theta)$$

$$p_1 = 0$$

$$p_3 = n_0$$

Equation III.10

The variable t has no particular special meaning; it merely parameterises the rays. The optical path length along a ray can be obtained:

$$\tau(t_2) - \tau(t_1) = \int_{\boldsymbol{t_1}}^{\boldsymbol{t_2}} n^2 \circ \boldsymbol{q}(\mathrm{t})\,dt$$

Equation III.11

Hence:

$$\tau(t) = \int_0^t \left(2n_0^2 - \frac{n_0^2}{a^2}\boldsymbol{q}.\boldsymbol{q}\right) dt$$

$$\tau(t) = n_0^2\left(t + \frac{1}{2k}cos(\theta)\big(1 - cos(2kt)\big)\right)$$

Equation III.12

and on escape $\kappa t = (\pi/2)$ one obtains:

$$\tau = n_0 a\left(\frac{\pi}{2} + cos(\theta)\right)$$

Equation III.13

For $\theta = 0$ the optical path length is obtained for the un-deviated ray passing through the centre of the lens.

$$\tau = n_0 a\left(\frac{\pi}{2} + 1\right)$$

Equation III.14

Since the ray escapes at $\boldsymbol{q} = a\big(sin(\theta), 0, cos(\theta)\big)$ with a momentum of $\boldsymbol{p} = (0,0,\ n_0)$, propagation to the $q_3 = a$ plane adds an optical path length of:

$$\tau = n_0 a\big(1 - cos(\theta)\big)$$

Equation III.15

Hence the total optical path length from the initial point $\boldsymbol{q_i} = (0, 0, -a)$ to the final point $\boldsymbol{q_f} = a(sin(\theta), 0, -1)$ is equal to:

$$\tau\left(\boldsymbol{q_f}\right) - \tau(\boldsymbol{q_i}) = n_0 a\left(\frac{\pi}{2} + cos(\theta)\right) + n_0 a\big(1 - cos(\theta)\big) = \tau = n_0 a\left(\frac{\pi}{2} + 1\right)$$

Equation III.16

which is a constant independent of θ that agrees with the on-axis result of Equation III.14.

The Lüneburg lens thus transforms a spherical wave from a point source on its rim to a plane wave with wave-fronts orthogonal to the optical axis formed by a line passing though the point source and the centre of the lens. Since the Lüneburg lens is spherically symmetric about its centre, all other ray trajectories are obtained by a rotation of the plane of incidence about the centre of the lens.

Appendix IV:
Modes of the Asymmetric Slab Waveguide

The fields in the upper cladding, core, and lower cladding regions must satisfy the wave equation for a medium with the respective refractive index. For a Cartesian co-ordinate system the solutions are plane waves with wave-vectors of the magnitude appropriate to the local refractive index. The boundary conditions ensure that the longitudinal variation of the field with propagation is the same in all three regions. Bound modes then correspond to a superposition of two plane waves with equal and opposite transverse components in the core region with exponentially decaying tails in the cladding region. In the case of symmetric slabs, the modes may be partitioned into symmetric and anti-symmetric classes characterised by cos-like and sin-like variation of the field in the core region about its central plane and exponential decay with identical decay constants in the upper and lower cladding. The boundary conditions enforce continuity of the field across the boundary and continuity of the transverse derivative (TE) or continuity of the transverse derivative weighted by the inverse of the local squared refractive index (TM).

For an asymmetric slab, the decay constants in the cladding are no longer equal and the field in the core is no longer either cos- or sin- like but a linear superposition of the two. This is equivalent to a shift. The higher index cladding will have a smaller decay constant than the lower index cladding. One therefore expects the mode to be pulled towards the higher index of the upper of lower cladding so satisfy the boundary conditions. One also notes that:

$$cos(\phi - \xi_c) = sin(\phi - \xi_s)$$
$$\xi_c = \frac{\pi}{2} + \xi_s$$

Equation IV.1

Hence even in the symmetric case the anti-symmetric solutions may be constructed using a transverse phase shift to the field in the core. This fact will be used to construct all solutions for the asymmetric guide using a cos-like field with a shift in the core. Then subsequently partition the solutions into cos-like and sin-like field with a shift in the core such that they smoothly map into the symmetric and anti-symmetric solutions of the symmetric slab-waveguide as an asymmetry parameter approaches zero.

Let:

n_e	be the effective index of the mode;
n_{cov}	be the refractive index of the upper cladding ($n_{air} = 1$);
n_{cor}	be the refractive index of the core ($n_{Si} = 3.47772$);
n_{sub}	be the refractive index of the lower cladding ($n_{SiO_2} = 1.44402$);
$k_0 = \frac{2\pi}{\lambda_0}$	be the vacuum wave-number;
λ_0	be the vacuum wavelength;
d	be one half of the core thickness;
$\beta = n_e k_0$	be the longitudinal propagation constant where n_e is the effective index;
γ	be the decay constant of the mode in the cladding;
κ	be the transverse wave-number in the core;
φ	be the field;
x	be the transverse co-ordinate.

Then the field in each region is given by:

Upper Cladding

$$\varphi(x) = cos(\kappa d - \xi)exp(\gamma_{cov} d)exp(-\gamma_{cov} x) \quad d \leq x < \infty$$
$$n_{cov}^2 k_0^2 = \beta^2 - \gamma_{cov}^2$$

Equation IV.2

Core

$$\varphi(x) = cos(\kappa x - \xi) \quad -d \leq x \leq d$$
$$n_{cor}^2 k_0^2 = \beta^2 + \kappa^2$$

Equation IV.3

Lower Cladding

$$\varphi(x) = cos(-\kappa d - \xi)exp(\gamma_{sub} d)exp(\gamma_{sub} x) \quad -\infty \leq x \leq -d$$
$$n_{sub}^2 k_0^2 = \beta^2 - \gamma_{sub}^2$$

Equation IV.4

To satisfy the boundary conditions:

Continuity of derivative (TE)

$$\gamma_{cov} cos(\kappa d - \xi) = \kappa sin(\kappa d - \xi)$$
$$\gamma_{sub} cos(-\kappa d - \xi) = -\kappa sin(-\kappa d - \xi)$$
$$\Longrightarrow$$
$$tan(\kappa d - \xi) = \frac{\gamma_{cov} d}{\kappa d}$$
$$tan(\kappa d + \xi) = \frac{\gamma_{sub} d}{\kappa d}$$

Equation IV.5

Hence:

$$\kappa d - \xi = p\pi + tan^{-1}\left(\frac{\gamma_{cov} d}{\kappa d}\right)$$
$$\kappa d + \xi = q\pi + tan^{-1}\left(\frac{\gamma_{sub} d}{\kappa d}\right)$$
$$\Longrightarrow$$
$$\kappa d = (p+q)\frac{\pi}{2} + \frac{1}{2}tan^{-1}\left(\frac{\gamma_{cov} d}{\kappa d}\right) + \frac{1}{2}tan^{-1}\left(\frac{\gamma_{sub} d}{\kappa d}\right)$$
$$\xi = (p-q)\frac{\pi}{2} + \frac{1}{2}tan^{-1}\left(\frac{\gamma_{cov} d}{\kappa d}\right) - \frac{1}{2}tan^{-1}\left(\frac{\gamma_{sub} d}{\kappa d}\right)$$

Equation IV.6

where p and q are integers.

Two cases may be distinguished:

1. $p - q = is\ even\ \Longrightarrow m = p + q\ is\ even$
2. $p - q = is\ odd\ \Longrightarrow m = p + q\ is\ odd$

It is noted that the field distributions are equivalent (cos-like) for $p - q$ equal to any even number up to an overall sign which may be absorbed into the field normalisation. They are also equivalent (sin-like) for $p - q$ equal to any odd number

All solutions are therefore exhausted by setting:

$$p + q = m$$
$$p - q = 0 \quad m\ even$$
$$p - q = 1 \quad m\ odd$$

1. m even core field representation $cos(\kappa x - \xi)$
2. m odd, core field representation $sin(\kappa x - \xi)$

$$\boxed{\begin{aligned} \kappa d &= m\frac{\pi}{2} + \frac{1}{2}tan^{-1}\left(\frac{\gamma_{cov} d}{\kappa d}\right) + \frac{1}{2}tan^{-1}\left(\frac{\gamma_{sub} d}{\kappa d}\right) \\ \xi &= \frac{1}{2}tan^{-1}\left(\frac{\gamma_{cov} d}{\kappa d}\right) - \frac{1}{2}tan^{-1}\left(\frac{\gamma_{sub} d}{\kappa d}\right) \end{aligned}}$$

Equation IV.7

Continuity of derivative (TM)

$$\frac{1}{n_{cov}^2}\gamma_{cov}cos(\kappa d-\xi)=\frac{1}{n_{cor}^2}\kappa sin(\kappa d-\xi)$$
$$\frac{1}{n_{sub}^2}\gamma_{sub}cos(-\kappa d-\xi)=-\frac{1}{n_{cor}^2}\kappa sin(-\kappa d-\xi)$$
$$\Rightarrow$$
$$tan(\kappa d-\xi)=\frac{n_{cor}^2}{n_{cov}^2}\frac{\gamma_{cov}d}{\kappa d}$$
$$tan(\kappa d+\xi)=\frac{n_{cor}^2}{n_{sub}^2}\frac{\gamma_{sub}d}{\kappa d}$$

Equation IV.8

Hence:

1. m even core field representation $cos(\kappa x-\xi)$
2. m odd, core field representation $sin(\kappa x-\xi)$

$$\kappa d=m\frac{\pi}{2}+\frac{1}{2}tan^{-1}\left(\frac{n_{cor}^2}{n_{cov}^2}\frac{\gamma_{cov}d}{\kappa d}\right)+\frac{1}{2}tan^{-1}\left(\frac{n_{cor}^2}{n_{sub}^2}\frac{\gamma_{sub}d}{\kappa d}\right)$$
$$\xi=\frac{1}{2}tan^{-1}\left(\frac{n_{cor}^2}{n_{cov}^2}\frac{\gamma_{cov}d}{\kappa d}\right)-\frac{1}{2}tan^{-1}\left(\frac{n_{cor}^2}{n_{sub}^2}\frac{\gamma_{sub}d}{\kappa d}\right)$$

Equation IV.9

Additional Constraints

$$n_{cov}^2k_0^2=\beta^2-\gamma_{cov}^2$$

Equation IV.10

$$n_{cor}^2k_0^2=\beta^2+\kappa^2$$

Equation IV.11

$$n_{sub}^2k_0^2=\beta^2-\gamma_{sub}^2$$

Equation IV.12

Hence:

$$k_0^2(n_{cor}^2-n_{cov}^2)=\kappa^2+\gamma_{cov}^2$$

Equation IV.13

$$k_0^2\left(n_{cor}^2-n_{sub}^2\right)=\kappa^2+\gamma_{sub}^2$$

Equation IV.14

The asymmetry has introduced two normalised frequency parameters, one associated to the core-cover interface and the other associated to the core-substrate

$$\nu_{cov} = k_0 d(n_{cor}^2 - n_{cov}^2)^{\frac{1}{2}}$$

Equation IV.15

$$\nu_{sub} = k_0 d\left(n_{cor}^2 - n_{sub}^2\right)^{\frac{1}{2}}$$

Equation IV.16

and hence:

$$\nu_{cov}^2 = (\kappa d)^2 + (\gamma_{cov} d)^2$$

Equation IV.17

$$\nu_{sub}^2 = (\kappa d)^2 + (\gamma_{sub} d)^2$$

Equation IV.18

Convention takes the reference normalised frequency to be defined by the smaller of these two normalised frequencies, which usually coincides with the core-substrate interface (the refractive index of the substrate is usually higher than the cover and thereby determines the cut-off condition).

The normalised propagation constant is then defined by;

$$b = \frac{n_e^2 - n_{sub}^2}{n_{cor}^2 - n_{sub}^2}$$

Equation IV.19

The asymmetry is parameterised by:

$$\eta = \frac{n_{sub}^2 - n_{cov}^2}{n_{cor}^2 - n_{sub}^2} = \frac{\nu_{cov}^2 - \nu_{sub}^2}{\nu_{sub}^2} = \frac{(\gamma_{cov} d)^2 - (\gamma_{sub} d)^2}{\nu_{sub}^2}$$

Equation IV.20

and hence:

$$(\gamma_{cov} d)^2 = \eta \nu_{sub}^2 + (\gamma_{sub} d)^2$$

Equation IV.21

A simple root solver may be used to solve Equations IV.7 or Equations IV.9 subject to Equation IV.10, Equation IV.11 & Equation IV.12 for any dependent parameter in terms of the remaining independent parameters. For example, Figure IV.1 is a plot of the normalised propagation constant versus the normalised frequency for an air / silicon / silica waveguide.

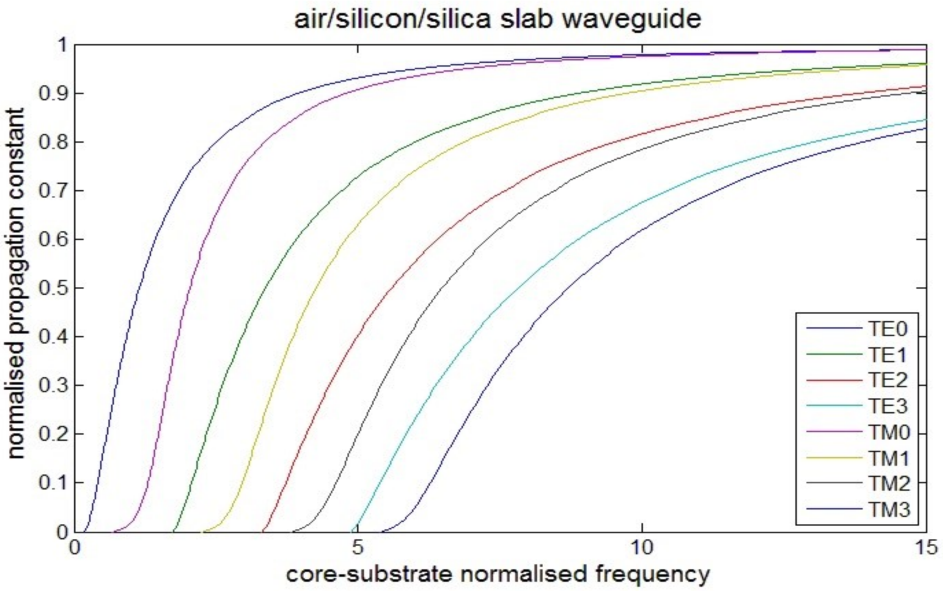

Fig. IV.1. The normalised propagation constant versus normalised frequency for the first 4 TE & TM modes of an air/silicon/silica slab waveguide.

Appendix V:
Python code

CrystalWave has a command interface that accepts commands generated by a Python script. This appendix provides a listing of the Python script used to automate the definition of the graded photonic crystal structure of a metamaterial Lüneburg lens. The code first builds a palette of atoms of different diameters and hence fill-factors that are associated to a specified effective index. It does this using the coefficients of a polynomial that inverts the calibration data (effective index versus fill-factor). An area that contains the lens is then scanned; each lattice point visited is tested to determine if it falls inside the lens; if it does the desired effective index is calculated using the Lüneburg formula from the position of the site and the pallet atom with the nearest associated effective index is substituted for the place-holder atom at the site. At the end, all placeholder atoms that remain are replaced by a palette atom associated to the effective index of the ambient region outside the lens.

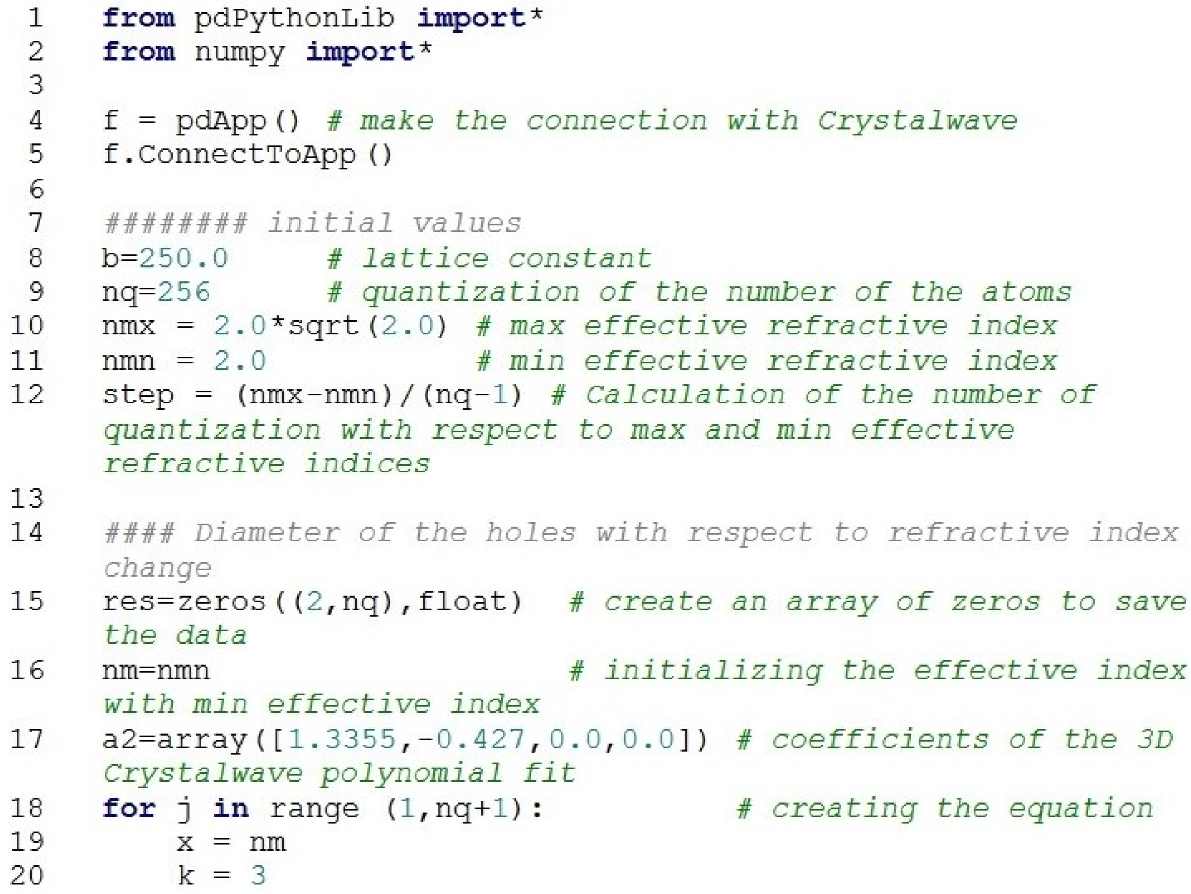

```
from pdPythonLib import*
from numpy import*

f = pdApp() # make the connection with Crystalwave
f.ConnectToApp()

######## initial values
b=250.0      # lattice constant
nq=256       # quantization of the number of the atoms
nmx = 2.0*sqrt(2.0) # max effective refractive index
nmn = 2.0           # min effective refractive index
step = (nmx-nmn)/(nq-1) # Calculation of the number of quantization with respect to max and min effective refractive indices

#### Diameter of the holes with respect to refractive index change
res=zeros((2,nq),float)  # create an array of zeros to save the data
nm=nmn                   # initializing the effective index with min effective index
a2=array([1.3355,-0.427,0.0,0.0]) # coefficients of the 3D Crystalwave polynomial fit
for j in range (1,nq+1):         # creating the equation
    x = nm
    k = 3
```

```
    y = a2[k]
    for i in range (1,k+1):
        y=y*x+a2[k-i]

    phil=(1/2.0)*(y+linalg.norm(y))    # non-negativity constraint for fill-factor calculation
    d = b*sqrt((2*sqrt(3)/pi)*phil)    # calculation of diameter of the atoms with respect to fill-factor
    res[0,j-1]=nm                      # saving the effective index in an array, j-1 because array starts from 0
    res[1,j-1]=d                       # saving the diameter of atoms in an array

######## creat the atom layer in Crystalwave, name the atom and adjust their sizes
    d=d/1000.0  # diameter of atoms in micrometers
    f.Exec("app.subnodes[1].subnodes[1].pcdevice.addellippaletteatom(3)" )
    f.Exec("app.subnodes[1].subnodes[1].pcdevice.paletteatoms2d[{j+1}].startchange()")
    f.Exec("app.subnodes[1].subnodes[1].pcdevice.paletteatoms2d[{j+1}].name={j}")
    f.Exec("app.subnodes[1].subnodes[1].pcdevice.paletteatoms2d[{j+1}].shape.width={d}")
    f.Exec("app.subnodes[1].subnodes[1].pcdevice.paletteatoms2d[{j+1}].shape.height={d}")
    f.Exec("app.subnodes[1].subnodes[1].pcdevice.paletteatoms2d[{j+1}].finishchange()")
    nm=nm+step
######### Finding the points/atoms on the coordinate
rl=7.5       # radius of the lens in micrometer
lcz=b/1000.0 # Lattice constant z direction in micormeter
lcx=b/1000.0 # Lattice constant x direction in micrometer
n0=2.0       # ambient refractive index, the area arround the lens and on the rim

bz=lcz*array([1.0,0.0])        # vector b in z direction
bx=lcx*array([0.5,0.866])      # vector b in x direction
bz_p=lcz*array([0.0,1.0])      # perpendicular vector, complementary
bx_p=lcx*array([-0.866,0.5])  # perpendicular vector
c0=array([7.5,0.0])            # centre coordinate of the lens(z,x)

```

```
c0_x=int(round(dot(c0,bz_p)/dot(bx,bz_p)))  # calculating the vector that define dthe lattice
c0_z=int(round(dot(c0,bx_p)/dot(bz,bx_p)))
p0=c0_z*bz+c0_x*bx

pp=array([0.0,0.0])          # initial value for vector to find the point
q=int(1.1547*(rl/lcx))+1

for pz_s in range (-q,q,1):  # scanning the area, checking the position of the atom
    for px_s in range (-q,q,1):
        pz=pz_s+c0_z
        px=px_s+c0_x
        pp=pz*bz+px*bx
        rp=linalg.norm(pp-c0)
        if rp<=rl:   # if the atom is inside the lens
            nl=n0*sqrt(2.0-(rp*rp)/(rl*rl))   # calculates the distance from the centre of the lens
            an = int(round((nl-nmn)/step))+1  # find the atom number to substiute with the previous atom
            f.Exec("app.subnodes[1].subnodes[1].pcdevice.objects[1].lattice2d.clearlatticepoint({pz},{px})" )  # deleting the old atom
            f.Exec("app.subnodes[1].subnodes[1].pcdevice.objects[1].lattice2d.addlatticeatom({an+1},{pz},{px})" )  # susbtituting the new atom

nl=n0   # effective refractive index of the area outside of the lens
an = int(round((nl-nmn)/step))+1   # defningthe natom number outside of the lens (exterior atom)
d=res[1,an-1]                      # finding the diameter of the exterior atom
d=d/1000.0                         # diameter of exterior atom in micrometer
f.Exec("app.subnodes[1].subnodes[1].pcdevice.paletteatoms2d[1].startchange()")  # substitution of the new exterior atom with the old atoms
f.Exec("app.subnodes[1].subnodes[1].pcdevice.paletteatoms2d[1].name=exterior")
f.Exec("app.subnodes[1].subnodes[1].pcdevice.paletteatoms2d[1].shape.width={d}")
```

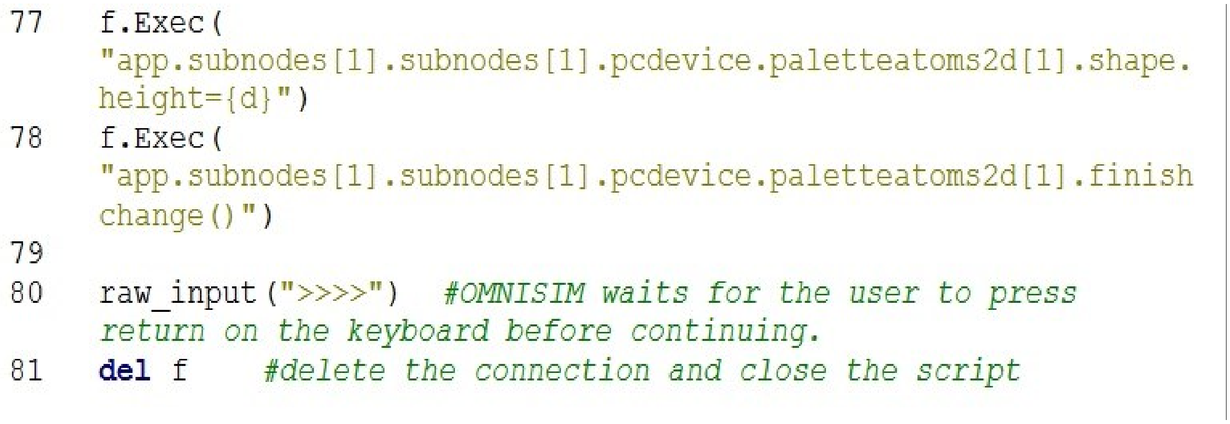

```
f.Exec("app.subnodes[1].subnodes[1].pcdevice.paletteatoms2d[1].shape.height={d}")
f.Exec("app.subnodes[1].subnodes[1].pcdevice.paletteatoms2d[1].finishchange()")

raw_input(">>>>")  #OMNISIM waits for the user to press return on the keyboard before continuing.
del f    #delete the connection and close the script
```

References:

[1] *'An Inefficient Truth'* Global action plan, 2007. http://www.globalactionplan.org.uk/green-it. (*Accessed Aug 2012*).

[2] A. Gladisch, C. Lange, and R. Leppla, '*Power efficiency of optical vs electronic access networks'*, ECOC 2008, 21-25 September 2008, Brussels, Belgium.

[3] T. Asami, S. Namiki, '*Energy Consumption Targets for Network Systems',* ECOC 2008, 21-25 September 2008, Brussels, Belgium.

[4] R. F. Kalman, L. G. Kazovsky, J. W. Goodman, *'Space division switches based on semiconductor optical amplifiers'*, IEEE Photon. Technol. Lett., **4**(9), 1992, pp. 1048-1051.

[5] J. Kim, C. J. Nuzman, B. Kumar, D. F. Lieuwen, J. S. Kraus, A. Weiss, C. P. Lichtenwalner, A. R. Papazian, R. E. Frahm, N. R. Basavanhally, D. A. Ramsey, V. A. Aksyuk, F. Pardo, M. E. Simon, V. Lifton,, H. B. Chan, M. Haueis, A. Gasparyan, H. R. Shea, S. Arney, C. A. Bolle, P. R. Kolodner, R. Ryf, D. T. Neilson,J. V. Gates, *'1100×1100 Port MEMS-Based Optical Crossconnect With 4-dB Maximum Loss'*, IEEE Photon. Technol. Lett., **15**(11), 2003, pp. 1537-1539 .

[6] E. L. Wooten, K. M. Kissa, A. Yi-Yan, E. J. Murphy, D. A. Lafaw, P. F. Hallemeier, D. Maack, D. V. Attanasio, D. J. Fritz, G. J. McBrien, D. E. Bossi*, 'A Review of Lithium Niobate Modulators for Fiber-Optic Communications Systems',* IEEE J. Sel. Topic. Quant, Electron., **6**(1), 2000, pp. 69-81.

[7] J.-M. Brosi, C. Koos, L. C. Andreani, M. Waldow, J. Leuthold, W. Freude, *'High-speed low-voltage electro-optic modulator with a polymer-infiltrated silicon photonic crystal waveguide',* Opt. Exp., **16**(6), 2008, pp. 4177-4191.

[8] J. Ding, H. Chen, L. Yang, L. Zhang, R. Ji, Y. Tian, W. Zhu, Y. Lu, P. Zhou, R. Min, M. Yu, *'Ultra-low-power carrier-depletion Mach-Zehnder silicon optical modulator'*, Opt. Exp., **20**(7), 2012, pp. 7081-7087.

[9] B. Qi, P. Yu, Y. Li, Y. Hao, Q. Zhou, X. Jiang, J. Yang, *'Ultracompact electrooptic silicon modulator with horizontal photonic crystal slotted slab'*, IEEE Photon. Techn. Lett., **22**(10), 2010, pp. 724 726.

[10] L. Alloatti, D. Korn, R. Palmer, D. Hillerkuss, J. Li, A. Barklund, R. Dinu, J. Wieland, M. Fournier, J. Fedeli, H. Yu, W. Bogaerts, P. Dumon, R. Baets, C. Koos, W. Freude, J. Leuthold, *'42.7 Gbit/s electro-optic modulator in silicon technology'*, Opt. Exp., **19**(12), 2011, pp. 11841-11851.

[11] X. Sun, L. Zhou, X. Li, Z. Hong, J. Chen, *'Design and analysis of a phase modulator based on a metal–polymer–silicon hybrid plasmonic waveguide'*, Appl. Opt., **50**(20) , 2011, pp. 3428-3434.

[12] M. Xin, C. E. Png, S. T. Lim, V. Dixit, A. J. Danner, *'A high speed electro-optic phase shifter based on a polymer-infiltrated P-S-N diode capacitor'*, Opt. Exp., **19**(15), 2011, pp. 14354 14369.

[13] J. Ding, H. Chen, L. Yang, L. Zhang, R. Ji, Y.Tian, W. Zhu, Y. Lu, P. Zhou, R. Min, *'Low-voltage, high-extinction-ratio, Mach-Zehnder silicon optical modulator for CMOS compatible integration'*, Opt. Exp., **20**(3), 2012, pp. 3209-3218.

[14] T. Baehr-Jones, R. Ding, Y. Liu, A. Ayazi, T. Pinguet, N. C. Harris, M. Streshinsky, P. Lee, Y. Zhang, A. E.-J. Lim, T.-Y. Liow, S. H.-G. Teo, G.-Q. Lo, M. Hochberg, *'Ultralow drive voltage silicon traveling-wave modulator'*, Opt. Exp., **20**(11), 2012, pp.12014-12020.

[15] H. Yu, M. Pantouvaki, J. Van Campenhout, D. Korn, K. Komorowska, P. Dumon, Y. Li, P. Verheyen, P. Absil, L. Alloatti, D. Hillerkuss, J. Leuthold, R. Baets, W. Bogaerts, *'Performance tradeoff between lateral and interdigitated doping patterns for high speed carrier-depletion based silicon modulators'*, Opt. Exp., **20**(12), 2012, pp. 12927-12938.

[16] H. Xu, X. Xiao, X. Li, Y. Hu, Z. Li, T. Chu, Y. Yu, J. Yu, '*High speed silicon Mach-Zehnder modulator based on interleaved PN junctions'*, Opt. Exp., **20**(14), 2012, pp. 15093 15099

[17] R. Shankar, *'Scalable Optical Switches: Architectures and Physical Layer Characterization'*, PhD thesis, University of Ottawa, Canada, (2008).

[18] D. Parker, C. Zimmermann, *'Phased Arrays—Part I: Theory and Architectures'* ,IEEE Trans. Microwave Theory & Techniques, **50**(3), 2002, pp. 678-687.

[19] W. A. Crossland, I. G. Manolis, M. M. Redmond, K. L. Tan, T. D.Wilkinson, M. J. Holmes, T. R. Parker, H. H. Chu, J. Croucher, V. A. Handerek, S. T. Warr, B. Robertson, I. G. Bonas, R. Franklin, C. Stace, H. J. White, R. A. Woolley, G. Henshall, *'Holographic optical switching: the Roses demonstrator'*,J. Lightwave Technology, **18**(12), 2000, pp. 1845-1854.

[20] I. S. Joe, *'Scalable optical switches with large port count based on a waveguide grating router and passive couplers'*, IEEE Photon. Techn. Lett., **20**(7), 2008, pp. 508-510.

[21] P. J. Winzer, R.-J. Essiambre, '*Advanced Modulation Formats*', Proc. IEEE, **94**(5), 2006, pp.952-985.

[22] W. Mathlouthi, H. Rong, M. Paniccia,*'Characterization of efficient wavelength conversion by four-wave mixing in sub-micron silicon waveguides'*, Opt. Express, **16**(21), 2008, pp. 16735-16745.

[23] K. Van Acoleyen , H. Rogier H, R. Baets, *'Two-dimensional optical phased array antenna on silicon-on-insulator'*, Opt Express, **18**(13), 2010, pp. 13655–13660.

[24] J. Sun, E. Timurdogan, A. Yaacobi, E. S. Hosseini, M. R.Watts, *'Large-scale nanophotonic phased array'*, Nature, **493**, 2013, pp. 195-199.

[25] H. Nikkhah, K. Van Acoleyen, R. Baets, *'Beam steering for wireless optical links based on an optical phased array in silicon'*, Annals of Telecommunications, Springer, **68**(1-2) , 2013, pp 57-62.

[26] M. Johansson, S. Hård, B. Robertson, I. Manolis, T. Wilkinson, W. Crossland, *'Adaptive Beam Steering Implemented in a Ferroelectric Liquid-Crystal Spatial-Light-Modulator Free-Space, Fiber-Optic Switch'*, Applied Optics, **41**(23), 2002, pp. 4904-4911.

[27] H. F. Talbot, *'Facts relating to optical science'*, Phil. Mag. IV, 1836, pp. 401-407.

[28] R. M. Jenkins, J. M. Heaton, D. R. Wight, J. T. Parker, J. C. H. Birbeck G. W. Smith, K. P. Hilton, *'Novel 1×N and N×N integrated optical switches using self-imaging multimode GaAs/AlGaAs waveguides'*, Appl. Phys. Lett. , **64**, 1994, pp. 684-686.

[29] S. Tomofuji, S. Matsuo, T. Kakitsuka, Ken. Kitayama, *'Dynamic switching characteristics of InGaAsP/InP multimode interference optical waveguide switch'*, Optics Express, **17**(26), 2009, pp. 23380-23388

[30] W. Wang, Y. Zhao, H. Zhou, Y. Hao, J. Yang, M. Wang, X. Jiang, *'CMOS-compatible 1×3 silicon electrooptic switch with low crosstalk'*, IEEE Photonics Technology Letters, **23**(11), 2011, pp. 751-753.

[31] Z. Jin, C. J. Kaalund, G. Peng, *'Novel approach to design high-performance large-port-count switches in low-index-contrast materials based on cascaded multimode interference couplers'*, IEEE J. Quant. Electron., **41**(12), 2005, pp. 1548-1551.

[32] T. J. Hall, *'Optical Transpose System'*, US Patent 6. 898.013 B2, (May 24 2005)

[33] T. J. Hall, *'Optical Crossbar Switch'*, US Patent 7. 127.136 B2, (Oct 24. 2006)

[34] H. Chen, A. Poon, *'Low-loss multimode-interference-based crossings for silicon wire waveguides'*, IEEE Photon. Technol. Lett. , **18**(21), 2006, pp. 2260-2262.

[35] T. Fukazawa, T. Hirano, F. Ohno, T. Baba, *'Low loss intersection of Si photonic wire waveguides'*, Jpn. J. Appl. Phys., **43**(2), 2004, pp. 646-647.

[36] W. Bogaerts, P. Dumon, D. Van Thourhout, R. Baets, *'Low-loss, low-cross-talk crossings for silicon-on-insulator nanophotonic waveguides'*, Optics Letters, **32**(19), 2007, pp. 2801-2803.

[37] P. J. Bock, P. Cheben, J. H. Schmid, J. Lapointe, A. Delâge, D.-X. Xu, S. Janz, A. Densmore, T. J. Hall, *'Subwavelength grating crossings for silicon wire waveguides'*, Optics Express, **18**(15), 2010, pp. 16146-16155.

[38] P. J. Bock, *'Addressing the challenges of silicon waveguides with subwavelength nanostructures'*, PhD Thesis, University of Ottawa, 2011.

[39] D. F.G. Gallagher, T. P. Felici, *'Eigenmode Expansion Methods for Simulation of Optical Propagation in Photonics - Pros and Cons'*, Photonics West, San Jose, 2003, Proc. SPIE, **4987**, 2003, art. 4987-10, pp. 69-82

[40] I. Tsukerman, *'Computational Methods for Nanoscale Applications : Particles, Plasmons and Waves'*, (Springer, 2008).

[41] K. Patorski, *'The self-imaging phenomenon and its applications'*, Progress in Optics, **27**, 1989, pp. 1–108.

[42] J. J. O'Connor, E. F. Robertson, *'William Henry Fox Talbot'*, MacTutor History of Mathematics, 2005. http://www-history.mcs.st andrews.ac.uk/Biographies/Talbot.html (last accessed 6 May 2012)

[43] Y. Lu, J. Zheng, P. Li, *'The influence of the polarization effect in Talbot self-imaging of high-density gratings'*, Optik, **122**(9), 2011, pp. 799–803.

[44] P. Zhou, J. H. Burge, *'Analysis of wavefront propagation using the Talbot effect'*, Applied Optics, **49**(28), 2010, pp. 5351–5359.

[45] Lord Rayleigh, *'On copying diffraction-gratings, and on some phenomenon connected therewith'*, Phil. Mag., **11**, 1881, pp. 196–205

[46] M. Berry, I. Marzoli, W. Schleich, *'Quantum Carpets, Carpets of Light'*, Physics World, **14**(6), 2001, pp. 39–44.

[47] M. V. Berry, S. Klein, *'Integer, fractional and fractal Talbot effects'*, Journal of Modern Optics, **43**(10), 1996, pp. 2139–2164.

[48] L. Auslander, R. Tolimieri, *'Is computing with the finite Fourier transform pure or applied mathematics?'*, Bulletin of the American Mathematical Society, **1**(6), 1979, pp. 847-897.

[49] R. Ulrich, G. Ankele, *'Self-imaging in homogeneous planar optical waveguides'*, Appl. Phys. Lett. **27**(6), 1975, pp. 337-339.

[50] O. Bryngdahl, *'Image formation using self-imaging techniques'*, J. Opt. Soc. Am. **63**(9), 1973, pp. 416-419

[51] M. Bachmann, P. A. Besse, H. Melchior, *'General self-imaging properties in N × N multimode interference couplers including phase relations'*, Applied Optics, **33**(18), 1994,.pp. 3905-3911

[52] L. B. Soldano, E. C. M. Pennings, *'Optical multi-mode interference devices based on self-imaging: principles and applications*', Journal of Lightwave Technology, **13**(4), 1995, pp. 615-627

[53] J. M. Heaton, R. M. Jenkins, *'General matrix theory of self-imaging in multimode interference (MMI) couplers'*, IEEE Photon. Technol. Lett., **11**(2), 1999, pp. 212-214.

[54] L. B. Soldano, *'Multimode Interference Couplers: Design and Applications'*, ISBN-10: 9040710449, ISBN-13: 978-9040710445, Delft Univ Pr, (December 1994), 98 pages.

[55] S. Chandrasekhar, X. Liu, *'Enabling components for future high-speed coherent communication systems'*, in Optical Fibre Communication Conference (OFC), OSA Technical Digest (CD) (Optical Society of America, 2011), paper OMU5, 2011.

[56] K. Van Acoleyen, J. Roels, P. Mechet, T. Claes, D. Van Thourhout, R. Baets, *'Ultracompact phase modulator based on a cascade of NEMS-operated slot waveguides fabricated in silicon-on-insulator'*, IEEE Photonics J., **4**(3), 2012, pp. 779-778

[57] R. Halir, I. M. Fernández, A. O. Moñux, J. G. W. Pérez, D. X. Xu, P. Cheben, S. Janz, *'A design procedure for high-Performance, rib-waveguide-based multimode interference couplers in silicon-on-insulator'*, J. Lightwave Techn., **26**(16), 2008, pp. 2928-2936.

[58] A. Maese-Novo, R. Halir, S. Romero-García, D. Pérez-Galacho, L. Zavargo-Peche, A. Ortega-Moñux, I. Molina-Fernández, J. G.Wangüemert-Pérez, P. Cheben, *'Wavelength independent multimode interference coupler'*, Opt. Exp. **21**(6), 2013, pp. 7033 7040

[59] G. C. Marsden, P. J. Marchand, P. Harvey, S. C. Esener, *'Optical transpose interconnection system architectures'*, Opt. Lett., **18**(13), 1993, pp. 1083-1085.

[60] M. P. Christensen, P. Milojkovic, M. W. Haney, *'Analysis of a hybrid micro/macro-optical method for distortion removal in free-space optical interconnections'*, J. Opt. Soc. Am. A, **19**(12), 2002, pp. 2473-2478.

[61] M. P. Christensen, P. Milojkovic, M. J. McFadden, M. W. Haney, *'Multiscale Optical Design for Global Chip-to-Chip Optical Interconnections and Misalignment Tolerant Packaging'*, IEEE J. Select. Topics Quant. Electron, **9**(2), 2003, pp. 548-556.

[62] W. Pijitrojana, T. J. Hall, *'Optical Transpose Interconnection System Architectures'*, Thammasat Int. J. Sc. Tech, **8**(4), 2003, pp. 46-54.

[63] A. Walther, *'Ray & Wave Theory of Lenses'* (Cambridge University Press, 2006).

[64] K. von Bieren, *'Lens Design for Optical Fourier Transform Systems'*, Appl. Opt. **10** (12), 1971, pp. 2739-2742.

[65] T. Tyc, L. Herzánová, M. Šarbort, K. Bering, *'Absolute instruments and perfect imaging in geometrical optics'*, New Journal of Physics 13, 2011, art. 115004, pp. 1-23.

[66] R. K. Lüneburg, *'Mathematical Theory of Optics'*, Providence Rhode Island: Brown University, 1944, pp. 189–213.

[67] G. Zouganelis, D. Budimir, *'Effective dielectric constant and design of sliced Lüneberg lens'*, Microwave & Optical Technology Letters, **49**(10), 2007, pp. 2332-2337.

[68] K. Yee, *'Numerical solution of initial boundary value problems involving Maxwell's equations in isotropic media'*. IEEE Transactions on Antennas and Propagation, **14** (3), 1966, pp. 302–307

[69] Z.-C. Le, S-G. Huang, M. L. Fu, W. Dong, J. Zhang, M. Zhang, *'Study on self-imaging properties for line-tapered multimode interference couplers'*, Optics Comm., **284**, 2011, pp. 5303-5310.

[70] D. B. Anderson, R. L. Davis, J. T. Boyd, R. R. August,*'Comparison of Optical-Waveguide Lens Technologies'*, IEEE J. Quant. Electron., **QE-13**(4), 1977, pp. 275-282.

[71] Tuck C. Choy, *'Effective Medium Theory: Principles and Applications'*, (Oxford University Press, 1999).

[72] http://www.epixfab.eu/ *(Last accessed July 2013)*

[73] L. O'Faolain, X. Yuan, D. McIntyre, S. Thoms, H. Chong, R.M. De La Rue, T.F. Krauss, *'Low-loss propagation in photonic crystal waveguides'*, Electron. Lett., **42**(25), 2006, pp. 1454-1455.

[74] J. H. Schmid, P. Cheben, P. J. Bock, R. Halir, J. Lapointe, S. Janz, A. Delage, A. Densmore, J. -M. Fedeli, T. J. Hall, B. Lamontagne, R. Ma, I. Molina-Fernandez, D. -X. Xu, *'Refractive Index Engineering With Subwavelength Gratings in Silicon Microphotonic Waveguides'*, IEEE Photonics Journal, **3**(3), 2011, pp. 597-607.

[75] H. Gao,,B. Zhang, S. G. Johnson, G. Barbastathis, *'Design of thin–film photonic metamaterial Lüneburg lens using analytical approach'*, Optics Express, **20**(2), 2012, pp.1617-1628.

[76] L. D. Landau, E. M. Lifshitz, *'Electrodynamics of continuous media'*, (Pergamon, Oxford, 1984)

[77] D. R. Smith, J. B. Pendry, *'Homogenization of metamaterials by field averaging'*, J. Opt. Soc. Am. B, **23**(3), 2006, pp. 391-403

[78] J. B. Pendry, D. R. Smith, *'Reversing light with negative refraction'*, Phys. Today, **57**(6), 2004, pp. 37-43.

[79] I. Tsukerman, *'Effective parameters of metamaterials: a rigorous homogenization theory via Whitney interpolation'*, J. Opt. Soc. Am. B **28**(3), 2011, pp. 577-586.

[80] I. Tsukerman, *'Nonlocal homogenization of metamaterials by dual interpolation of fields'*, J. Opt. Soc. Am. B **28**(12), 2011, pp. 2956-2965

[81] V. V Gozhenko, A. K. Amert, K. W Whites, *'Homogenization of periodic metamaterials by field averaging over unit cell boundaries: use and limitations'*, New Journal of Physics **15**, 2013, 043030, pp. 1-27.

[82] X. Y.Z. Xiong. L. J. Jiang, V. A. Markel, I. Tsukerman. *'Surface waves in three-dimensional electromagnetic composites and their effect on homogenization'*, Optics Express, **21**(9), 2013, pp. 10412-10421.

[83] J S Pérez-Huerta, Guillermo P Ortiz, Bernardo S Mendoza, W Luis Mochán, *'Macroscopic optical response and photonic bands'*, New Journal of Physics, **15,** 2013, 043037, pp. 1-18.

[84] A. Torre, *'Linear Ray and Wave Optics in Phase Space'*, (Elsevier, 2005).

[85] Y. Jiao, S. Fan, D. A. B. Miller, *'Designing for beam propagation in periodic and non-periodic photonic nanostructures: Extended Hamiltonian method'*, Phys. Rev. E, **70**, 2004, art. 036612, pp. 1-9.

[86] P. S. J. Russel, T. A. Birks, *'Hamiltonian optics of non-uniform photonic crystals'*, J. Lightwave Technol., **17**(11), 1999, pp. 1982–1988.